Novel Nonlinear Microscopy Techniques Based on Femtosecond Laser Pulse Shaping and Their Applications

by

Baolei Li

Department of Physics
Duke University

Date:_____

Approved:

_____
Warren S. Warren, Chair

_____
Daniel J. Gauthier

_____
Martin C. Fischer

_____
Joshua E. S. Socolar

_____
Kate Scholberg

Dissertation submitted in partial fulfillment of
the requirements for the degree of Doctor of Philosophy in the Department of Physics in the Graduate School
of Duke University

2012

ABSTRACT

Novel Nonlinear Microscopy Techniques Based on Femtosecond Laser Pulse Shaping

and Their Applications

by

Baolei Li

Department of Physics
Duke University

Date:_____

Approved:

_____
Warren S. Warren, Chair

_____
Daniel J. Gauthier

_____
Martin C. Fischer

_____
Joshua E. S. Socolar

_____
Kate Scholberg

An abstract of a dissertation submitted in partial
fulfillment of the requirements for the degree
of Doctor of Philosophy in the Department of
Physics in the Graduate School
of Duke University

2012

Abstract

Nonlinear optical microscopy serves as a great tool for biomedical imaging due to its high resolution, deep penetration, inherent three dimensional optical sectioning capabilities and superior performance in scattering media. Conventional nonlinear optical microscopy techniques, e.g. two photon fluorescence and second harmonic generation, are based on detecting a small light signal emitted at a new wavelength that is well separated from the excitation light. However, there are also many other nonlinear processes, such as two-photon absorption and self-phase modulation, that do not generate light at new wavelengths and that have not been extensively explored for imaging. This dissertation extends the accessible mechanisms for contrast to the later nonlinear optical processes by combining femtosecond laser pulse shaping and homodyne detection. We developed a rapid pulse shaper with a relatively simple and compact instrument design that modifies the spectrum of individual laser pulses from an 80 MHz mode-locked laser. The pulse shaper enables simultaneous two-photon absorption and self-phase modulation imaging of various nanoparticles in-vitro with high sensitivity. We also applied this imaging technique to study the nonlinear optical response in graphene. Because our technology detects the nonlinear signature encoded within the laser pulse itself, we achieve intrinsic contrast of biological and non-biological samples in highly scattering media. These capabilities have significant implications in biomedical imaging and nanophotonics.

Contents

List of Tables

List of Figures

Acknowledgements

It has been a great experience studying at Duke University as a graduate student. On my journey towards seeking a doctorate degree, I have received invaluable guidance and support from my advisors, colleagues, family and friends. I would like acknowledge everyone who has contributed to this dissertation.

First, I would like to express my gratitude to my dissertation committee. I am grateful to my advisor Dr. Warren S. Warren for all the guidance and encouragement he has provided me during my graduate studies. I appreciate his patience and his belief in me. His guidance and vision in all aspects of my research projects directly led to my academic accomplishment as a graduate student and played an essential role in my professional growth. I would like to thank Dr. Martin C. Fischer for his hand-on training in every aspect of research. I appreciate all the critical experimental skills Dr. Fischer has taught me and all his help on any problem I have encountered in my research. I would like to thank Dr. Daniel J. Gauthier for serving as the chair of my committee for the first two years. Dr. Gauthier's guidance and support played a critical role in my academic growth. I would also like to thank Dr. Joshua Socolar and Dr. Kate Scholberg for reading and commenting on my dissertation.

During my research I had many useful discussions with present and past graduate students and postdocs in Warren^2 lab. I would like to thank Dr. Jesse Wilson, Dr. Prathyush Samineni, Kevin E. Claytor, Dr. Francisco Robles, Dr. Yuming Chen, Dr. Dan Fu

and Dr. Thomas Matthews for their help in experiments, data analysis, and discussing experimental results. I would like to thank Dr. Simone Degan for his support and suggestions in various tissue experiments. I would like to thank Christina Sun Gainey, Dr. Thomas Theis, Ryan Davis, Mary Jane Simpson and other group members for proof-reading and commenting on my dissertation. I am also grateful for the administrative support in the physics and the chemistry departments during my graduate study.

I would like to acknowledge our collaborators. My dissertation project would not be successful without their support. I would like to thank Dr. Hsiangkuo Yuan and Prof. Tuan Vo-Dinh for providing all the breast cancer cell samples incubated with gold nanoparticles or graphene flakes. I am grateful to Congwen Yi and Prof. April S. Brown for their help in preparing various monolayer and few-layer graphene samples. I would like to thank Yingwen Cheng for developing reduced graphene oxide flakes for the in vitro graphene imaging experiment and preparing various graphene samples. I appreciate Prof. Jie Liu's suggestions and guidance with the graphene imaging project. I am grateful to Dr. Zheshen Zhang from MIT for his support on numerical calculation of the third-order nonlinear susceptibility of graphene.

Finally, I would like to thank my parents and sisters for their support, patience and belief in me throughout the course of my doctoral study.

1. Novel nonlinear optical microscopy

For over than 300 years, optical microscopy methods have enabled biologists to observe an enormous variety of small creatures, from microbes to subcellular organelles, with ever-increasing spatial resolution and ever-expanding contrasts. Optical microscopy is also an essential tool for characterizing microstructures and probing their fundamental physical properties. Along with the development of modern laser technology and nonlinear optics, many nonlinear optical processes have been adapted for imaging, providing not only structural, but also the chemical information of samples. This chapter reviews advances in nonlinear microscopy with a focus on the novel nonlinear contrasts recently enabled by pulse shaping techniques. We then introduce the major contributions of the work in this dissertation to this emerging field. At the end of this chapter, the organization of the rest of the dissertation is described.

1.1. Introduction to conventional nonlinear optical microscopy

Optical microscopy methods can be categorized into two groups: linear and nonlinear microscopy, which distinguish signals according to their dependence on the intensity of the incident light. Because it takes two or more photons to produce nonlinear signals, nonlinear optical microscopy is also known as multi-photon microscopy. Pulsed lasers are usually employed to achieve the high peak intensity with low average power required for nonlinear optical microscopy [1, 2]. A commonly adopted laser system for biomedical imaging consists of a mode-locked laser operating

at a few tens of MHz (i.e. one pulse every 10 nanoseconds). The pulse duration usually ranges from a few tens of femtoseconds (10^{-15} s) to a few picoseconds (10^{-12} s). Pulsed lasers can provide much more energy in a single pulse and significantly increase the peak intensity, leading to observable nonlinear optical effects at moderate average power levels (few mW). Nonlinear optical microscopy with a pulsed laser also dramatically reduces the risk of cell damage that can occur when dealing with linear microscopy (e.g. the bleaching effect in confocal fluorescence microscopy). Moreover, with less energy deposited into the sample, the overall system suffers less adverse effects due to heating.

1.1.1. Advantages of nonlinear optical microscopy

One major advantage of nonlinear microscopy is the ability to inherently provide three dimensional optical sectioning [1, 3]. In the linear regime, contrast is usually due to path integrated absorption [4], reflectance[5-9], fluorescence[10-12], fluorescence lifetime[13-17], and Raman scattering [18-20]. Therefore, signals from different depths accumulate, diminishing the depth information (tight focusing does not help in this case because it is the total flux, not the intensity that matters). As shown in Figure 1.1(a), in linear microscopy, a cone of fluorescent light can be generated. By using a pinhole before the detector (as an aperture), a confocal microscope can reject signals from regions other than the focal plane, and hence is capable of producing depth-resolved images with raster beam scanning or stage scanning [21-23]. Empowered by the

invention of the laser, confocal microscopes are able to provide near diffraction limited information in three dimensions [22, 23]. Linear contrasts such as fluorescence, Raman and reflectance can be implemented in the confocal arrangement to generate high-resolution depth-resolved images [21-25]. However, confocal microscopes have some limitations in highly scattering media. First, out-of-focus photons can still register at the detector due to random scattering [3, 26]. These photons degrade the contrast, severely limiting the imaging depth in heavily scattering media. In addition, because the pinhole highly reduces the efficiency of photon collection, longer acquisition time is usually needed to obtain a sufficient signal-to-noise ratio, limiting the imaging speed.

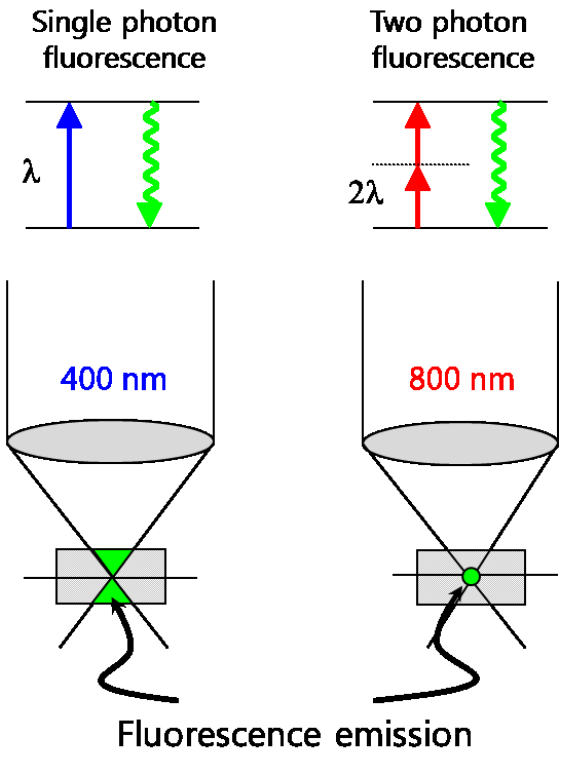

Figure 1.1: Comparison of single-photon fluorescence (left) and two-photon fluorescence (right). Two-photon excitation is localized to the focal volume.

In contrast, nonlinear optical imaging methods produce depth-resolved signals by selective excitation instead of spatial filtering on the detection side [1, 3]. Because of the higher order intensity dependence, the nonlinear signal is created almost exclusively in the focal volume of the input laser beam. As shown in Figure 1.1(b), in the nonlinear case, the signal production is localized to the focal spot. This strong localization enables three-dimensional sectioning without using additional apertures even in a heavily scattering medium, because any signals collected necessarily originate from the focal volume. This property significantly increases the penetration depth of nonlinear optical microscopy into scattering media, such as tissue.

The second advantage of nonlinear imaging methods lies in the fact that they can employ multiple photons in the near IR region (often referred to as the therapeutic window shown in Figure 1.2) to excite the nonlinear signal, which requires one visible or ultraviolet photon in the linear regime [3, 25, 27]. Near-IR (NIR) light experiences less absorption in tissue as compared to other wavelengths. Therefore, using NIR light increases the penetration depth of nonlinear microscopy and assists its application in imaging cells *in vivo* [28, 29]. The reduced absorption also reduces the energy deposited in the sample which decreases the risk of sample damage.

A third advantage is the ability to obtain chemically specific information without fluorescent labeling. As we will demonstrate later, this is made possible by probing various resonant energy levels (electronic or vibrational) in the molecules of interest to greatly enhance the desired output signal. By avoiding the use of fluorescent tags, *in vivo*

or *in vitro* studies of cells may be achieved without disturbance of the natural cellular processes and environment.

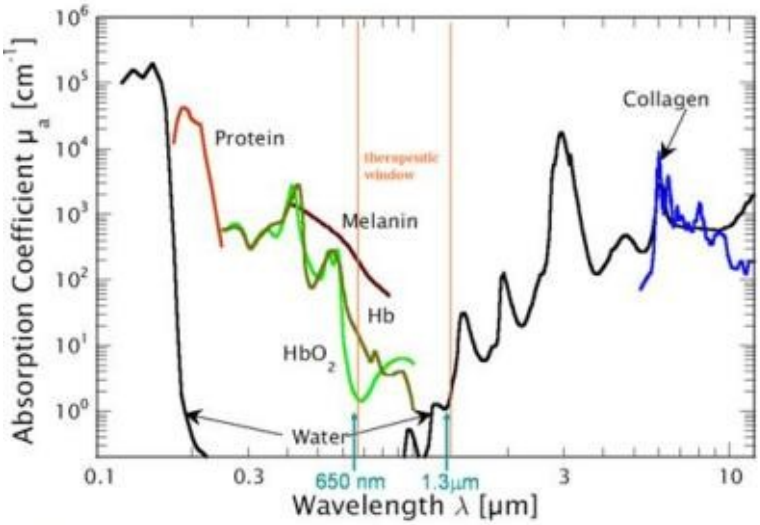

Figure 1.2: Optical absorption spectra of various tissue components in the ultraviolet to infrared wavelength range. The window from 650 nm to 1.3 μm displays the least absorption and is called the "therapeutic window" for optical tissue imaging.

1.1.2. Conventional nonlinear optical microscopy

Many nonlinear optical imaging methods have been developed for tissue imaging, such as two-photon fluorescence (TPF) [1, 3, 25, 30-34], second-harmonic generation (SHG)[8, 35-37], third-harmonic generation (THG)[37-39], and coherent anti-Stokes Raman scattering (CARS) [2, 40]. TPF based imaging is the most commonly utilized and well developed nonlinear imaging technique. As shown in Figure 1.3(a), in TPF, a molecule is excited by absorbing two photons of nearly half the energy that is required to enable the direct electronic transition. However, only a few species of biological molecules fluoresce, and thus, the intrinsic TPF contrast in tissue is significantly

limited. To enhance the contrast, exogenous fluorescent labeling is usually needed, but labeling can perturb the studied system and fluorophores are prone to photobleaching. Additionally in TPF, light generated at shorter wavelengths suffers from strong re-absorption and scattering, and thus has difficulty reaching the detector.

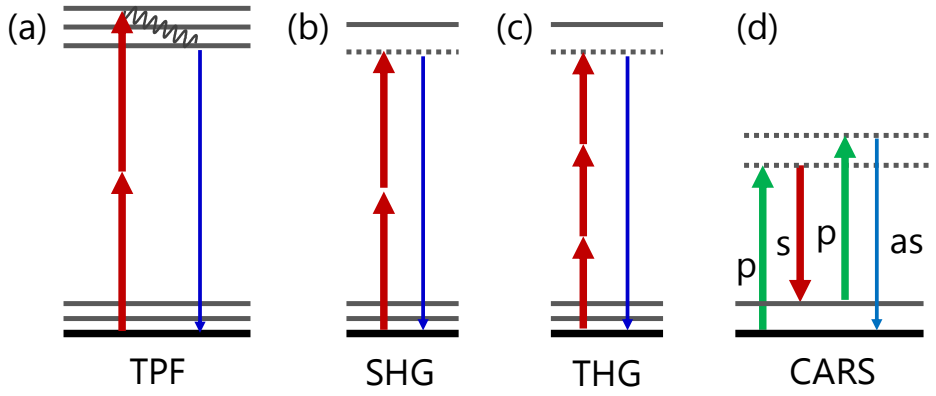

Figure 1.3: Several nonlinear processes that generate light at different wavelengths than what is used for excitation. In CARS (d), *p* stands for pump, *s* for Stokes and *as* for anti-Stokes. These processes are easily adopted for nonlinear optical imaging.

Harmonic generation is an energy conserving process, thus causing minimal energy deposition in the sample and lowering photodamage. It does not need external labeling and does not suffer from photobleaching. However, severe symmetry constraints restrict the range of possible targets for harmonic generation imaging. For example, SHG (Figure 1.3(b)) is limited to anisotropic material, such as collagen, microtubules, and muscle myosin (used to get intrinsic structural contrast). SHG is associated with second order nonlinear susceptibility, $\chi^{(2)}$, which is non-zero only in non-centrosymmetric molecules. THG (Figure 1.3(c)), on the other hand, is associated with the

real part of third-order nonlinear susceptibility $\chi^{(3)}$ and is primarily generated at interfaces.

CARS is another third-order nonlinear optical process associated with $\chi^{(3)}$. As shown in Figure 1.3 (d), it usually takes two degenerate pump photons and one Stokes photon to generate an anti-Stokes photon. The generation of anti-Stokes signal is enhanced when the frequency difference between the pump and the Stokes beams matches a Raman transition (a vibrational level). CARS provides chemically specific and intrinsic molecular contrast. However, the large nonresonant background in CARS presents a major challenge in the utility of CARS microscopy [2, 40]. In Chapter 5 we will discuss CARS further and introduce a new way to eliminate the nonresonant background by using femtosecond laser pulse shaping [41].

1.2. Novel nonlinear contrasts enabled by laser pulse shaping

One common feature of the above mentioned nonlinear optical imaging contrast mechanisms (TPF, SHG, THG, and CARS) is that they are all based on the emission of light at a new wavelength that is well separated from the excitation light. However, there are many other nonlinear optical processes that do not necessarily create new light, for example, self-phase modulation (SPM), two-photon absorption (TPA), sum-frequency absorption (SFA), ground state depletion (GSD), excited state absorption (ESA), stimulated emission (STE) and stimulated Raman scattering (SRS), as shown in Figure 1.4. Harnessing these optical processes for nonlinear imaging presents great challenges for

the nonlinear microscopy community, but it also provides many advantages. Specifically, these processes are usually more common and are thus able to provide intrinsic molecular contrast. For example, TPA is a required process for TPF, but not all molecules that experience TPA are fluorescent, and SPM is ubiquitous in biological and non-biological samples. ESA and SRS can provide rich chemical specific information on molecules with biomedical significance, e.g. melanin, hemoglobin, and amino acids.

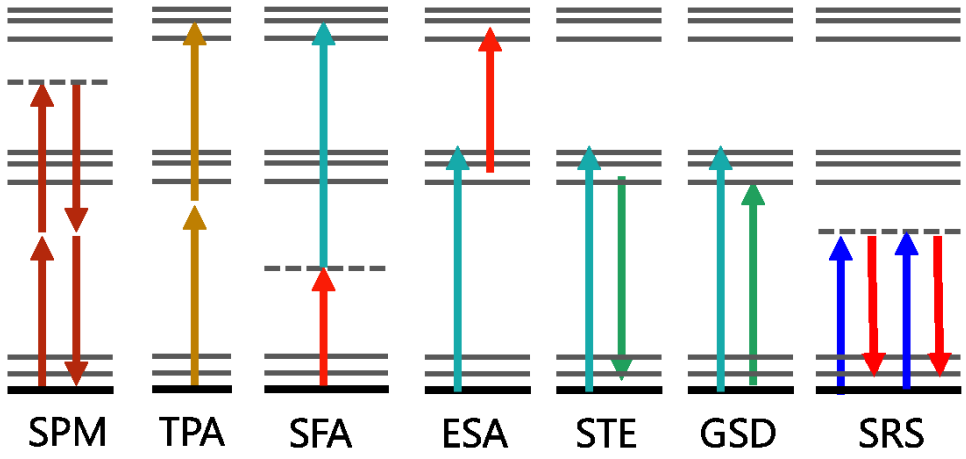

Figure 1.4: Several nonlinear processes that do not generate light at different wavelengths. Pulse shaping or pulse train shaping can make these processes accessible contrasts for nonlinear optical imaging.

1.2.1. Pump-probe microscopy

The Warren group is at the forefront of the development of novel nonlinear optical imaging techniques utilizing these processes to gain access to previously inaccessible endogenous contrasts in biological samples [27, 42-51]. The key behind these innovations is the pulse train shaping or pulse shaping technique described below.

In principle, any nonlinear optical processes involving a two-beam interaction could be adapted for nonlinear optical imaging using a pump-probe type of measurement. The basic idea behind pump-probe imaging is the modulation transformation illustrated in Figure 1.5. The pump beam (a train of mode-locked laser pulses) is modulated at a frequency of a few MHz. This intensity modulation will impose an intensity modulation at the same frequency onto the probe beam through the nonlinear optical interaction. The amplitude of this transferred modulation is usually very small (10^{-6}) but can be measured by sensitive homodyne detection using a lock-in amplifier. With the presence of a pump pulse, the probe pulse may gain or lose energy, resulting in in-phase (positive) or out-of-phase (negative) modulation in the probe beam [27, 45, 52, 53]. For example, GSD and STE induce in-phase signal, while SFA and ESA result in out-of-phase signals.

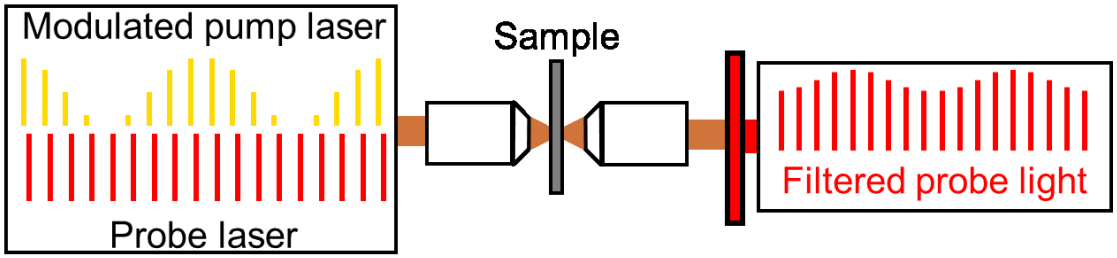

Figure 1.5: Modulation transformation in pump-probe microscopy. Due to the cross-talk between the two laser beams, the intensity modulation in the pump beam is transferred onto the probe beam. The pump beam is rejected by the filter such that the modulation in the probe beam can be measured by a lock-in amplifier with zero background.

The contrast in pump-probe microscopy can be significantly enhanced when the wavelength configuration matches the energy level diagrams of certain molecules.

Further, the time delay between the pump and the probe pulse provides another degree of freedom. The delay trace of the pump-probe signal reflects the temporal evolution of the ground state or the excited state population, thereby measuring the molecular dynamics of the system and providing molecular specific contrast.

Pump-probe imaging has been successfully applied for imaging the oxygenation of hemoglobin[52], skin pigments (distinguishes eumelanin from pheomelanin)[53, 54], and pigments used for paintings[55]. Pump-probe-type STE and SRS microscopy have also demonstrated in various applications in biomedical imaging [56-58].

1.2.2. Spectral reshaping for SPM and TPA measurement

SPM and TPA only involve a single laser beam. Both processes alter the spectrum of the input laser pulse due to cross-talk between different frequency components. However, this change is rather small and can be easily buried in the variation caused by various linear interactions. One way to extract the nonlinear signature of SPM and TPA is through spectral reshaping: the spectrum of the input pulse is shaped in a way such that the spectral modification caused by a nonlinear process may produce a detectable signal that is unique to each specific physical phenomenon. For example, one can measure the nonlinear signal through a hole-refilling mechanism, where a pre-manufactured spectral hole is refilled when the pulse undergoes TPA or SPM, and thus the nonlinear signal can be measured against zero background [42, 49].

Spectral reshaping techniques can be implemented in a homodyne configuration. Instead of completely eliminating the spectral component in the hole, one can leave a local oscillator in the hole (LO, a spectral component with cycling phase) to interfere with the generated nonlinear signal [44, 59]. In this manner, not only can the weak signal be amplified but the phase of the nonlinear signal can also be ascertained, i.e. SPM signal can be discerned from TPA signal. The basic principle of the spectral reshaping technique has been successfully demonstrated with an amplified laser system operating at 20 KHz [44, 59]. However, for fast nonlinear imaging, especially in tissue samples, fast repetition rate (mode-locked) lasers and high data acquisition rate are desired. Although our initial attempt has shown that rapid pulse shaping for individual mode-locked laser pulses is possible[60], the sensitivity of our previous pulse shaping technique is inadequate due to the unwanted instrumental background in detection. The current dissertation explores the best pulse shapes for spectral reshaping techniques with mode-locked lasers and describes a rapid pulse shaper that can create such pulse shapes.

1.3. Imaging nanomaterials with novel microscopy

In this dissertation, we also demonstrate two applications of our SPM and TPA imaging: imaging gold nanostars in breast cancer cells and nonlinear optical characterization and imaging of graphene. In the 1990s, advances in material science and engineering enabled us to manufacture materials and functional structures at the nanometer scale, which is smaller than the size of naturally existing cells and many sub-

cellular organelles [61-63]. These materials have a broad range of applications in industry, biology, and medicine [31, 64-66]. Nanomaterial can have much larger and tunable nonlinear optical coefficients than bulk material, due to quantum confinement effects [67]; therefore our novel nonlinear microscopy technique based on spectral reshaping is a promising tool for characterizing the material itself and studying its biomedical applications [67, 68].

1.4. Outline of the dissertation

The rest of this dissertation is organized as follows: Chapter 2 describes the fundamental principles behind the spectral reshaping technique and explores the effect of various pulse shapes for rapid SPM and TPA imaging via numerical simulations. Chapter 3 focuses on the experimental realization of the spectral reshaping technique. After introducing the general background of laser pulse shaping, we provide a detailed discussion on the configuration of a newly designed rapid pulse shaper based on a wing-cut pulse shape, the optimal pulse shape discussed in Chapter 2. In Chapter 4, we showcase the application of our novel nonlinear optical imaging techniques for graphene characterization and imaging graphene in a biological environment, specifically in breast cancer cells. In Chapter 5, we employ a similar pulse shaping technique to suppress the nonresonant background in CARS spectroscopy.

2. Pulse shape optimization for nonlinear optical imaging by femtosecond pulse reshaping

This chapter explores the effects of various femtosecond spectral reshaping techniques on nonlinear signals. We first introduce the fundamental principle behind the spectral reshaping techniques. We then present a systematic numerical simulation to investigate the mechanism of nonlinear signal generation with different pulse shapes, including the spectral-hole shape and the wing-cut shape. An optimal pulse shape is identified with considerations of all possible challenges in implementation.

2.1. The principle of spectral reshaping

When a broadband laser pulse undergoes a nonlinear optical process, one spectral component may interact with other components, introducing characteristic modifications to the original spectrum, such as spectral broadening or nonlinear absorption. Through these interactions certain nonlinear signatures are imprinted into the spectrum of the output beam. Pre-shaping the spectrum of the laser pulse in a way such that the spectral modifications caused by a nonlinear optical process will lead to a unique and measurable effect is thus the fundamental principle behind spectral reshaping techniques.

In the limit of extremely intense laser pulses, the possible observable nonlinear processes are almost limitless. However, the ultimate objective here is imaging sensitive materials, such as living tissue, and as a result it is critical to limit the applied power. In typical applications described later, we use much less average power than a laser pointer

(5 mW), and roughly 10^{-7} of the photons actually participate in the nonlinear processes. In addition, the materials in general are highly scattering. So we are primarily interested in finding nonlinear optical signatures which are robust, readily detected and separable from scattered light. As discussed in Chapter 1, these constraints have restricted traditional nonlinear imaging to methods which generate light of a different color than the excitation light. What is new here, and is a primary focus of the Warren group, is an extension to processes which do not generate light of a different color, but instead use manipulations of the optical pulses (primarily pulse shaping to permit hole refilling and homodyne detection) to resolve the nonlinear signatures.

To elaborate on this principle, we discuss here the hole-refilling technique developed by the Warren group [42, 44, 46, 59], where a pre-manufactured spectral hole can be refilled by one of three nonlinear processes: two-photon absorption (TPA), saturable absorption (SA) or self-phase modulation (SPM). In the simplest case, TPA is assumed to cause an attenuation of the electric field proportional to the instantaneous intensity (electric field squared). SA causes an attenuation of the electric field proportional to the instantaneous field (linear absorption), plus a correction that is positive and proportional to the instantaneous intensity (electric field squared). SPM is assumed to cause a phase shift proportional to the instantaneous intensity (we will be more quantitative in the next section). Figure 2.1 and 2.2 illustrate these effects.

As shown in Figure 2.1 (top-left), a spectral hole is created at the center of a broadband laser spectrum with an initial Gaussian profile. According to the Fourier

transform theorem, in the time domain, this particular spectrum is equivalent to the combination of a short pulse with higher intensity and a negative long pulse with lower intensity (Figure 2.1, bottom-left). If the intensity at the bottom of the hole in the frequency domain is zero, the total area of the laser pulse in the time domain must be zero by the Fourier transform. Thus the areas covered by these two Gaussian pulses in the time domain are the same but with opposite sign. Because TPA depends on the square of the intensity, the short, intense positive pulse experiences much larger attenuation than the less intense negative long pulse (Figure 2.1, bottom-right). Consequently, the areas of these two pulses are no longer equal. In the frequency domain (Figure 2.1, top-right), this imbalance corresponds to a non-zero component in the center of the spectrum; the spectral hole is refilled.

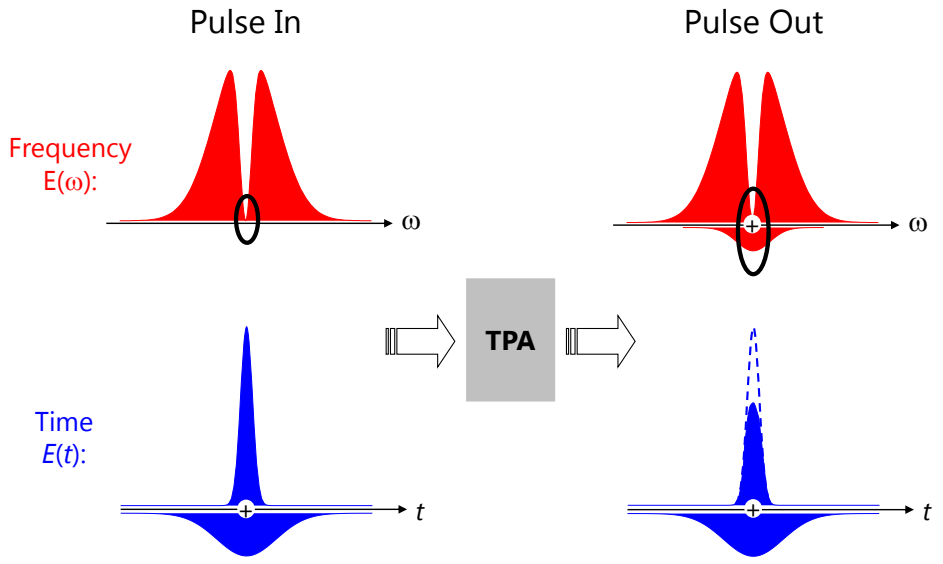

Figure 2.1: Two-photon absorption (TPA) refills the spectral-hole in a femtosecond pulse spectrum with a negative, real component. Saturable absorption (SA) would refill the spectral hole with a positive component (see text).

Since TPA is a loss process, the newly generated component is negative (180^{o} out of phase), with respect to the incoming pulse. Saturable absorption (a fractional attenuation of the laser pulse in the time domain that becomes smaller as the intensity grows) would instead produce a larger attenuation of the negative-going portion, and would reshape the pulse to produce a newly generated component which is positive (in phase with respect to the incoming pulse). Going forward, we will generally refer to images using the real part of the refilling as "TPA images", with the understanding that both TPA and SA can contribute (and as we show later, the sign can change experimentally).

The same principle also applies for the SPM process, as shown in Figure 2.2. SPM is a dispersive process, where the energy of the laser pulse is conserved. However, the phase of the pulse is modulated by an amount proportional to the instantaneous pulse intensity. Consequently, a new frequency component appears on the imaginary axis. When the shaped pulse (with a spectral hole in the frequency domain, Figure 2.2, top - left) enters a Kerr medium, the intense positive pulse will induce stronger SPM than the weak negative pulse (in the time domain, Figure 2.2, bottom-right). Again, the areas of the two pulses no longer exactly cancel because the intense part has a greater phase shift, resulting in new frequency components on the imaginary axis at the center of the spectrum (Figure 2.2, top-right). Effectively, the spectral hole is refilled by SPM and the added field is 90° out of phase with respect to the rest of the pulse.

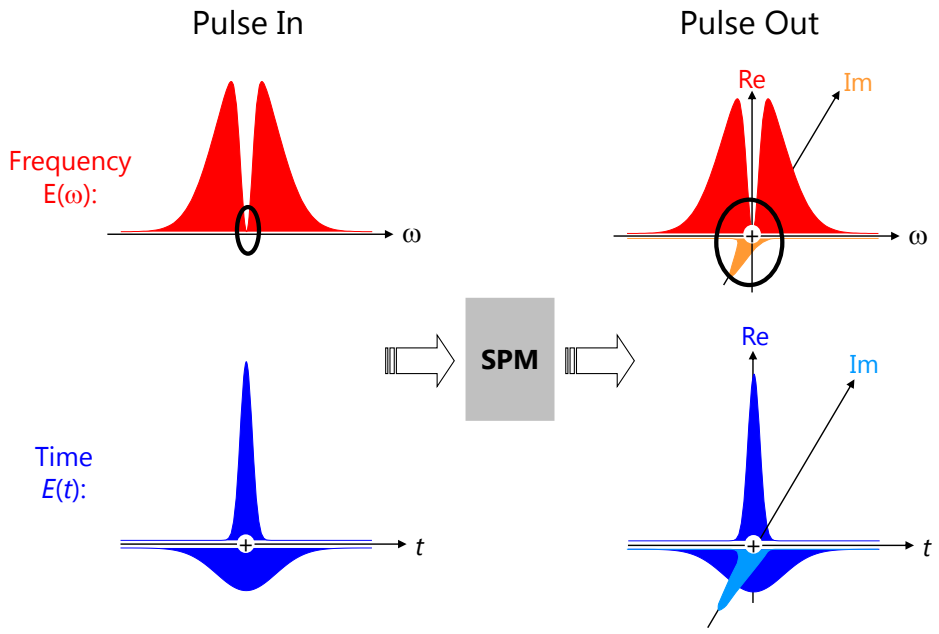

Figure 2.2: Self-phase modulation (SPM) refills the spectral-hole in a femtosecond pulse spectrum with an imaginary component.

Both TPA and SPM refill a spectral hole but with different phases: TPA, being an absorptive process, adds a field that is 180° out of phase (a negative TPA signal is in phase), whereas SPM is a dispersive process and adds a 90° out-of-phase component. These two contributions appear against zero background (Figure 2.3 (a)) and thus can be measured by a photodiode with a band-pass filter which rejects the rest of the spectrum. Nonetheless, phase sensitive homodyne detection offers higher sensitivity and the ability to discern SPM from TPA [69]. The homodyne detection is achieved by adding a phase reference in the spectral hole to serve as a local oscillator (LO), as shown in Figure 2.3 (b). The LO with a phase that cycles at a fixed frequency interferes with the generated nonlinear signal and leads to a small intensity modulation, which can be picked up by a lock-in amplifier. Once the lock-in phase is calibrated (by a pure Kerr material, e.g. glass),

the two channels of the lock-in amplifier can measure pure SPM and pure TPA signals simultaneously. This homodyne scheme also enhances the nonlinear signal by several orders of magnitude due to the amplification effect of the LO.

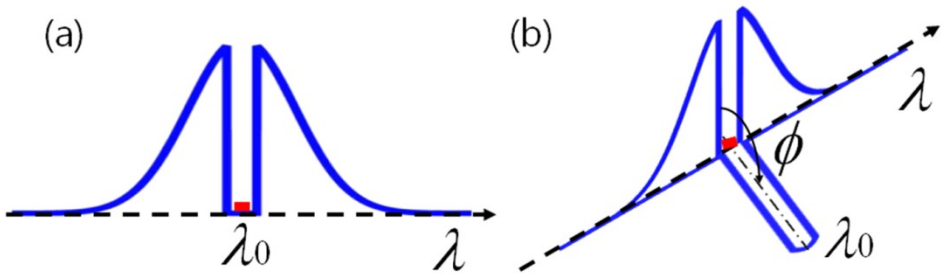

Figure 2.3: Homodyne detection with a spectral-hole pulse shape. (a), the hole-refilling signal (red square) in a spectral hole. (b), Spectral-hole with a local oscillator (blue bar at λ_0) for homodyne detection. The local oscillator in the hole (with a cycling phase ϕ) interferes with the hole-refilling signal, leading to detectable intensity modulation in the spectral hole.

2.2. Numerical calculation of SPM and TPA signals for shaped laser pulses

In nonlinear optics, the optical response of a given material can be described by a induced polarization *P(t)* as a power series in the electric field strength *E(t)* as [70]

$$\begin{aligned} P(t) &= \varepsilon_0[\chi^{(1)}E(t) + \chi^{(2)}E^2(t) + \chi^{(3)}E^3(t) + \cdots] \\ &\equiv P^{(1)}(t) + P^{(2)}(t) + P^{(3)}(t) + \cdots \end{aligned} \quad (2.1)$$

The quantities $\chi^{(2)}$ and $\chi^{(3)}$ are known as the second- and third-order nonlinear optical susceptibilities, respectively. These quantities as well as the polarization and electric field are treated as scalars for simplicity in writing Eq. (2.1). However, they are tensors in nature. The second-order nonlinear susceptibility $\chi^{(2)}$ is a third-rank tensor, with which

the second-order nonlinear polarization $\boldsymbol{P}^{(2)}$ can be expressed as $P^{(2)}_i = \chi^{(2)}_{ijk} E_j E_k$, where *i, j, k* denote the *x, y* or *z* component of the electrical field $\boldsymbol{E}$ or the polarization $\boldsymbol{P}$ (vectors). This second-order susceptibility can generate observable effects, such as second harmonic generation (SHG), but only in the limit where the media is noncentrosymmetric. This does happen in tissue (primarily from collagen) but is not very general. The third-order nonlinear susceptibility $\chi^{(3)}$ is a fourth-rank tensor, with which the third-order nonlinear polarization $\boldsymbol{P}^{(3)}$ can be expressed as $P^{(3)}_i = \chi^{(3)}_{ijkl} E_j E_k E_l$. The full expression of $\chi^{(3)}$ has 81 separate elements. However, in centrosymmetric materials, which we consider in our experiment, only 21 elements are nonzero (the three terms of the form $\chi^{(3)}_{iiii}$, and 18 of the form $\chi^{(3)}_{iijj}$, $\chi^{(3)}_{ijij}$, or $\chi^{(3)}_{ijji}$)[70]. In this thesis, we will be using a single laser pulse to generate the nonlinear signals, which is linearly polarized along the x direction (in lab coordinates), so the only tensor component we measure is $\chi^{(3)}_{xxxx}$. In the rest of this thesis we will use $\chi^{(3)}$ as a scalar to represent this specific element. Because our work puts a premium on using relatively weak laser pulses, we are principally interested in observing nonlinear effects that proceed at low powers of the electric field (yet high enough to induce a nonlinear process).

We can perform numerical simulations of the pulse propagation in a nonlinear medium to understand the signal generation in the SPM and TPA processes. A laser pulse is described by $E(z,\tau) = A(z,\tau)\exp[ik_0 z - i\omega_0 \tau] + c.c.$, where $A(z,\tau)$ is the electric field envelope as a function of time, $\tau = t - z/v_g$. Under the slowly varying amplitude

approximation, the propagation equation in a centrosymmetric medium (including up to the third-order effect) can be expressed as [71]

$$\left[\frac{1}{2k_0}\nabla_{\perp}^2 + i\partial_z - \frac{\beta_2}{2}\partial_\tau^2 + i\frac{\alpha_0}{2} + \frac{3\omega_0}{4nc}\chi^{(3)}\left|A(z,\tau)\right|^2\right]A(z,\tau) = 0. \tag{2.2}$$

Note that $\chi^{(3)}$ is complex and is frequency-dependent, but we will generally not be near a strong resonance and the frequency dependence will not be important. As we will see later, $\chi^{(3)}$ is not always independent of laser power. The TPA and SPM coefficients, α_2 and η_2, can be expressed by the imaginary and real components of the third-order nonlinear susceptibility $\chi^{(3)}$ as [71]

$$\alpha_2 = \frac{3\omega_0}{4nc}\mathrm{Im}(\chi^{(3)}),\ \eta_2 = \frac{3\omega_0}{4nc}\mathrm{Re}(\chi^{(3)}). \tag{2.3}$$

The corresponding nonlinear refractive index n_2 is thus defined as $n_2 = \eta_2 c / 2\omega_0$ such that the refractive index $n = n_0 + 2n_2|A|^2$.

The propagation equation Eq. (2.2) can be solved by numerical integration using the split-step Fourier transformation method [71]. The temporal dispersion term (β_2) is treated as a simple multiplication in the spectral domain. The remaining linear terms (α_0, denoting diffraction and attenuation) and nonlinear terms (TPA and SPM) are accounted for in the time domain by a recursive solution method for cylindrically symmetric geometries [72]. To obtain the electric field distribution in the far field, we calculated the diffraction integral of the field given by the nonlinear simulations (for our cylindrically symmetric geometry, this has the form of a Hankel transform) [59].

For imaging, focused laser beams are usually employed to achieve larger signal strength and higher spatial resolution. To quantify the hole-refilling signal for this specific geometry, we approximate the focused beam with a Gaussian spatial profile (which, by itself, is the solution for the linear propagation equation):

$$A(r,z,\tau) = A_0(z,\tau)\frac{w_0}{w_z}\exp\left[-\frac{r^2}{w_z^2} + i\Phi(r,z)\right], \tag{2.4}$$

where $w_z = w_0\Big/\sqrt{1+z^2/z_R^2}$ denotes the beam radius at a position z, and z_R is the Rayleigh length. With this Gaussian profile we can obtain an approximate expression for the hole-refilling signal by reducing the 3-dimensional equation to an "effective" 1-dimensional equation. Disregarding the effect of the nonlinearities in the medium on the spatial beam profile, we substitute Eq. (2.3) and Eq. (2.4) into Eq. (2.2) and replace the remaining radial dependence $\exp(-2r^2/w^2)$ in the nonlinear polarization term by its intensity-weighted average of 1/2 to arrive at an effective propagation equation for A_0:

$$\partial_z A_0(z,\tau) = \frac{1}{2}(i\eta_2 - \alpha_2)\frac{w_0^2}{w_z^2}\left|A_0(z,\tau)\right|^2 A_0(z,\tau), \tag{2.5}$$

Assuming a uniform nonlinearity and integrating over *z*, we can obtain a first order expression for the amplitude change as

$$\Delta A_{out}(\tau) \approx (i\eta_2 - \alpha_2)\frac{\pi}{2} z_R \left|A_{in}(\tau)\right|^2 A_{in}(\tau). \tag{2.6}$$

This expression indicates that we can approximate the case of a Gaussian beam focused well inside a uniform nonlinear medium as a plane wave traversing a similar medium of length $\pi z_R/2$.

Eq. (2.6) is the core equation we use to simulate the signal generated with shaped laser pulses. We start with a transform limited pulse $A_0(\tau)$ and apply a complex modulation mask in the spectral domain to obtain the desired pulse shape as

$$\widetilde{A}_{in}(\omega) = M(\omega) * \widetilde{A}_0(\omega). \tag{2.7}$$

When we Fourier transform this input spectrum back into the time domain and apply Eq. (2.9), we obtain the generated field. Adding this new field to the original and performing a Fourier transform yield the total output intensity in the selective spectral region under the assumption that the pulse does not change appreciably during propagation.

2.3. From a spectral-hole to the wing-cut pulse shape

To explore the optimal pulse shape for the spectral-reshaping measurement, we compute the signal generated by various pulse shapes. By varying the position and spectral width of the LO, we can obtain symmetric shapes, such as the spectral-hole case shown in Figure 2.4(a). Asymmetric shapes may also be created, such as the wing-cut pulse shape in Figure 2.4(b), where one side of the spectrum is phase-cycled and the other is kept static. For detection, we can place the detection window directly inside the LO spectrum, and we term this scheme 'LO detection'. The detection window can also be placed outside the range of the LO, because nonlinear interactions affect the entire

spectrum. In this case, since the static portion of the spectrum is used for lock-in detection. We term the latter scheme the 'static detection', where the 'local oscillator' serves to modulate the spectral changes, rather than probing a fixed spectrum with a varying reference field. By 'static detection', we can eliminate the potential instrumental background resulting from the implementation of the phase cycling while still being able to separate TPA and SPM based on their relative phase.

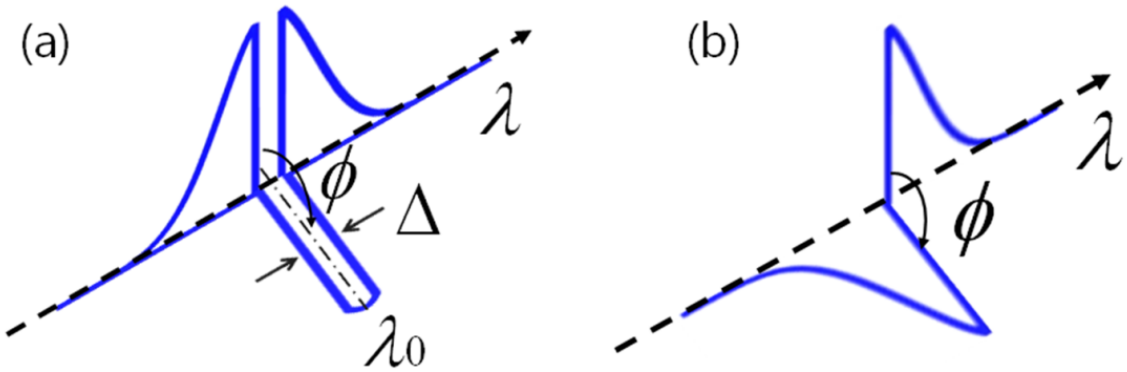

Figure 2.4: (a) The spectral-hole shape, with a phase-cycling LO in the hole. (b) The wing-cut pulse shape. Both shapes are not necessarily symmetric; in (a) the LO can be off-center, so does the edge in (b). As the spectral-hole center (λ_0) shifts towards the short wavelength and the width (Δ) of the local oscillator increases, a spectral-hole shape transforms into a wing-cut shape.

Figure 2.5 compares simulated lock-in signals for shaped pulse trains experiencing SPM (left column) and TPA (right column) as a function of the width and the position of the LO. In the top row we display signals with a detection window that is identical to the LO position (LO detection), whereas in the bottom row the remaining (static) portions of the spectrum are detected (static detection).

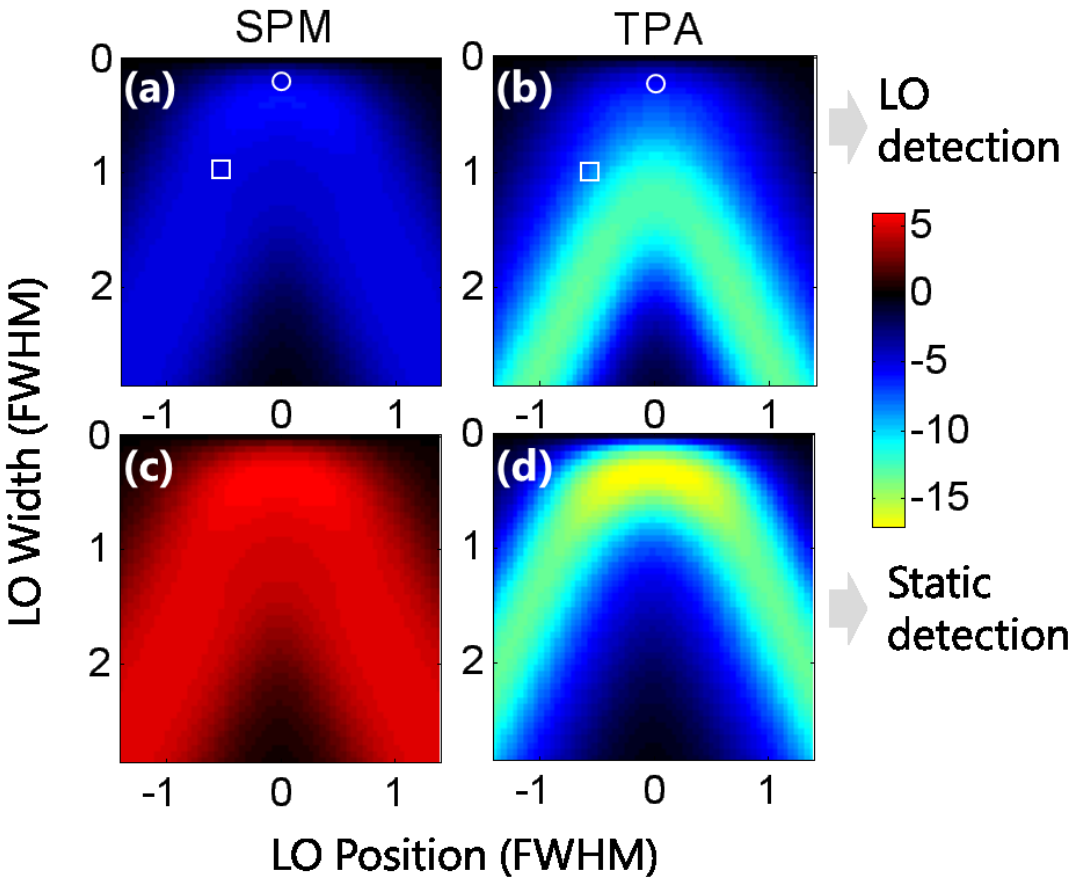

Figure 2.5: Self phase modulation (a, c) and two photon absorption (b, d) signal as functions of the LO position and the LO width (measured in units of the bandwidth (FWHM) of the unshaped pulse). In the top row (a, b) frequencies corresponding to the LO are passed for detection, while the bottom row (c, d) shows the results of detecting the static portion. Each point in these figures represents one particular pulse shape from the continuum described in Figure 2.4 (the spectral-hole shape is marked by white circles, and the wing-cut shape, squares in (a) and (c). For the calculations TPA and SPM coefficients are equal in magnitude (scaled $\alpha_2 = \eta_2$).

Several features are apparent in Figure 2.5. First, when the LO is at the center of the spectrum, both SPM and TPA signals increase with the hole width initially, then decrease, since the signal strength depends on the spectral intensity both inside and outside the LO. When the LO remains narrow the change is dominated by the increasing

LO width (the total power); however, as the width gets increasingly larger, the total intensity of the pulse is decreased with an inhomogeneous phase profile (temporal chirp). Second, for LO detection, SPM and TPA signal amplitudes scale similarly for a narrow hole (in the limit of negligible nonlinear contributions from the LO), but differ as the hole becomes wider. This scaling behavior can be discussed later in section 2.5. Basically, as the LO gets wider, sensitivity for SPM and TPA measurement is no longer equal. Third, for SPM, the LO detection and static detection yield signals of identical magnitude but opposite sign, since SPM is energy conserving and the power changes in one component of the spectrum are balanced by the other. In contrast, for TPA, this correlation does not hold due to its absorptive nature. Fourth, for static detection, maximal TPA and SPM signals are obtained with a relatively narrow LO in the center, as indicated with ovals in Figure 2.5 (c) and (d). The wing-cut geometry (indicated by rectangles) generates about 80% of the maximal TPA and 95% of the maximal SPM signal. However, this small sacrifice in signal is outweighed by the simplicity of implementation, e.g. the detected light no longer needs to be filtered with a sharp and narrow optical band-pass filter. Finally, as we will show in Chapter 3, compared to our previous LO detection setup in [60], which is represented by circles in the top center in Figure 2.5 (a) and (b), our wing-cut shapes (squares) produce larger signals by increasing the detection spectrum and much less background by measuring the static portion.

2.4. Optimizing the wing-cut pulse shape

The wing-cut pulse shape enables the measurement of SPM and TPA signals with a relatively simple apparatus; a long-pass filter is used for pulse shaping and a short-pass filter for detection. In previous calculations (Figure 2.5), we measured either all of the spectral components in the LO range or all of the spectral components outside of it. However, it is not clear which of these two schemes is the most efficient for signal detection. To find the optimal cut-off wavelengths (edges) for the short- and long-pass filters, we carried out numerical calculations, taking into account the attenuation of the long-wavelength spectrum in the phase cycling branch.

From Figure 2.6, we obtain a globally optimal configuration for both SPM and TPA signals along the diagonal of the 2D chart given by the coordinate (LPF = 0.4 FWHM, SPF = 0.4 FWHM). SPM also displays a local optimal configuration around (LPF=0.4 FWHM, SPF = -0.4 FWHM). For simplicity, we assume that the edges are infinitely sharp (100% rejection or transmission) for LPF and SPF in the numerical calculation. However, in reality, the edges of both SPF and TPF have finite widths, making the theoretical global optimum not feasible. Therefore, in our experiments we choose the local optimal configuration for SPM measurement. This is also one of the reasons why the theoretical optimal spectral-hole case in Figure 2.5 is not experimentally feasible. Given a specific LPF for pulse shaping, we have a fairly large range to tune the SPF edge (by tuning the incident angle) to achieve the best signal detection, as shown in Figure 2.6. The SPM signal may change sign under certain configurations, due to the fact that the SPM signal

generated at different frequencies has different response, and this will be discussed in the next section.

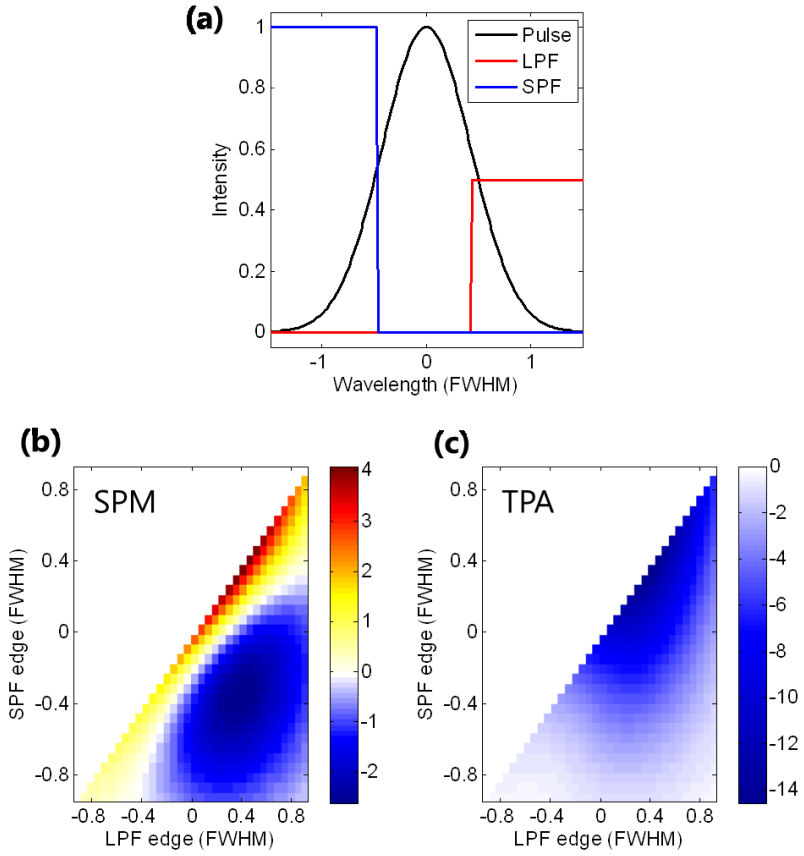

Figure 2.6: Nonlinear signals for different wing-cut pulse shapes. Parts (b) and (c) plot the SPM and TPA signals as functions of the position of the long pass filter (for pulse shaping) and the short pass filter (for detection). The configuration in (a) corresponds to the local optimum for SPM measurement, the center of the blue cloud in part (b).

2.5. Quantification of the nonlinear signal

2.5.1. Signal generation with wing-cut pulse shapes

For wing-cut pulse shapes, the generation of SPM and TPA signals can still be interpreted as a 'hole-refilling' effect of a four-wave-mixing process ($\chi^{(3)}$ effect). For plane

waves, the nonlinear polarization at the anti-Stokes frequency (the short wavelength) created in a four-wave-mixing process can be written as[70]

$$p(\omega_{AS}) \propto \chi^{(3)}(-\omega_{AS}, \omega_{\mathrm{Pr}}, \omega_P, -\omega_S) E_{\mathrm{Pr}}(\omega_{\mathrm{Pr}}) E_P(\omega_P) E_S^*(\omega_S), \tag{2.8}$$

where, ω_S, ω_P, ω_{Pr}, ω_{AS} are frequencies of the Stokes, E_S, pump, E_P, probe, E_{Pr}, and anti-Stokes beam E_{AS}. In our experiment, all frequencies are provided in a single femtosecond laser pulse and we consider only nonresonant contributions to $\chi^{(3)}$, and thus we treat $\chi^{(3)}$ as frequency-independent. For a broad spectrum, an integral over frequencies is needed:

$$p(\omega) \propto \chi^{(3)} \int_{-\infty}^{\infty} d\Omega \varepsilon(\omega - \Omega) \int_{-\infty}^{\infty} d\omega' \varepsilon(\Omega + \omega') \varepsilon^*(\omega'). \tag{2.9}$$

Here, ε is the shaped spectrum including the long-wavelength spectrum with a cycling phase $\phi = 2\pi ft$. The interference term between the short-wavelength reference and the generated nonlinear polarization can be written as

$$I_{AS} \propto \int_{\omega_{SPF}}^{\infty} d\omega \varepsilon(\omega) p^*(\omega) + c.c.. \tag{2.10}$$

where ω_{SPF} is the edge of the short-pass filter. We can write our final lock-in signal (at frequency *f*) as $I_{SPM} = \gamma_{SPM}\,\mathrm{Re}[\chi^{(3)}]$ and $I_{TPA} = \gamma_{TPA}\,\mathrm{Im}[\chi^{(3)}]$, and generally $\gamma_{SPM} \neq \gamma_{TPA}$. The ratio of the two signal components is proportional (but not equal) to the ratio of susceptibility components: $I_{TPA}/I_{SPM} = \beta\,\mathrm{Im}[\chi^{(3)}]/\mathrm{Re}[\chi^{(3)}]$. The proportionality factor β depends on the specific pulse shape, which in turn depends on the position of the edge filters and the attenuation in the phase-cycling spectrum.

For pulse shapes with a weak, narrowband LO, the sensitivity for the SPM measurement is the same as for the TPA measurement and therefore we obtain $\beta = 1$ (section 2.5.2). However, for pulse shapes where a substantial portion of the spectrum is phase-cycled, the sensitivity of SPM and TPA measurement differs. As shown in Figure 2.7, the SPM signal generated at different frequencies may switch signs. Therefore integration over a wider spectrum may lead to lower SPM signal. For TPA, there is no sign change. As a result, the simple 1-to-1 correspondence does not hold and a numerical integral is required to calculate the β value for a specific pulse shape. β also depends on the phase profile of the laser source (i.e. chirp). Further discussion of the chirp effect will be carried out in section 2.5.3. Ultimately, this β factor can be determined by measuring well calibrated samples, as will be shown in section 2.5.4.

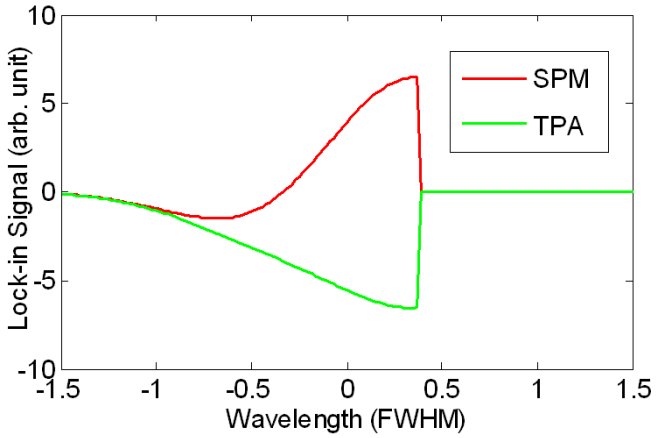

Figure 2.7: SPM and TPA signal intensity at individual wavelengths. In this calculation, the position of the LPF filter is indicated by Figure 2.6 (a); TPA and SPM coefficients are of the same magnitude ($\alpha_2 = \eta_2$).

2.5.2. The special case for a weak, narrowband local oscillator

If we only create a weak LO in the spectral-hole (i.e. the spectral width is much narrower as compared to the FWHM of the spectrum), we can assume that the LO portion of the beam is too weak to contribute to nonlinear interactions. Therefore we can avoid having to perform multiple propagations of pulses with different phases of the LO. Consequently, we only need to propagate one pulse without a LO according to Eq. (2.6) and let the resulting field interfere with a known LO of varying phase. The total field we obtain in the spectral-hole thus can be expressed as:

$$A_{out}(\tau) = A_{LO}\exp(i\phi) + (i\eta_2 - \alpha_2)\frac{\pi}{2} z_R \left|A_w(\tau)\right|^2 A_w(\tau). \tag{2.11}$$

Here, A_w is the pulse given by the static wings shown in Figure 2.3(b). The signal measured by the lock-in amplifier is the 1-f modulation of the integrated optical power in the spectral-hole, which can be written as

$$S_\phi \propto \left|A_w\right|^2 A_w A_{LO}\{\alpha_2 \cos\phi + \eta_2 \sin\phi\}. \tag{2.12}$$

These two terms are measured simultaneously by the two channels of the lock-in amplifier as the TPA signal and the SPM signal. According to Eq. (2.12), the ratio of SPM signal to TPA signal is exactly the ratio of the real component of $\chi^{(3)}$ to the imaginary component of $\chi^{(3)}$, or in other words, β=1.

2.5.3. Effects of temporal chirps

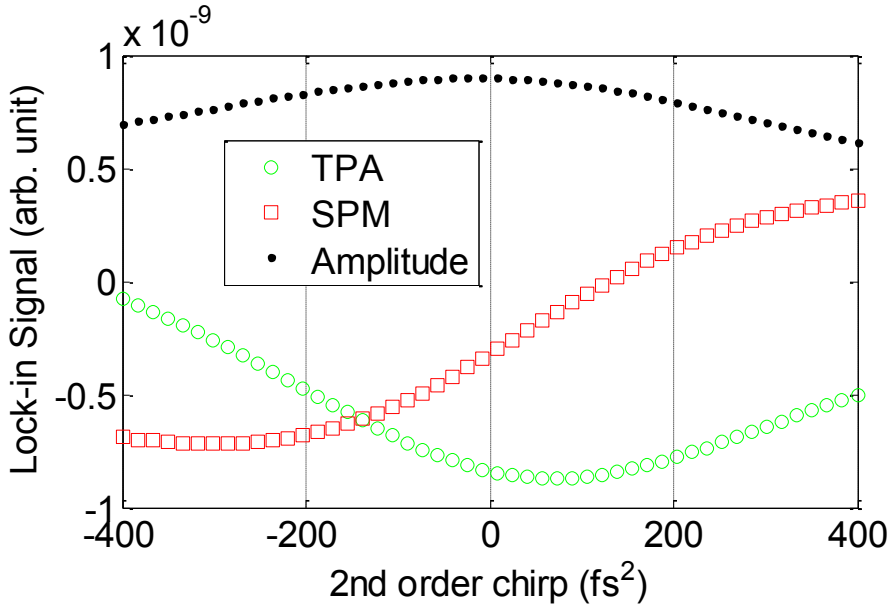

Figure 2.8: The effect of 2nd order chirp on SPM and TPA measurement. In this calculation, the configuration of filters is given by Figure 2.6 (a) and TPA and SPM coefficients are of equal magnitudes ($\alpha_2 = \eta_2$).

The signal measured with the wing-cut pulse shape is integrated over a broad spectrum; therefore the phase profile of the original spectrum may have a significant effect on the signal. We calculated the signal with an uncompensated second order chirp and plotted the result in Figure 2.8. The first order and third-order chirp have much less influence because the phase-cycling spectrum and the detected spectrum possess opposite phases and somewhat cancel out. According to Figure 2.8, the residual uncompensated 2nd order chirp mixes the signal from the SPM and TPA channels. However, since these two signal components remain orthogonal, it is always possible to choose a lock-in reference phase such that one channel measures only SPM and the

other measures only TPA. In Table 2.1, we listed the calculated reference phase for selective 2nd order chirps. The residual chirp also changes the sensitivity γ_{SPM} and γ_{TPA}, and modifies the β factor, according to Table 2.1. In our numerical simulations we observed that the maximum nonlinear signal, in terms of amplitude, is generated when the frequency components are in phase, signifying ideal experimental conditions (i.e., chirp-free).

Table 2.1: Lock-in reference phase for select values of 2nd order chirp and the corresponding β factor.

2nd order chirp (fs^2)	Reference Phase (π)	β
-400	0.519	1.256
-200	0.2775	1.329
-100	0.1422	1.347
0	0	1.358
100	-0.1422	1.357
200	-0.2775	1.345
400	-0.519	1.327

2.5.4. Determining the β factor experimentally

For our experiments, we chose filters that correspond to the broad local optimum for SPM, as shown in Figure 2.6. For this specific filter configuration, β is calculated to be 2.4 for an un-chirped input pulse. To determine β experimentally, we compare our data to Figure 4 in [59] where TPA and SPM were measured in a 20 mM solution of Rhodamine 6G (R6G) in methanol. In this reference, a narrow-hole pulse shape was used, corresponding to β=1. Using this reference and experimental data, obtained with our pulse shaper in a similar sample, we obtain β = 1.7. This value is smaller than the

calculated value for a transform-limited pulse (β = 2.4). We attribute this discrepancy to residual uncompensated chirp in our system (for example, second order chirp that increases the pulse duration to 1.5 times the transform-limited case would yield β = 1.6). Even in the absence of a reference standard, β can be calibrated by detecting only a very small portion of the spectrum, albeit at the expense of lower signal levels.

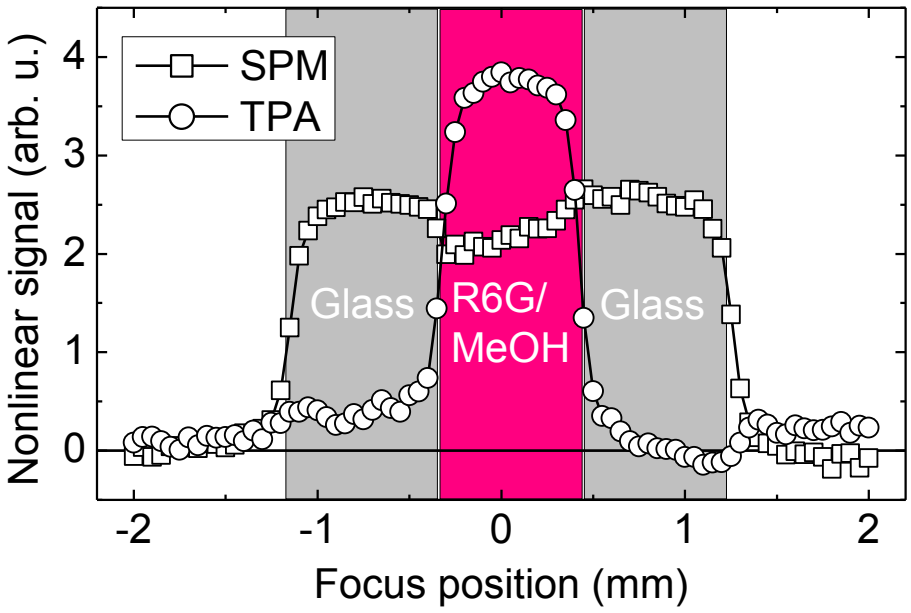

Figure 2.9: SPM and TPA measurement of a quartz cuvette filled with 20 mM Rhodamine 6G in methanol. The beam is focused by a 10x objective, 0.25 NA. Input power is 1.5 mW and the lock-in time constant is 100 ms. From this result, β is calibrated to be 1.7.

2.6. Conclusion

In conclusion, we have systematically studied the signal generation with various pulse shapes for the spectral reshaping technique. We have shown the smooth transition from the spectral-hole shape to the wing-cut shape and obtained the optimal pulse

shape, while also considering the ease of implementation. The wing-cut pulse shape simultaneously measures SPM and TPA but with different sensitivity. The ratio between SPM and TPA detection sensitivity can be experimentally calibrated, making our technique a truly quantitative imaging method.

3. Rapid pulse shaper for spectral-reshaping imaging

This chapter focuses on the innovation of a new rapid pulse shaper which creates the wing-cut pulse shape described in Chapter 2 at MHz rates. We will first introduce the basic knowledge behind femtosecond pulse shaping and several principles for designing a rapid pulse shaper. We will then explain how the previous rapid pulse shaper [60] works and why it fails to provide the required sensitivity for imaging. Following a detailed description of the new rapid pulse shaper, we will briefly introduce the rest of the experimental setup, the instrument control and the data acquisition process. Several experimental results will be presented, to demonstrate the validity and usefulness of the new rapid pulse shaper.

3.1. Femtosecond laser pulse shaping

The most intuitive way of modifying the shape of a laser pulse (a packet of electromagnetic waves) is through wave modulation in the time domain, similar to the way in which amplitude-modulation radio broadcasting works. According to the Fourier theorem, one can equivalently shape a pulse in the spectral domain or the Fourier space, e.g. FM radios. In the latter case, the laser spectrum is spatially dispersed such that a spatial mask can be applied to selectively alter individual frequency components of the laser pulse. Since there is no physical process that can be turned on and off fast enough, most successful femtosecond laser pulse shaping techniques operate in the spectral domain. Advancements in laser pulse shaping techniques over the past few decades

have enabled the generation of laser pulses with arbitrary waveforms [73, 74], thus making a strong impact in areas such as nonlinear fiber optics [75, 76], high-field physics [77-79], and ultrafast spectroscopy and microscopy [42, 44, 45, 49, 73, 80-82] .

3.1.1. 4-f pulse shaper for spectral pulse shaping

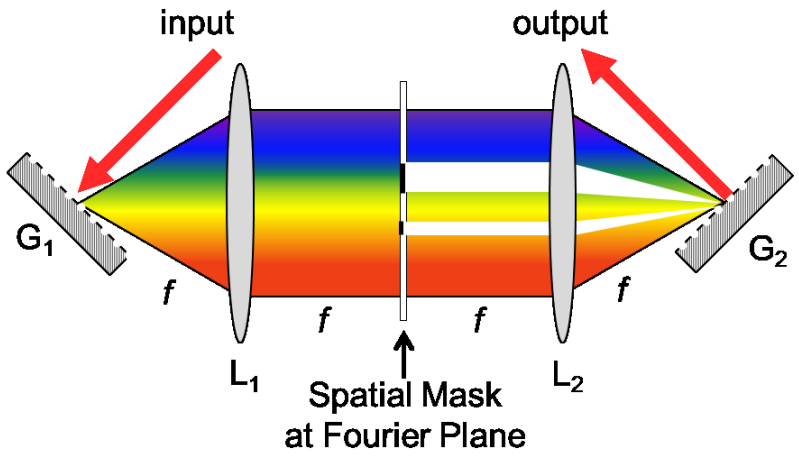

Figure 3.1: Schematic of a standard 4-f configuration (top view). G_1 and G_2 are the gratings to disperse and recombine input and output laser pulse. L_1 and L_2 are the input and output lenses with focal length *f*. The spatial mask is placed at the Fourier plane.

A femtosecond laser pulse shaper usually takes the 4-f configuration illustrated in Figure 3.1 [74]. A diffraction grating (G_1) is placed at the back focal plane of the input lens (L_1) with focal length *f*. G_1 disperses the input beam into its frequency components, mapping color onto an angle. This angularly dispersed beam is then collimated by L_1 causing different frequency components to become parallel to each other, focusing each component to the Fourier plane, thus mapping color onto a spatial position. The amplitude and phase of each individual frequency component can be modulated

(simultaneously or separately) by placing a spatial mask in the focal plane (or Fourier plane). After the modulation, these spatially dispersed frequency components are collected by lens L_2, placed one focal length away from the Fourier plane, and consequently focused onto and recombined by grating G_2 into a single beam. This symmetric setup prevents undesired modifications of the shaped pulse, e.g. spatial and temporal chirp. In implementation, reflected gratings can be replaced by transmission gratings or prisms and the pair of lenses can also be substituted by a pair of curved mirrors. Our implementation is shown in Figure 3.2 and employs all reflective optical elements to avoid chromatic aberration from the lenses and to make our setup more compact.

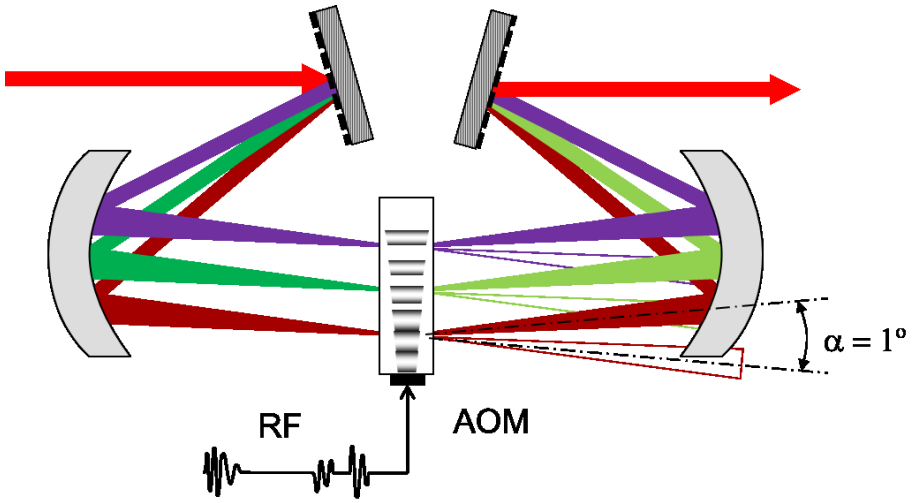

Figure 3.2: Schematic of an acousto-optic modulator (AOM) based 4-f pulse shaper. The first order diffraction beam is employed for pulse shaping. RF denotes the radiofrequency pulse; α is the diffraction angle.

For a simple pulse shape (e.g. a partially masked spectrum), a fixed spatial mask in the focal plane could be used. For many applications, however, programmable spatial

masks that can manipulate both the amplitude and phase of the light are desired. Two instruments are commonly used for this purpose, liquid crystal spatial light modulators (LCLSMs) and acousto-optical modulators (AOMs). Both devices are able to manufacture laser pulses into arbitrary waveforms. AOM-based pulse shapers were invented by Warren's group; they enabled fast update of the waveform which is essential to our spectral reshaping technique, and thus these are our main focus in this dissertation [83]. For more information on the LCLSM-based pulse shaper, please refer to reference [74].

In an AOM, a transducer is attached to a tellurium dioxide crystal as shown in Figure 3.2. A radiofrequency (RF) pulse drives the transducer and creates an acoustic wave in the crystal which acts as a diffraction grating for the incoming femtosecond laser beam. This grating is effectively static for the femtosecond laser pulse (the acoustic wave propagates only 10^{-5} of the acoustic wavelength during the 100 fs duration given a speed of the acoustic wave at 4.2 km/s). Nevertheless, the phase of the diffracted beam (employed for pulse shaping) is shifted by the phase of the acoustic wave in which the beam is diffracted, while its amplitude is controlled by the local intensity of the acoustic wave. Therefore we can impart any modulation onto the spectrum of the input laser pulse by programming the waveform of the radiofrequency pulse.

One major advantage of an AOM-based pulse shaper, as compared to a LCSLM-based one, is its dynamic feature: the pulse shape can be updated at a rate of 200 kHz (it takes the acoustic wave about 5 μs to propagate over a 2 cm AOM crystal), while the LCLSM can only operate at a few hundred Hertz at most. This means we can shape

individual pulses coming from an amplified laser system operating at the kilohertz level. A shorter crystal can increase the update rate but with a trade-off in spectral resolution.

For the discussion in this dissertation, we limit ourselves to the 'traditional' pulse shapers in a sense that the pulses are still sparse in time: there is huge time gap between pulses. Combining the pulse shaping methods we discussed here with frequency comb technology, which produces optical pulse trains with a well-defined frequency spectrum, enables the generation of optical arbitrary waveforms. To learn more about this topic please refer to a recent review by Cundiff and Weiner [84].

3.1.2. Rapid pulse shaper with a 4-f configuration

Manufacturing each individual pulse from a mode-locked laser operating at an 80 MHz rate into an arbitrary shape is extremely challenging, if not impossible, due to the inadequate update rate of the programmable spatial masks. However, it is feasible for the specific pulse shapes we discussed in Chapter 2, since only the phase of selected spectral components is rapidly cycling at the MHz rate and the spectral selection remains the same from pulse to pulse. If we use two separate units to realize two functions, spectral selection and phase cycling, rapid pulse shaping can be achieved. This basic principle makes the design of a rapid pulse shaper at MHz rates feasible.

In our first generation rapid pulse shaper for the hole-refilling measurement [60] an AOM-based telescope is employed to impose the cycling phase and a folded 4-f pulse shaper is used for spectral selection. As shown in Figure 3.3, an AOM is driven in

the continuous mode acts as a frequency shifter for the diffracted beam (upper arm, or the local oscillator (LO) arm). The AOM splits the input pulse train into two arms and recombines them after both beams are shaped individually and retro-reflected. The diffracted and undiffracted beams are vertically displaced at an angle twice the Bragg angle of the acoustic wave grating. Both beams are collimated and sent into a static folded 4-f pulse shaper, which we will call the spectral selection unit. The beams are spectrally dispersed using a diffraction grating (DG) and focused using a cylindrical lens (CL) onto a large end mirror (M) which is placed at the Fourier plane. This folded 4-f configuration guarantees minimum beam distortion. A fixed mask is placed in front of the end mirror to create a hole in the undiffracted beam (the lower one), producing the static wings for the desired pulse shape. The mask is placed as close as possible to the mirror to obtain the highest spectral resolution. No spatial mask is needed for the LO, since the LO is relatively weak as compared to the wings. The overlap of the portion outside the hole will be eventually rejected by the band-pass filter for detection. Note that both beams travel through the same optical components (common path mode) achieving interferometric stability.

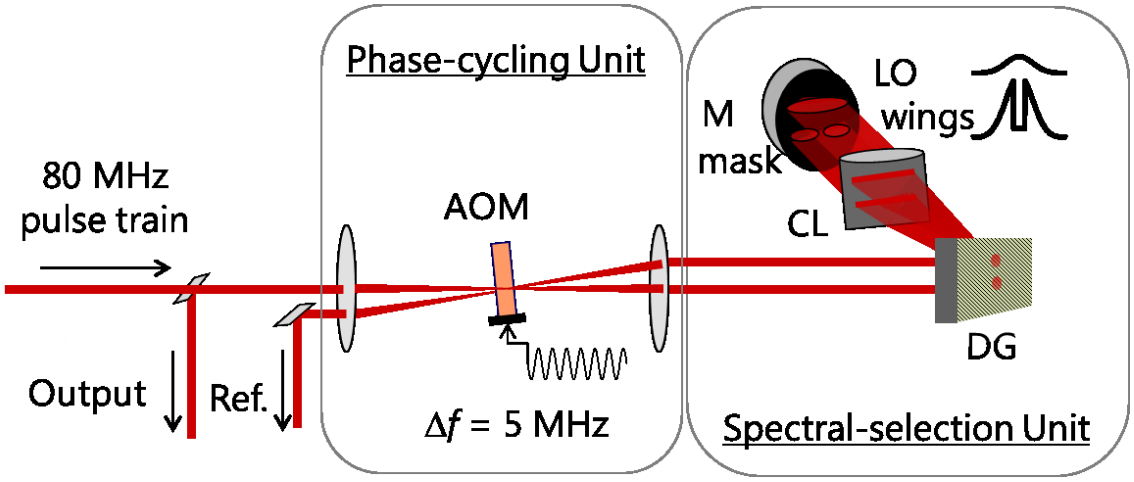

Figure 3.3: Rapid pulse shaping with a common-mode interferometric pulse shaper with a 4-f configuration. The acousto-optic modulator (AOM) acts as the splitter and combiner for the interferometer arms. It also shifts the frequency of the local oscillator (LO) arm. The spectral selection is performed by the folded 4-f pulse shaper. DG, diffraction grating; CL, cylindrical lens; M, end mirror. The output is vertically displaced by tilting the end mirror and isolated using a pick-off mirror.

When the reflected beams are recombined by the AOM, they are diffracted for the second time. The output consists of the undiffracted wings and the double-diffracted LO. The end mirror is slightly titled to provide a vertical offset such that the output can be picked off by a mirror. If the AOM is driven at a frequency $f_{RF} = mf_{rep}+\Delta f$, where m is an integer and f_{rep} is the pulse repetition rate, then the double-diffracted LO beam is frequency shifted by $2\Delta f$. Therefore, the relative spectral phase of the LO (double-diffracted) rotates at a frequency of $2\Delta f$ with respect to the wings (undiffracted) of the pulse spectrum. This creates the required spectral-hole pulse shape (with LO) for the spectral reshaping technique (hole-refilling), without any AOM update rate restrictions.

The two single-diffracted beams (the undiffracted LO and the diffracted wings from the second time through) can be collected and serve as an optical reference. The

forward diffraction (first time through) and the backward diffraction (second time through) creates the same amount of frequency shift (Δf) but with opposite sign. Due to the spectral overlap outside the spectral hole, these two single diffracted beams interfere and create an intensity modulation at $2\Delta f$. This modulated signal can be recorded by a photodetector and be fed into the lock-in amplifier as a reference. This optical reference is phase-locked to the output beam and thus substantially improves the stability of the lock-in detection.

With this 4-f rapid pulse shaper pumped by an 80 MHz Ti:Sapphire mode-locked laser, we measured TPA and SPM signals of a quartz cuvette filled with 30 mM Rhodamine 6G (R6G). The sample was translated through the laser focal volume, created by a 10x objective, to obtain a z-scan trace. For comparison, a z-scan trace obtained with a 4-f AOM-based pulse shaper shown in Figure 3.2 pumped by an amplified laser system (Coherent, RegA) is also displayed in Figure 3.4(a). TPA and SPM signals can be clearly distinguished: TPA is only present in the sample containing R6G, while SPM is present in the sample as well as the glass, as indicated by the shaded regions in Figure 3.4 (a). Figure 3.4(b) displays results obtained with the mode-locked laser and the interferometric pulse shaper operating at a 10 MHz modulation frequency (Δf = 5 MHz). Similar qualitative features are observed when comparing the data in Figure 3.4 (a) and (b). However, in the mode-locked case, a significant background is present relative to the signal intensity. This background can be suppressed by measuring the double-frequency signal (20 MHz), as shown in Figure 3.4 (c), but at the expense of reducing the absolute

signal. Note that this result is achieved by 50 mW laser power with 5 ms averaging. This sensitivity is not acceptable for imaging in tissue samples, which has much background noise. To perform SPM/TPA imaging at a moderate power level (a few mW) the background has to be significantly suppressed.

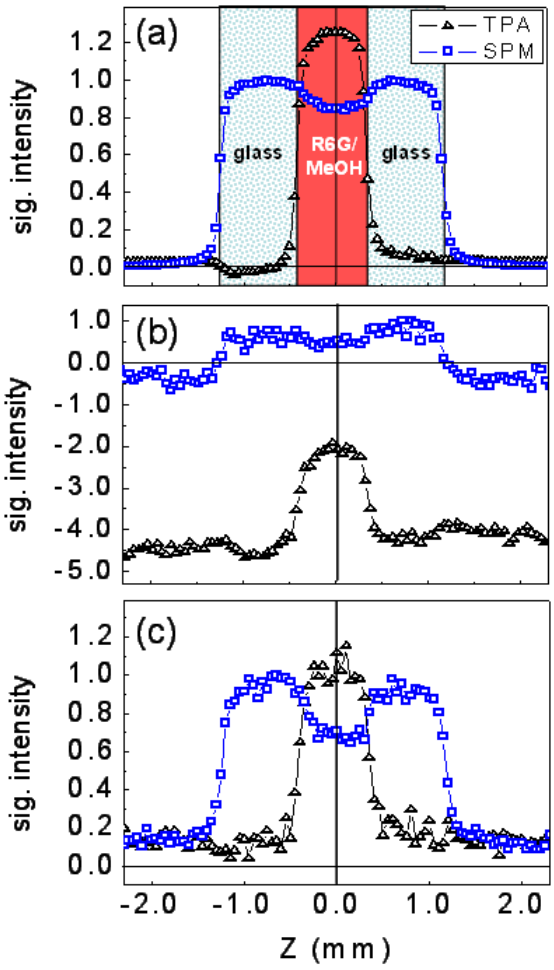

Figure 3.4: TPA and SPM measurements in a quartz cuvette filled with 30mM Rhodamine 6G in methanol using an amplified laser with 0.25 mW input power detected at 5 kHz (a) and a mode-locked laser with 52.5 mW input power detected at 10 MHz (b) and 20 MHz (c). The lock-in time constant was set to 3 ms for all experiments (only for comparison). Adopted from Ref. [60].

3.1.3. Origin of the background

The undesired background shown in Figure 3.4 (b) has two origins – spectral leakage and intensity fluctuation. Due to the finite resolution one can achieve in the 4-f pulse shaper, there is always a spectral overlap at the edges of the spectral hole, no matter how sharp the spatial mask. Consequently, the two rising edges of the band-pass filter in detection need to be steep; otherwise, even a slight leakage into the detection window can induce enormous background in detection. The leakage can be reduced by increasing the width of the spectral hole while maintaining the window for detection. However, the relative signal is also reduced, since the pulse energy decreases and the spectral reshaping induces the largest refilling near the edges. Because of this significant tradeoff between the background suppression and signal generation, tuning the width of the spectral hole can only marginally improve the signal-to-background ratio (SBR).

The second component of the background, which is the major contribution, comes from the unwanted intensity modulation in the LO beam introduced by the AOM. In the ideal case, the RF pulse should excite a stable propagating acoustic wave in the crystal, which only introduces phase shift in the diffracted beam. However, in reality, two factors may induce amplitude fluctuation in the beam: the standing wave created by the reflection of the acoustic wave at the end of the crystal and the vibration caused by the environment or the RF wave itself. Even though it is very difficult to isolate and characterize the contribution from individual factors, these two together introduce intensity fluctuation around 10^{-4} in the laser pulse over a wide range of frequencies at

MHz rates. It is extremely difficult to reduce this fluctuation in the previous design. To prevent the formation of a standing wave, the end of the AOM crystal is cut at a particular angle and decorated with additional damping material. However, even in the optimum case for a typical AOM, the return loss is still about 40dB or 10^{-4}. In addition, even if it is possible to isolate our AOM from its environmental vibrations, the RF input still acts as a source of disturbance. An intensity fluctuation at the level of10^{-4} is acceptable for various other applications that use AOMs, but it does not fulfill the requirement for our nonlinear measurement. The signal we measure at a moderate laser power (e.g. 5 mW input power produces a 10^{-6} nonlinear signal) is well below this level.

3.2. The reconfigured rapid pulse shaper

3.2.1. Instrumental design

To suppress the background in our lock-in detection to a tolerable level, we developed a new rapid pulse shaper. The key of the re-design is that the probe (the spectral portion we measure) should not undergo any dynamic optical elements (i.e. the AOM). This is made possible by switching from the spectral-hole shape to the wing-cut pulse shape, which enables us to separate the spectrum with an edge filter before the beam enters the dynamic phase-cycling unit (the AOM).

The design of our new rapid pulse shaper is illustrated in Figure 3.5. A long-pass edge filter (LPF, Semrock LP808RU), with the transmission edge angle-tuned to 810 nm, splits the input laser beam (80 MHz Ti: Sapphire oscillator, 25 nm FWHM centered at 808

nm) into two paths. The transmitted long wavelength component passes through an AOM (Isomet, M1135-T80L), which is driven by an 82 MHz continuous RF wave. Since the first-order diffracted output of the AOM experiences a frequency shift, phase-cycling is introduced at 2 MHz in this path (4 MHz after double-passing the AOM). Both arms are back-reflected, temporally and spatially overlapped on the LPF, and coupled into a home-built laser scanning microscope (as will be discussed later). For detection, a short pass filter (SPF, Omega 791AESP) with its edge at 791 nm (away from the LPF edge at 810 nm) completely rejects the phase-cycling spectral component. With this setup, the detected light does not undergo any modulation before entering the sample. Therefore, no detrimental instrument background is introduced.

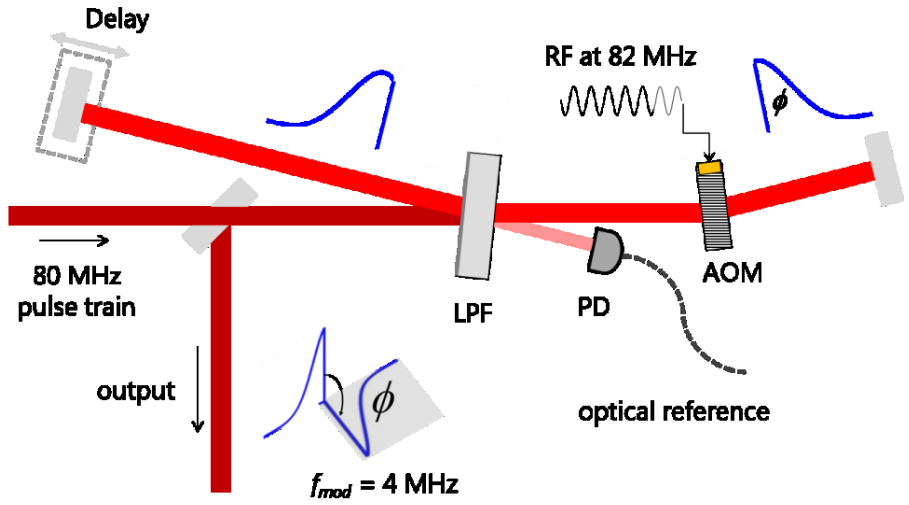

Figure 3.5: Schematic of the new rapid pulse shaper. LPF, long-pass filter; SPF, short-pass filter; PD, photo detector. The phase of the long wavelength part is shifted when going through the AOM.

To achieve better performance in scattering media, we choose to cycle the phase of the long wavelength spectrum and detect the short wavelength component. If we

choose the opposite case (in the previous chapter we have shown these cases to be equivalent in theory), the scattered photons coming out from the sample at arbitrary angles (deviation from normal incidence) could pass the long-pass filter and degrade the signal. This is because the transmission curve shifts towards short wavelengths when photons are not at normal incidence, as shown in Figure 3.6(a). As a result, photons from the phase-cycled short wavelength spectrum that come out of a scattering media at various angles may pass the filter. Using a short-pass filter can circumvent this problem because the edge of the transmission curve of a short-pass filter also shifts towards short wavelength. The modulated long wavelength photons can never get through the filter, leading to a much cleaner signal. This setting also makes the epi-mode TPA/SPM imaging possible.

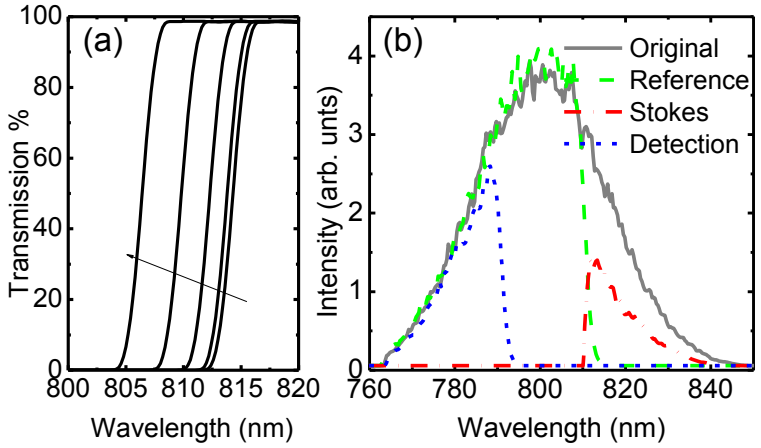

Figure 3.6: Spectral separation for the wing-cut pulse shape. Part (a) shows the transmission curves of the long-pass filter at different incident angles (0, 4, 8, 12 and 16 degree, as indicated by the arrow). Part (b) plots the separated (the reference and the Stokes), recombined, and detection spectra in our experiment.

3.2.2. Optically-derived reference for the lock-in detection

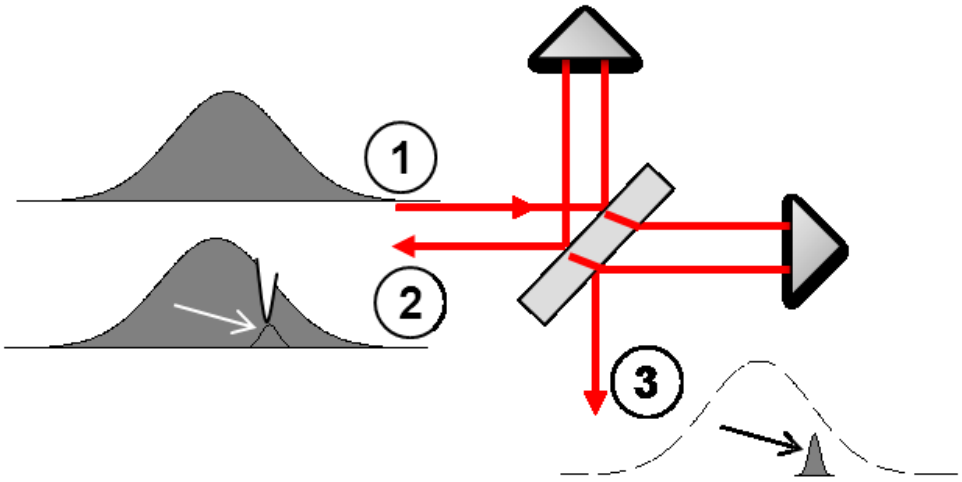

Figure 3.7: Generation of the optical reference. (1), Input spectrum; (2), output spectrum (of the shaped pulse); (3), spectrum of the optical reference. Arrows point to the overlapped spectrum.

To ensure the phase stability of the lock-in detection, we derived a phase-locked optical reference from the new pulse shaper. While the radio-frequency reference generated from a synchronized function generator is in principle suitable, stable phase-locking is extremely difficult to maintain due to the interferometric design of the shaper. Due to the finite spectral width of the long-pass filter, we can use the leakage of the recombined beams as an optical reference. As shown in Figure 3.6 (a), at a typical incident angle, the rising edge of the transmission curve is about 3.6 nm wide (transmission shifts from 5% to 95%). As a result, the spectra of the transmitted and reflected beams are partially overlapped. The finite-width rising edge also allows leakage into the remaining output arm of the interferometer, labeled No. 3 in Figure 3.7, resulting in an intensity modulation at 4 MHz, the same frequency of the signal we are

detecting. This intensity modulation can be directly measured by a photo detector and be fed to the lock-in amplifier as a reference. This optically derived reference ensures that the measured nonlinear optical signal is phase-locked. In addition, we can build the rapid pulse shaper with a small footprint (less than 1' x 1'), with very few elements and seal it in a box, thus minimizing environmental turbulence, such as air flow or dust.

3.3. Experimental setup and data acquisition

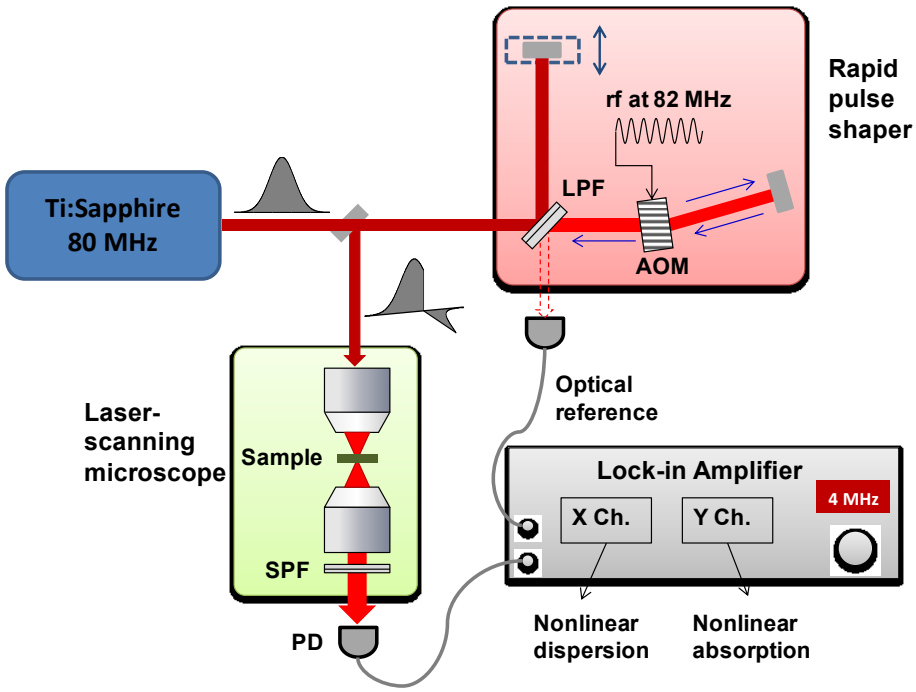

Figure 3.8: Experimental setup used for two-photon absorption and self-phase modulation imaging. SPF, short-pass filter; AOM, acousto-optic modulator. The edge of the SPF is shifted to reject the phase-cycling portion of the spectrum.

The experimental setup for performing nonlinear optical imaging is shown in Figure 3.8. In addition to the new rapid pulse shaper, the development of a laser scanning microscope is also an essential part in our experiment. Laser scanning

microscopes are commercially available from a number of microscope companies. However, they are usually expensive and do not allow the customizability required for our nonlinear imaging. Therefore, we have developed a multi-mode and multi contrast laser scanning microscope based on the design described in Ref. [46]. The core of a laser scanning microscope is the scan system, which delivers a collimated laser beam at various angles onto the back aperture of an infinity corrected objective. The infinity corrected objective maps the angle to position on the focal plane. By changing the angle, the focal spot can be scanned across the sample.

We detect our nonlinear signals (SPM and TPA) in the microscope as follows. The beam coming out of the condenser is sent through the short-pass filter (which is angle-dependent) and detected by an amplified silicon photodetector (PDA36A, Thorlabs). This beam is not de-scanned; therefore, we need to image the back aperture of the objective onto the detector with a combination of lenses for minimum spatial deviations during scanning. The filter should also be placed at the minimum deviation position to obtain a position-independent filter performance. The signal from the detector is analyzed by a lock-in amplifier (SRS844, Stanford Research Systems) synchronized to the optical reference. The X and Y channels from the lock–in are fed into a National Instruments DAQ module (PXI-6259) to provide SPM and TPA images. The DAQ module features simultaneous 32 channels sampling as well as four output channels, two of which are used for controlling the scan mirrors.

In addition to SPM/TPA images, we also simultaneously register the linear transmission images and the TPF images. The transmission images are detected in forward mode. A small amount of the output beam is directed by a thin coverslip onto the transmission photodetector (PDA36), and then the signal is fed directly into the DAQ module. The TPF image is collected in the epi-mode with a long-pass dichroic filter (FF685, Semrock) placed right before the objective and a PMT (Hamamatsu PMT C6270). The signal from the PMT is also fed directly into the DAQ module.

We built our own image scanning software with LabWindows/CVI (National Instruments) for instrument control and data acquisition. The main function of the program is to output waveforms to the scan mirrors to raster scan the beam and synchronously read out data from the DAQ module (4 input channels in total). The software also controls the XYZ sample stage constructed using three motorized scanning stages attached to a GPIB-controlled motion driver (ESP7000, Newport). While acquiring a Z-stack of images, the z-stage is moved along the axial axis.

3.4. Experimental results and discussion

3.4.1. SPM/TPA spectroscopy of liquid samples

To test the performance of the new rapid pulse shaper, we measured TPA and SPM signals in a quartz cuvette filled with 30 mM Rhodamine 6G in methanol using a mode-locked laser. The cuvette is translated through the focus created by a 10x objective. As shown in Figure 3.9, TPA is present only in the sample containing R6G,

while SPM is present in the sample as well as the surrounding glass. Compared to the result obtained with our previous rapid pulse shaper shown in Figure 3.4 [60], the new rapid pulse shaper demonstrate much higher performance: 40 times improvement in signal to background (SBR) ratio is achieved with 1/20 laser power; the signal to noise ratio (SNR) is also increased by a factor of 20 under similar conditions. Here the background is defined as the 'signal' in the SPM channel when the focal spot is parked in air. The noise is defined as the standard deviation of the signal, which can be extracted from time traces of the detected signal (approximately reflected by the variation of the signal in glass in Figure 3.9).

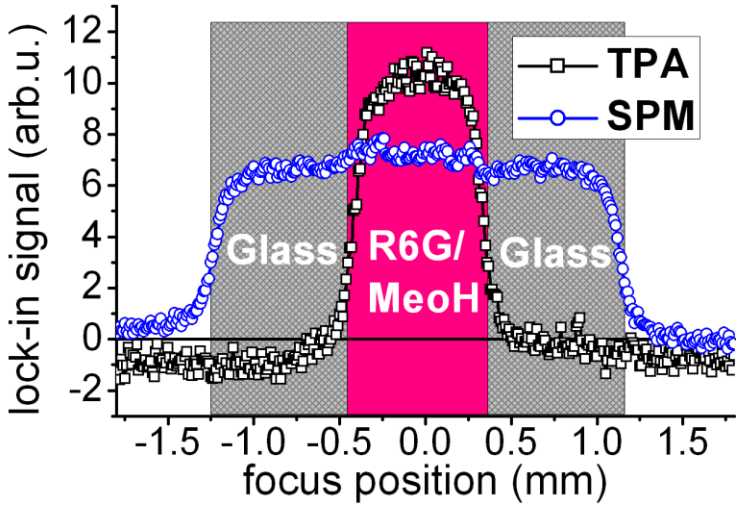

Figure 3.9: TPA and SPM measurements in a quartz cuvette filled with 30 mM Rhodamine 6G in methanol using a mode-locked laser with 2.5 mW input power and a 1 ms lock-in time constant. The objective is 10x, 0.25 NA.

3.4.2. Imaging gold nanostars in vitro

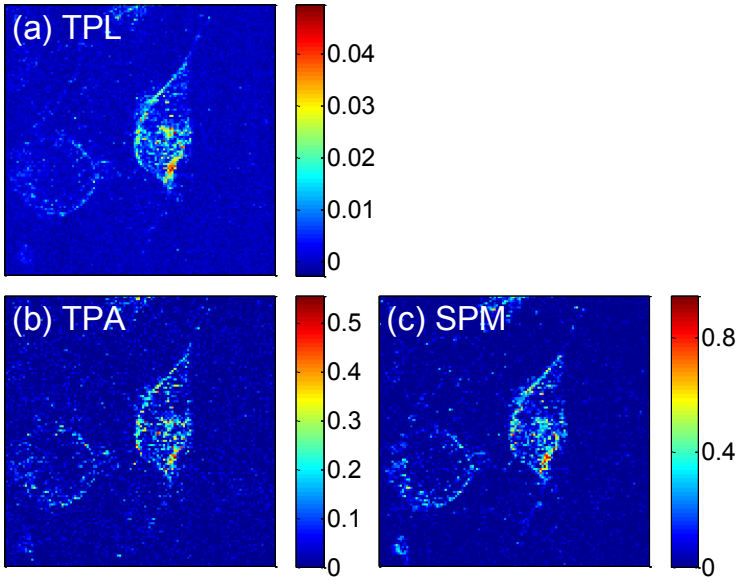

Figure 3.10: Multicontrast nonlinear optical images of BT549 breast cancer cells incubated with gold nanostars: (a), two-photon luminescence; (b), two-photon absorption; (c), self-phase modulation. The lock-in phase was adjusted according to the SPM signal generated in the glass coverslip. Images (a)-(c) were acquired simultaneously (dimensions 100×100 μm, 0.5 mW input power, 8-frame average, and acquisition time 3.2 s per frame)

To demonstrate the applicability of our technique for nonlinear optical microscopy, we acquired TPA and SPM images on BT549 breast cancer cells that were incubated for 24 h with silica-coated and TAT-tagged gold nanostars, displayed in Figure 3.10 (b) and (c), respectively [85]. Nanoparticles can have much larger and tunable nonlinear optical coefficients than bulk material due to quantum confinement effects, and thus are commonly used as nonlinear optical imaging agents [67, 86, 87]. The TPA and SPM images in Figure 3.10 show clear and highly correlated contrast. For comparison, we also acquired co-registered two-photon luminescence (TPL) images of

the same sample, shown in Figure 3.10 (a). From the SPM, TPA, and TPL images, we can see that the nanostars predominantly accumulate in the cytoplasm. It is important to note that, unlike two-photon luminescence imaging, TPA and SPM can be used for imaging of non-luminescent targets.

3.4.3. Quantum yield imaging

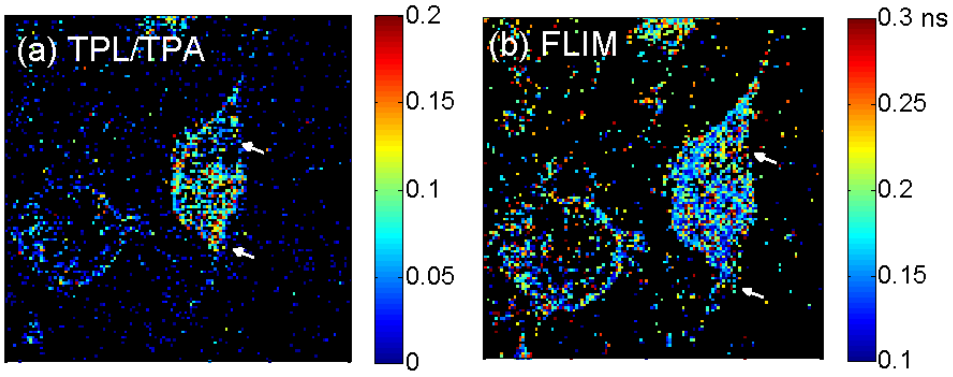

Figure 3.11: Comparison of quantum-yield imaging with fluorescence lifetime imaging. (a), Map of TPL to TPA ratio (taken from Figure 10 (b) and (c); the dimension is 100×100 μm). (b), FLIM image of the same cell taken with an Olympus FV1000 multiphoton microscope and PicoHarp 300 counting electronics (80 MHz, 810 nm, 0.8 mW input power and 120 s acquisition time, and the dimension is 80×80 μm).

We also plot the ratio of TPL to TPA in Figure 3.11 (a), reflecting the quantum yield for two-photon luminescence (or fluorescence in the case of dyes), which could be used to study the environmental effects on optical imaging agents or to study the quantum yield properties of individual nanoparticles. The rapid measurement of quantum yield could have advantages in Förster resonance energy transfer (FRET) experiments [65, 88]. Commonly, transfer efficiency is determined by relative measurements of the fluorescence (or fluorescence lifetime) of a donor fluorophore in

the presence and absence of an acceptor molecule. In a simple donor-acceptor model, the transfer efficiency is complementary to the quantum yield (describing the two possible pathways of transfer or fluorescence). Hence, a rapid and direct measurement of quantum yield could give the transfer efficiency without relative measurements at different acceptor configurations. In the case of nanoparticles, the quantum yield has a wide distribution due to variations in size and shape. This inhomogeneity masks the environmental effects in our current cell sample. However, in cases where a single particle or a few-nanoparticle aggregate can be tracked [87], the quantum yield images could provide information on nanoparticle properties and on environmental influences.

As a comparison, we also acquired a fluorescent life time image (FLIM) of the same cell (Figure 3.11 (b)) [13-15]. Both the quantum yield and FLIM images are dominated by the inhomogeneity of nanostar lifetimes. This heterogeneity prevents fine-scale image co-registration, but a large-scale correlation between fluorescence lifetime and quantum yield in the areas marked by arrows can be observed, in which low quantum yield seems to correspond to longer lifetimes.

3.5. Conclusion

In summary, we have developed a rapid pulse shaper based on the wing-cut pulse shape. By cycling the phase of one half of the spectrum and detecting the intensity modulation in the other half our new pulse shaper enables rapid, low-background SPM and TPA imaging with simple implementation using widely available mode-locked lasers.

The validity of our microscopy technique is demonstrated by SPM/TPA measurements in R6G solutions as well as the *in vitro* imaging of breast cancer cells incubated with gold nanoparticles. With the ability to co-register both TPA and TPF images, our multi-contrast nonlinear microscope can produce quantum-yield images, which is potentially very useful for biomedical research and worth further exploration.

4. Graphene Imaging with femtosecond spectral reshaping

In this chapter, a phase-cycling nonlinear spectral reshaping imaging technique is applied to study the third-order nonlinear optical susceptibility of graphene and to image graphene, both isolated and in a biomedical environment. Specifically, we measure the complex $\chi^{(3)}$ of graphene and investigate its saturation behavior. We find that the high nonlinear optical contrast enables us to count the number of layers in graphene, which permits characterization of graphene samples made using different methods, and allows us to distinguish and track graphene flakes *in vitro*. Partial content of this chapter has been published in Nano Letters[89].

4.1. Introduction

The novel physical and chemical properties of graphene and its derivatives have stimulated interest in biological and medical applications, including drug delivery and cancer therapy [90-92], biological sensing [93, 94] and tissue engineering [95]. The current challenges associated with applying graphene to biological systems include its potential adverse health impact [96, 97], which further motivates investigation of graphene in a biomedical environment. Unfortunately, most imaging techniques that are capable of resolving graphene face significant challenges. Atomic resolution techniques are time consuming [98], invasive and not applicable to bulk tissue or *in vivo* imaging. Conventional optical microscopy gives strong contrast only on select substrates [99-101].

Linear and nonlinear fluorescence imaging methods have been demonstrated with graphene oxide (GO) [102, 103], but its luminescence is very weak[104], even if functionalized by dyes (graphene quenches dyes' fluorescence) [105]. Spatially resolved Raman spectroscopy of graphene [19, 20] is compromised by tissue scattering. Here, we overcome these limitations using a novel type of nonlinear microscopy that is based on femtosecond laser spectral reshaping. This method, described below, can quantitatively characterize and image graphene in highly scattering environments, such as tissue. We also use this technique to provide a detailed study of the nonlinear optical response of graphene, a critical step for various applications including nanophotonics and optoelectronics [106].

4.2. Nonlinear optical signal in graphene

4.2.1. Spectral-reshaping imaging

The unique linear dispersion relation of graphene induces a significant coherent nonlinear optical response. This is due to the fact that optical fields that are involved in a nonlinear optical process are all on resonance for frequencies across a very broad spectrum (from THz to visible). The nonlinear optical response of graphene is given by the surface conductivity, instead of the nonlinear optical susceptibility $\chi^{(n)}$ for bulk material. However, an effective $\chi^{(n)}$ can be deduced from the surface conductivity by treating graphene as a thin layer of bulk material with a thickness of 0.33 nm [107, 108]. In this chapter, we focus on the ubiquitous four wave mixing process (FWM) in graphene

in the near infrared spectrum. In a conventional CARS-type FWM process [67, 107, 109], two colors (pump at wavelength λ_P and Stokes at wavelength λ_S) are employed for excitation, generating a new color at the anti-Stokes wavelength (λ_{AS}). In previous work [107], Hendry *et al*. have detected this anti-Stokes emission in single- and multi-layer graphene flakes deposited on a glass coverslip, producing high-sensitivity and high-resolution nonlinear optical images. The effective $\chi^{(3)}$ of graphene, according to their measurement (6 ps laser pulse at around 800 nm wavelength), is seven orders of magnitude higher than that of bulk silica. Because of the linear dispersion relation, this large nonlinear optical response should also be evident even when all photons involved in the FWM process (pump, probe, and anti-Stokes) are provided by a single broadband laser beam [67, 110], i.e. a near-degenerate case [111].

Two pulse-shaping methods that are similar to the hole-refilling technique [44, 59] can be used to detect the nonlinear signal in the near-degenerate FWM case. In one method, the anti-Stokes spectrum of the input pulse is eliminated with a static 4-f pulse shaper; therefore, the newly generated signal at the anti-Stokes wavelength can be detected against zero background [111]. In the other method, the anti-Stokes input spectral components are utilized as a local oscillator to interfere with the nonlinear signal and perform homodyne detection [46].

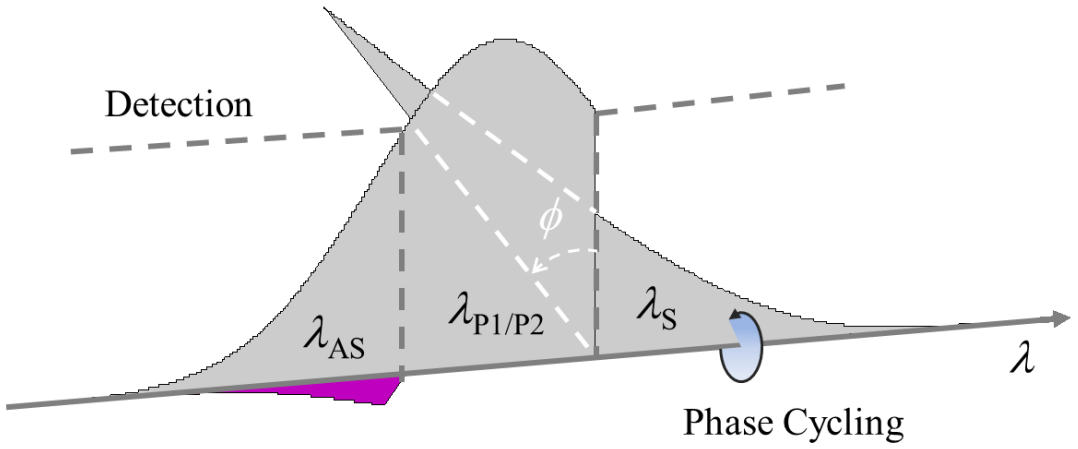

Figure 4.1: The pulse shape implemented for spectral-reshaping imaging. Dashed gray lines indicate the edges of the short- and long-pass filters placed symmetrically about the center wavelength. The phase ϕ of the Stokes component (λ_S) is cycled with frequency *f*. Nonlinear interactions take this modulated Stokes component, together with the pump components ($\lambda_{P1/P2}$), and generate a new field in the anti-Stokes spectrum (λ_{AS}) drawn in purple. This new component has a spectral phase that cycles with frequency *f* and interferes with the original static anti-Stokes components. The field generated by TPA is 180 degrees out of phase with λ_S, and the field generated by SPM is 90 degrees out of phase [44, 46]. Therefore, the homodyne detection of the intensity of the anti-Stokes spectrum can distinguish between TPA and SPM.

As illustrated in Figure 4.1, frequency shifting the Stokes component by a few MHz using a rapid pulse shaper (see Chapter 3) with an acousto-optic modulator (AOM) introduces a phase shift ϕ onto this spectral component of each laser pulse. This phase shift is then increased from pulse to pulse. Consequently, the cycled phase is transferred to the generated nonlinear signal in the anti-Stokes spectrum through the FWM process, which involves two pump photons (not necessarily degenerate) and one Stokes photon. The generated signal interferes with the original component at the anti-Stokes wavelength (acting as a phase reference for homodyne detection), thus producing an

intensity modulation on the output beam which can be measured by a lock-in amplifier (amplitude A, phase θ). A short-pass filter is inserted before the photodetector to reject all other frequency components of the output pulse. Compared to conventional CARS type of FWM, or previous near-degenerate FWM method, our technique provides additional phase information of the nonlinear interaction, amplifies the signal, and reduces sensitivity to scattering (as the reference field is part of the single excitation pulse).

To resolve the phase information in our nonlinear optical signal, we adjust the lock-in reference phase such that SPM processes give a phase of $\theta = 0$, and TPA processes give a phase of $\theta = \pi/2$. In general, the phase is related to the susceptibility components by $\tan\theta = \beta \mathrm{Im}[\chi^{(3)}_{gr}]/\mathrm{Re}[\chi^{(3)}_{gr}]$, where β is a constant that takes into account the relative detection sensitivity of TPA and SPM. That is, if we have a same magnitude of the real and imaginary parts of $\chi^{(3)}$, the ratio of the measured TPA signal to the SPM signal is β. The factor β depends on the specific pulse shape and detection setup (e.g. the position of the edge filters) and can be calibrated experimentally (for the current pulse shape β = 1.7, refer to Figure 2.7 in Chapter 2).

4.3. Measuring the complex $\chi^{(3)}$ of graphene and its saturation

4.3.1. Experimental setup and the expected signal using a simple analytical model

With the phase-cycling spectral reshaping technique, we are able to measure the complex form of the effective third-order nonlinear optical susceptibility of graphene,

$\chi^{(3)}_{gr}$. The geometry of our experimental setup is illustrated in Figure 4.2, where a graphene monolayer on a glass substrate is illuminated by a laser beam focused by a 20x 0.45 NA objective. The sample is translated through the focus and at each z position the lock-in signal is recorded. The input laser is linearly polarized along the x direction (in lab coordinates) and the detection is not polarization-sensitive. Due to the symmetry of graphene in the transverse plane, the signal should be independent of the excitation light polarization [112].

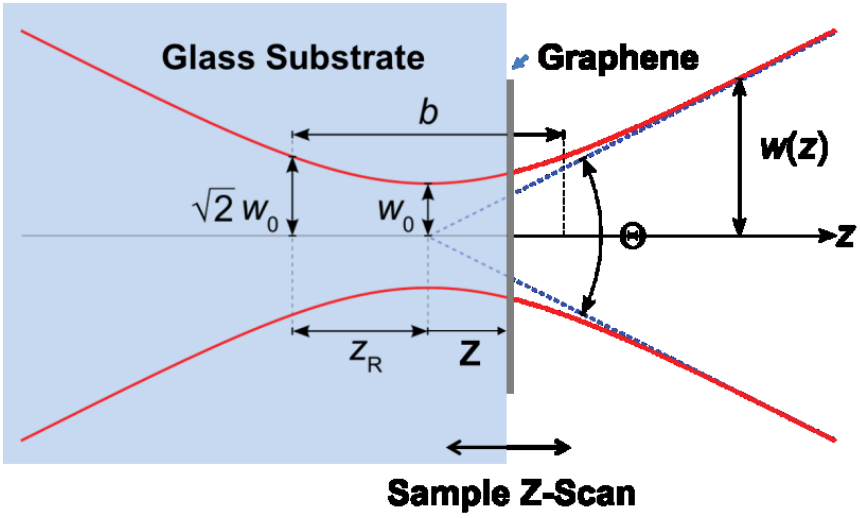

Figure 4.2: $\chi^{(3)}$ measurement on a monolayer of graphene. The sample is translated across the focus to produce a nonlinear signal as a function of axial position, from which we can extract $\chi^{(3)}_{gr}$. The focused beam is described by a Gaussian profile with a beam radius w_0 and a Rayleigh range z_R. These parameters are taken in air and the deflection at the interface is not shown (see text). The figure is adapted from Wikipedia (http://en.wikipedia.org/wiki/Gaussian_beam).

To extract the effective $\chi^{(3)}$ from a graphene sample, we derive a simple analytical model to calculate the expected nonlinear signal as a function of the axial position. Our

experiment is conducted with ultrafast laser pulses, where their temporal profile can be described by a Gaussian function

$$P(t) = P_0 \exp\left[-4 \ln 2 \left(\frac{t}{\tau_P} \right)^2 \right], \tag{4.1}$$

where τ_P is the full width at half-maximum (FWHM) pulse duration and P_0 is the peak power given by $P_0 = \varepsilon_P \sqrt{4 \ln 2 / \pi} \big/ \tau_P \approx 0.94 \varepsilon_P / \tau_P$, with ε_p denoting the pulse energy. For an average laser power of 1 mW, the energy carried by a single mode-locked laser pulse (FWHM 50 fs, 80 MHz repetition rate) is about 12.5 pJ.

With the geometry shown in Figure 4.2, the intensity profile of a focused laser beam can be treated as a Gaussian distribution:

$$I(z,r) = I_0 \frac{w_0^2}{w^2(z)} \exp\left(-\frac{2r^2}{w^2(z)} \right). \tag{4.2}$$

Here the beam radius w(z) (as a function of axial position z and the Rayleigh range z_R) is the position where the intensity drops to $1/e^2$ and is given by

$$w(z) = w_0 \sqrt{1 + \frac{z^2}{z_R^2}}, \; z_R = \frac{\pi w_0^2}{\lambda}. \tag{4.3}$$

The total power transmitted is then expressed as

$$P_0 = I_0 \frac{\pi}{2} w_0^2 = I_0 z_R \lambda / 2 . \tag{4.4}$$

Here w_0 is the beam waist at the focus in air. The refraction at the air-glass surface changes the focusing behavior, but the beam waist w_0 remains the same in glass. The total power is also conserved when transmitted from air into glass (if the 4% reflection is neglected). In our experiment, the distance is measured in air. The position in glass can be obtained by rescaling the length by the refractive index of the glass (n). For example, the Rayleigh range (z'_R), the distance from the interface to the focus (z') and the wavelength (λ') in glass are given by $z'_R = nz_R$, $z' = nz$, and $\lambda' = \lambda/n$ (in all these cases, the prime denotes parameters in glass). However, if the distance is normalized by the Rayleigh range, this change does not need to be explicit.

For a constant $\chi^{(3)}$ the signal measured by the spectral reshaping method is proportional to $\chi^{(3)}$ multiplied by the intensity squared [59]. For now, we assume that both graphene and glass have a constant $\chi^{(3)}$ across the spectrum and intensity range used in our experiment. The SPM signal from the graphene monolayer is expressed as a signal produced by a thin layer with an effective third-order nonlinear optical susceptibility $\chi^{(3)}_{gr}$ and an effective thickness d = 0.33 nm, the interlayer distance in graphite:

$$\begin{aligned} SPM_{gr}(z) &= \gamma_{SPM}\,\mathrm{Re}[\chi^{(3)}_{gr}]\int_0^\infty I^2(z,r)2\pi r dr\cdot d \\ &= \frac{\pi}{4} d I_0^2 w_0^2 \gamma_{SPM}\,\mathrm{Re}[\chi^{(3)}_{gr}]\frac{1}{1+z^2/z_R^2} \\ &= \gamma_{SPM} P_0^2 \frac{d}{z_R \lambda}\mathrm{Re}[\chi^{(3)}_{gr}]\frac{1}{1+z^2/z_R^2}. \end{aligned} \tag{4.5}$$

γ_{SPM} is the coefficient introduced in Chapter 2 to account for the sensitivity of our SPM measurement. Integration along the axial direction is not needed for graphene, because it is atomically thin. A similar derivation yields the expression for the TPA signal produced by the graphene monolayer:

$$TPA_{gr}(z) = \gamma_{TPA} P_0^2 \frac{d}{z_R \lambda} \mathrm{Im}[\chi_{gr}^{(3)}] \frac{1}{1 + z^2 / z_R^2}. \tag{4.6}$$

To calculate the SPM signal in glass, the integration over the axial direction needs to be evaluated, leading to

$$\begin{aligned} SPM_{gls}(z) &= \frac{\pi}{4} I_0^2 w_0^2 \gamma_{SPM} \,\mathrm{Re}[\chi_{gls}^{(3)}] \int_{-\infty}^{z'} \frac{1}{1 + z'^2 / z_R'^2} dz' \\ &= \frac{\pi}{4} I_0^2 w_0^2 \gamma_{SPM} z_R' \,\mathrm{Re}[\chi_{gls}^{(3)}] \left(\frac{1}{\pi} \arctan(\frac{z'}{z_R'}) + \frac{1}{2} \right). \\ &= \gamma_{SPM} P_0^2 \frac{n\pi}{\lambda} \mathrm{Re}[\chi_{gls}^{(3)}] \left(\frac{1}{\pi} \arctan(\frac{z}{z_R}) + \frac{1}{2} \right) \end{aligned} \tag{4.7}$$

The reflective index n is introduced here to account for the beam profile change when the Gaussian beam enters the glass. The total SPM signal includes the contribution from graphene, Eq. (4.5), and from glass, Eq. (4.7), which can be expressed as

$$\begin{aligned} SPM_{Total}(z) &= \gamma_{SPM} P_0^2 \frac{n\pi}{\lambda} \mathrm{Re}[\chi_{gls}^{(3)}] \left(\frac{1}{\pi} \arctan(\frac{z}{z_R}) + \frac{1}{2} + \frac{B}{1 + z^2 / z_R^2} \right) \\ &= A \left(\frac{1}{\pi} \arctan(\frac{z}{z_R}) + \frac{1}{2} + \frac{B}{1 + z^2 / z_R^2} \right) \end{aligned}. \tag{4.8}$$

The coefficient A and B are defined as

$$A = \gamma_{SPM} P_0^2 \frac{n\pi}{\lambda} \mathrm{Re}[\chi_{gls}^{(3)}],\ B = \frac{d}{nz_R\pi} \frac{\mathrm{Re}[\chi_{gr}^{(3)}]}{\mathrm{Re}[\chi_{gls}^{(3)}]}. \quad (4.9)$$

A is the maximum SPM signal generated in the glass substrate when the beam focus is embedded in glass. The ratio of the real part of $\chi^{(3)}_{gr}$ to that of $\chi^{(3)}_{gls}$ can be expressed as

$$R \equiv \frac{\mathrm{Re}[\chi_{gr}^{(3)}]}{\mathrm{Re}[\chi_{gls}^{(3)}]} = \frac{\pi B n z_R}{d}. \quad (4.10)$$

The TPA signal is produced only by graphene and can be expressed as

$$TPA_{Total}(z) = \frac{A \cdot C}{1 + z^2 / z_R^2}, C = \frac{d}{nz_R\pi} \frac{\gamma_{TPA}}{\gamma_{SPM}} \frac{\mathrm{Im}[\chi_{gr}^{(3)}]}{\mathrm{Re}[\chi_{gls}^{(3)}]}. \quad (4.11)$$

A, B, and C, will be used later as a model fitting parameter. With these coefficients, the ratio Γ of $\mathrm{Im}[\chi^{(3)}_{gr}]$ to $\mathrm{Re}[\chi^{(3)}_{gr}]$ is given by

$$\Gamma = \frac{\gamma_{SPM} C}{\gamma_{TPA} B} \equiv \frac{C}{\beta B}. \quad (4.12)$$

The β factor (1.7 for the pulse shape used in these measurements) has been defined previously to account for the different sensitivity of the SPM and the TPA measurements (refer to Figure 2.7 in Chapter 2).

4.3.2. Experimental results

The graphene sample used for the $\chi^{(3)}$ measurement was purchased from Graphene Supermarket (1ML-GL-1x1) , where a CVD-grown monolayer graphene is transferred onto a glass substrate (Eagle E301, Corning, a BSC type of glass) with

refractive index n=1.5 [113, 114]. The surface morphology of this graphene sample is investigated using the high-contrast SPM and TPA images shown in Figure 4.3 (taken with a 40x 0.75 NA objective). Because this CVD-grown graphene monolayer is fairly uniform across the whole illuminated region (up to few 100 μm), it serves as an ideal sample for $\chi^{(3)}$ measurements. However, we do observe that some regions of the sample have been scratched or crumpled during the transfer process; as a result, the effective number of layers at the edges of the graphene sheet is higher, leading to substantially higher nonlinear signals in both SPM and TPA channels. High-contrast imaging of monolayer graphene on various substrates, by itself, is useful for many solid-state applications of graphene. For example, our method could be employed to check the uniformity of the transferred monolayer graphene onto polymer based substrates used to manufacture mechanically flexible graphene-based biosensors, [115, 116].

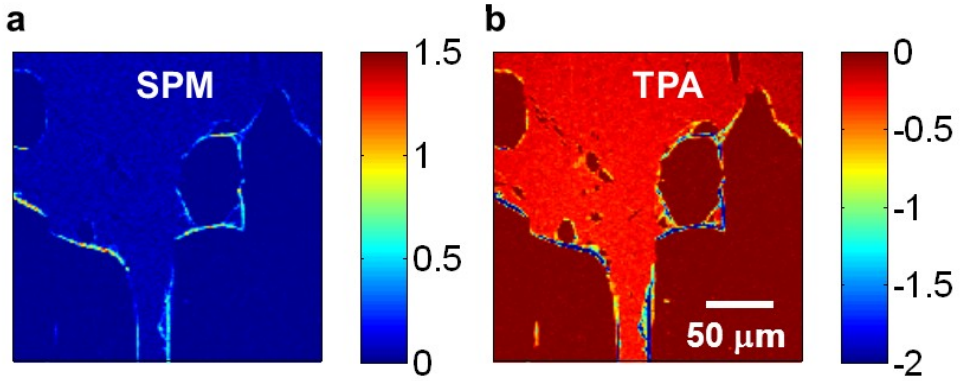

Figure 4.3: SPM and TPA images of the monolayer graphene on glass. These images are taken with a 40x 0.75 NA objective, and 1 mW input power. High intensity along the perimeter is due to the rolling up of the edges.

To quantitatively assess $\chi^{(3)}_{gr}$, a different objective (20x 0.45 NA) is used to ensure better characterization over a larger area and to reduce the risk of damaging our sample. For this experiment, we use an 80 MHz mode-locked laser with the central wavelength at 805 nm (FWHM = 25 nm). A pulse duration τ_p of 50±5 fs is measured by a second-harmonic generation FROG. Figure 4.4 shows the measured nonlinear signals as functions of the sample position, or z-scan traces. Note that both TPA and SPM show prominent features and clear power dependence, which may or may not be reproduced by the simple analytical model described above.

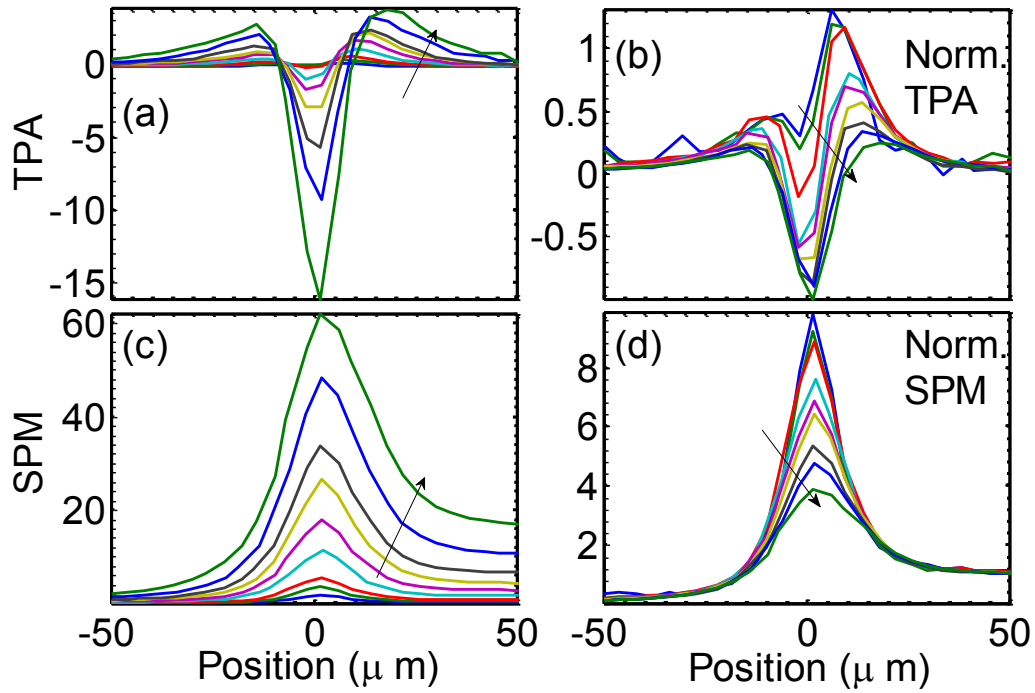

Figure 4.4: Nonlinear signals in graphene as functions of the z position with increasing laser power. The left column (a, c) plots the original TPA and SPM z-scan traces, and the right column (b, d) shows normalized z-scan traces (normalized by the SPM signal in glass, which shows the expected quadratic dependence on power, as shown in Figure 4.6). The arrows indicate increasing laser powers (0.37, 0.56, 0.74, 1.11, 1.48, 1.88, 2.31, 2.91, and 3.65 mW).

The TPA z-scan traces shown in Figure 4.4 (a), particularly the dip at the focus, is unexpected according to our simple analytical model, which predicts a positive Lorentzian peak (see Eq. (4.11)). We will show later that this dip structure is not an artifact. It reflects the very strong power dependence of the TPA coefficient, which actually changes sign near the power we apply; however, other nonlinear optical processes could also contribute to the observed trace.

The SPM z-scan trace has a functional dependence that is in good agreement with the derived analytical model (Eq. (4.8)). Figure 4.5 shows the experimental results (using 0.56 mW power) along with a fit to Eq. (4.8). Here the data is normalized by the maximum signal in glass (the value at the right end in Figure 4.4 (c)), which exhibits a perfect quadratic dependence on laser power as demonstrated in Figure 4.6. To facilitate the fitting, we first deduced the Rayleigh range (z_R = 4.9±0.1 μm) by fitting a SPM z-scan trace of a clean glass coverslip with Eq. (4.7), as shown in the inset in Figure 4.5. With this Rayleigh range and by fitting a z-scan trace of the total SPM signal with Eq. (4.8), we obtain a coefficient B of 11.5 and a corresponding ratio R of $8.0*10^5$. According to Eq. (4.10), this ratio R can also be calculated by dividing the area between the blue dotted line (which is the normalized signal from the glass substrate) and the data curve by d/n.

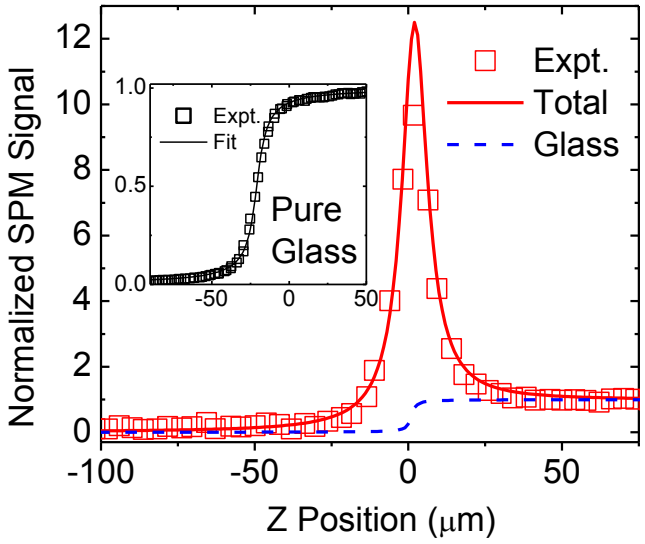

Figure 4.5: Experimental data compared with the analytical-model fit assuming a constant $\chi^{(3)}_{gr}$. The SPM signal is normalized by the maximum signal from glass. The blue dashed line is the calculated SPM signal from the glass substrate. The inset is a fit to the SPM signal from pure glass, which yields a Rayleigh range of 4.9 μm in air. The laser power is 0.56 mW. The mismatch in peak value is due to the saturation effect.

With the ratio R and by using Eq. (4.10), we obtain the real part $\chi^{(3)}$ in graphene $Re[\chi^{(3)}_{gr}] = 4.0*10^{-16}$ m^2/V^2. Because the absolute $\chi^{(3)}$ value of our glass substrate is not available, we use a value from a similar type of glass (BSC) which has of $\chi^{(3)}_{gls} = 5.0*10^{-22}$ m^2/V^2 [70, 117]. Depending on its ingredients and the specific manufacturing process, our glass substrate may have a value that deviates from the cited one. This is one of the major contributors to the uncertainty of our measurement and a 20% error would be a reasonable estimate [118]. This experimentally derived result is in relatively good agreement with the value obtained by a theoretical model ($4.4*10^{-16}$ m^2/V^2, shown later in Figure 4.7). This model was developed by our collaborator Dr. Zheshen Zhang from MIT and it has been published in Ref. [119]. We will introduce the model in the next

subsection and we will discuss the theoretical data in more detail. Note that this value is about 5 times smaller than what was reported by Hendry *et al.* in Ref. [107] ($2.1*10^{-15}$ m^2/V^2 or $1.5*10^{-7}$ esu, 1 esu = $1.4*10^{-8}$ m^2/V^2), where the amplitude of $\chi^{(3)}_{gr}$ is measured by a FWM experiment with two 6 ps laser pulses at 969 nm and 1179 nm. This discrepancy is likely due to the fact that our experiments used much shorter pulses (50 fs vs. 6 ps). The carrier dynamics and the induced optical response could substantially differ in these two regimes.

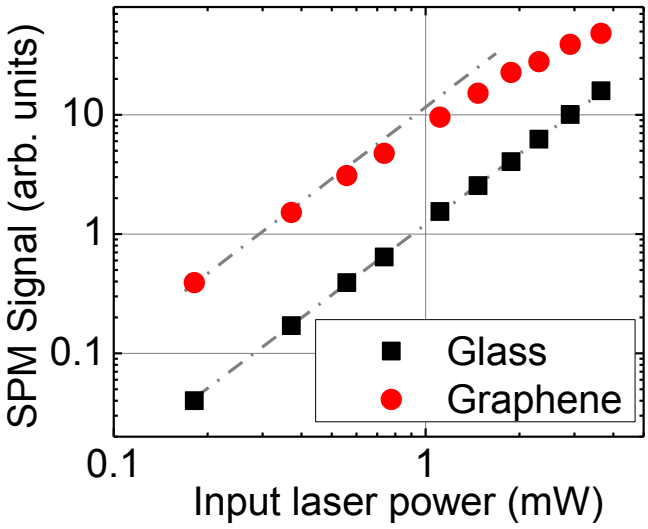

Figure 4.6: Power dependence of the SPM signal of graphene. Grey dashed lines represent the quadratic dependence. The signal in glass (value at the right end of the z-scan traces in Figure 4.4 (c)) shows nearly perfect quadratic power dependence, while the signal in graphene (peak value of curves shown in Figure 4.4 (c) subtracted by half of the glass SPM signal) deviates from the quadratic dependence, particularly at high powers.

In Figure 4.5, the fit to our SPM z-scan trace by using the analytical model is reasonably good except for the peak value at the focus. We suspect that this deviation is due to a saturation effect in the third-order nonlinear optical response at high intensities

[119]. This saturation effect is readily observed in Figure 4.4 (d), where a series of normalized SPM z-scan traces taken with varying input power are plotted in a group. Without saturation (i.e. constant $\chi^{(3)}$), all curves should lay on top of each other. However, our experimental results exhibit an increasing fall-off of the peak as the laser power increases. The saturation effect is also revealed by the power dependence of the SPM signal shown in Figure 4.6. While the SPM signal in the glass substrate clearly shows a quadratic dependence with power, the SPM signal in graphene deviates from the predicted quadratic dependence, particularly at high powers, indicating a decreasing $\mathrm{Re}[\chi^{(3)}_{gr}]$.

4.3.3. Theoretical calculation of $\chi^{(3)}$ in graphene

The optical response of the 2D electron system in graphene has been examined in several theoretical studies. Perturbation theory has been employed to calculate the effective $\chi^{(3)}$ but has failed to predict the saturation effect [107]. Our collaborator Dr. Zheshen Zhang has developed a comprehensive full-band quantum-dynamic model to study the saturation and FWM process in graphene [119]. In his work, Zhang numerically solves the quantum dynamics of a density-matrix with strong continuous-wave excitation. In this subsection, we introduce the density-matrix model developed in Ref. [119] and the comparison between the obtained numerical results and our experimental data will be discussed later in subsection 4.3.4.

By using a tight-binding model with the nearest-neighbor interaction approximation, the Hamiltonian of an electron with momentum **p** in graphene can be expressed as

$$H_0 = \begin{pmatrix} 0 & h_{\mathrm{p}} \\ h_{\mathrm{p}}^* & 0 \end{pmatrix},\ h_{\mathrm{p}} = -\varsigma\left[\exp\left(i\frac{ap_y}{\sqrt{3}\hbar}\right) + 2\cos\left(\frac{ak_x}{2}\right)\exp\left(-i\frac{ap_y}{\sqrt{3}\hbar}\right)\right], \tag{4.13}$$

where ζ = 2.7 eV is the hopping energy for electrons in graphene and a = 0.33 nm is the lattice constant of graphene. With a given **p**, the two energy eigenstates $|C_{\mathbf{p}}\rangle$ and $|V_{\mathbf{p}}\rangle$ with eigenvalues $\pm|h_{\mathbf{p}}|$ for this Hamiltonian correspond to the paired conductive-band and valence-band states. In a conventional FWM experiment, light with two frequencies (pump, ω_p and stokes, ω_s) are applied with polarization along the x axis of the lattice, and therefore the total external field can be written as a vector potential

$$\widetilde{A}(t) = A_p \exp(-i\omega_p t) + A_s \exp(-i\omega_s t) + c.c.. \tag{4.14}$$

When exposed to this electric field, the new Hamiltonian of the electron can be obtained by simply substituting **p** with **p**+e $\widetilde{A}(t)$, which can be expanded as a sum of two parts

$$H = H_0 + V(t),\ V(t) = e\nabla_{\mathrm{p}} H_0 \widetilde{A}(t) \tag{4.15}$$

Once electrons are excited from the valence band to the conduction band, they go through several relaxation processes at different time scales: an ultrafast quantum decoherence process, a fast electron-electron scattering relaxation followed by a slower electron-phonon relaxation [119, 120]. The quantum-dynamics of the system thus can be

described by two phenomenological decay constants: τ_1 for carrier relaxation and τ_2 for the quantum decoherence. τ_2 could be determined by measuring the imaginary part of the linear conductivity and usually takes a value of about 1 fs [119]. τ_1 can be measured by pump-probe spectroscopy. The measurement typically ranges from 10 fs to 100 fs, depending on the specific underlying relaxation mechanisms [119, 120]. With these two time constants, the dynamics of the density matrix can be expressed as

$$\begin{cases} \dot{\rho} = -(\rho - \rho^{eq})/\tau_1 + \dfrac{2ie}{\hbar}\sum_j \widetilde{A}_j(t)\, V_{VC}(\rho_{VC} + \rho_{CV}) \\ \dot{\rho}_{VC} = (i\omega_{CV} - 1/\tau_2)\rho_{VC} - \dfrac{ie}{\hbar}\sum_j \widetilde{A}_j(t)\,(2V_{VV}\rho_{VC} + V_{VC}\rho) \\ \dot{\rho}_{CV} = (-i\omega_{CV} - 1/\tau_2)\rho_{CV} - \dfrac{ie}{\hbar}\sum_j \widetilde{A}_j(t)\,(-2V_{VV}\rho_{CV} + V_{VC}\rho) \end{cases} . \tag{4.16}$$

Here the density matrix elements ρ_{lq} and the transition elements V_{lq} are defined as

$$\rho = \rho_{CC} - \rho_{VV},\ \langle l|V(t)|q\rangle = e\sum_j \widetilde{A}_j(t)V_{lq},\ l,q \in \{V,C\}. \tag{4.17}$$

Here ρ is the population inversion, ρ_{VC} is the quantum coherence, ρ^{eq} is the population inversion in thermal equilibrium, and ω_{CV} is the band gap frequency. Note that V_{CC}, V_{VV} and V_{CV} are transition elements. This approach is valid when the pulse duration τ_P is longer than τ_1 and τ_2, when the chemical potential is close to zero and when $\hbar\omega_{p,s}$ is much larger than kT. These density matrix elements are made up of components at frequencies ($m\omega_p$+$n\omega_s$)

$$\rho(t) = \sum_{m,n} \rho^{(m,n)}(t) \exp[-i(m\omega_p + n\omega_s)t] + c.c.,\ \ \rho \in \{\rho, \rho_{VC}, \rho_{CV}\}. \tag{4.18}$$

Under a steady state approximation, these Fourier components of the density matrix elements do not change with time. Together with Eq. (4.16), the density matrix of a single electron with momentum **p** can be obtained.

We calculate the expected velocity of an electron along the x direction as

$$\langle v_x \rangle = \mathrm{Tr}(v_x \rho) \equiv \mathrm{Tr}(\partial H / \partial p_x \rho). \tag{4.19}$$

The surface current density is then obtained by evaluating the integral of $e\langle v_x \rangle$ over the whole Brillouin zone

$$\tilde{J}(t) = \frac{1}{4\pi} \int_{BZ} -e\langle v_x \rangle \mathrm{d}k_x \mathrm{d}k_y = \sum_{m,n} J^{(m,n)} \exp[-i(m\omega_p + n\omega_s)t] + c.c.. \tag{4.20}$$

The induced higher order surface currents $J^{(m,n)}$ at multiple frequencies $m\omega_p + n\omega_s$ are the origin of the nonlinear optical response in graphene. For example, the current at the so-called anti-Stokes frequency $2\omega_p - \omega_s$ may radiate new light at this frequency. The optical response of graphene thus can be described by the surface conductivity σ as a function of frequency (analogous to the nonlinear optical susceptibility in bulk material). The FWM conductivity σ_{FWM} at $\omega_{as} = 2\omega_p - \omega_s$ can be calculated by

$$\sigma_{FWM} = 2 \times \frac{8}{3} \times J^{(2,-1)} \Big/ E_p^2 E_s^*. \tag{4.21}$$

Here the factor of 2 accounts for the two electron spin states. We define the complex effective third-order nonlinear optical susceptibility of graphene as

$$\chi_{gr}^{(3)} = \sigma_{FWM} / \varepsilon_0 \, \omega_{as} d \, , \tag{4.22}$$

where d = 0.33 nm is the effective thickness of a single graphene layer.

4.3.4. Comparison between experiment and theory

One of the obvious features of the experimental data is the saturation in the third-order nonlinear optical response of graphene with laser pulse energies of the order of 10 pJ, which seems astonishing at first glance. However it is interesting to count photons in this problem. With a 1 mW average input power, each mode-locked laser pulse in our experiment carries about $5*10^7$ photons during the 50 fs pulse duration, which goes through a 4 μm^2 focal area and leads to a photon number density of $1.25*10^{15}$ photons per cm^2. Graphene is a single layer of carbon atoms with a number density of $3.8*10^{15}$ atoms per cm^2. So with our pulses, we approach one photon per atom (or per valence electron), which certainly suggests that saturation effects are plausible.

Then the critical parameter is the ratio of the pulse length to the relaxation times. The theoretical calculation is performed with a pump wavelength at 805 nm and a Stokes wavelength at 810 nm, in accordance with the wavelength used in our experiment. The calculated $\chi^{(3)}_{gr}$ as functions of intensity for three sets of (τ_1, τ_2) are plotted in Figure 4.7. One particular set of parameters (τ_1 = 30 fs, τ_2 = 1 fs, the solid line) is chosen to match a saturation threshold intensity of 11 GW/cm^2, which is obtained by fitting our

experimental data with a classical saturation model (see Figure 4.10). At low intensities, the unsaturated real part of $\chi^{(3)}_{gr}$ is $4.4*10^{-16}$ m^2/V^2 and the corresponding imaginary part is $0.9*10^{-16}$ m^2/V^2. As mentioned above, this is in good agreement with our result, obtained by fitting our experimental data with the simple analytical model.

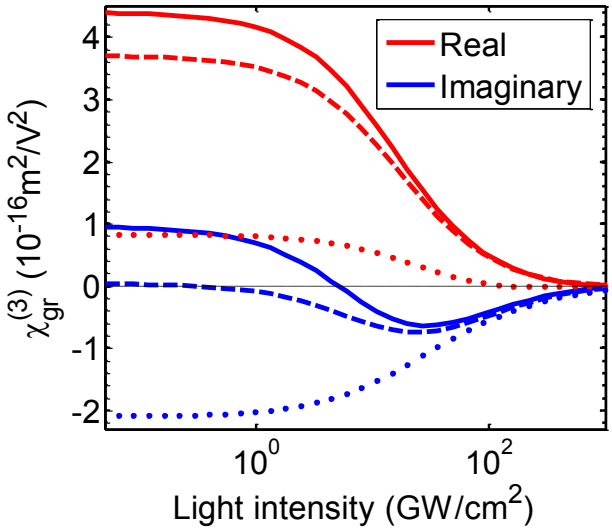

Figure 4.7: Real and imaginary parts of the effective $\chi^{(3)}$ of graphene as a function of light intensity as predicted by the theoretical model in Ref. [119]. The pump and Stokes wavelengths are 805 nm and 810 nm. Solid, dashed and dotted lines are for (τ_1 = 30 fs, τ_2 = 1 fs), (τ_1 = 20 fs, τ_2 = 1 fs) and (τ_1 = 10 fs, τ_2 = 1 fs).

With τ_1 = 30 fs, our numerical calculation predicts a strong saturation behavior starting at a few GW/cm^2 in both the real and imaginary parts of $\chi^{(3)}_{gr}$. The imaginary part of $\chi^{(3)}_{gr}$ exhibits an unexpected sign change, which might lead to the previously observed sign change in our TPA signal (the dip feature in the z-scan traces). However, the saturation behavior varies significantly as τ_1 changes, and the sign change only appears for certain choices of τ_1 for a given τ_2. For example, as τ_1 increases from 10 fs to 30 fs, the

real part of the unsaturated $\chi^{(3)}$ increases by three times. More significantly, the imaginary part shifts from a negative to a positive value, introducing a cross-over point during the saturation regime. With the theoretical prediction shown in Figure 4.7 and given the fact that we indeed observe a sign change in our TPA measurement, the relaxation time τ_1 in graphene should be bigger than 20 fs. This is entirely consistent with an intuitive interpretation: if the relaxation time were much greater than the pulse length, a flux on the order of one photon per molecule at the beam focus (coupled with the known linear absorption of 2.3% for single layer graphene) implies a substantial fractional electronic excitation. In contrast, silica or glass has very little absorption, the relaxation times are much shorter, and the atoms are distributed over the laser beam Rayleigh range and beyond-hence the threshold for seeing significant changes in the nonlinear coefficients is much higher.

To perform a quantitative comparison between the saturation behavior observed in our measurement and the theoretical prediction, we need to calculate the expected lock-in signal with consideration of the temporal profile of the laser pulses at high input power. This is because laser pulses are modified in our spectral reshaping measurement and the saturation behavior of $\chi^{(3)}$ has a different impact on different pulse shapes, which changes the expected measurement of SPM and TPA at high intensities. In our experiment, the phase of the Stokes spectrum is cycled and the temporal profile of intensity varies from pulse to pulse. As a result, each pulse may experience a distinct $\chi^{(3)}_{gr}$, particularly when the intensity is in the saturation regime. Figure 4.8 (a) plots a series of

temporal intensity profiles for a set of eight pulses. The spectrum of these pulses is shown in Figure 4.1, but with a different phase shift in the Stokes spectrum. As the phase shift increases (with steps of $\pi/4$), the pulse shape in the time domain also displays a periodic modulation, and so does the peak intensity. For a π phase shift, a flat-top pulse shape is formed and the peak intensity drops to half.

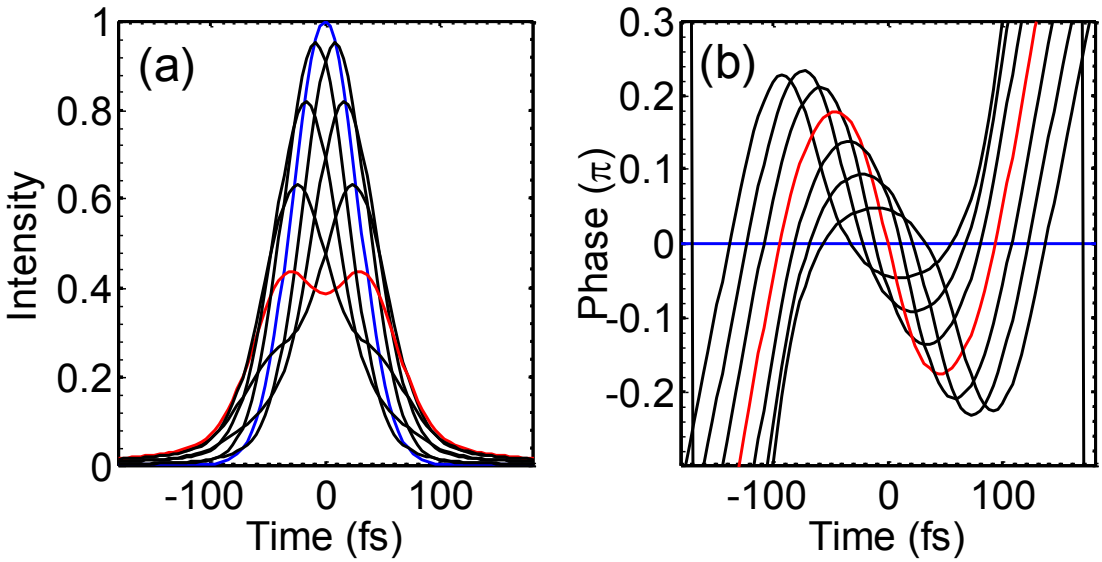

Figure 4.8: Temporal profiles of pulse intensities (left) and the corresponding phase (right) for phase-cycled laser pulses, with their spectrum shown in Figure 4.1. The blue curves are for a zero phase shift in the Stokes spectrum and the red curves are for a π phase shift. The phase step for each curve is $\pi/4$. Because of this large intensity modulation, the saturation behavior has different impacts on pulses with different phase shifts.

The impact of the saturation effect on the lock-in signal can be quantified by calculating an intensity-dependent γ_{SPM} and γ_{TPA}, which involves solving the nonlinear propagation equation described in Chapter 2 with a time-dependent $\chi^{(3)}$, i.e. $\chi^{(3)}(t) = \chi^{(3)}(I(t))$, and with the assumption of an instantaneous nonlinear response. Figure 4.9

shows the calculated lock-in signal (normalized by the intensity squared) as a function of the peak intensity of a Gaussian laser pulse. For comparison, we also plot the signal predicted by a classic saturation model $S/S_0 = 1/(1+I/I_{th})$, where S_0 is the unsaturated signal obtained with the unsaturated $\chi^{(3)}$ and I_{th} is the threshold. While the classical model with a threshold of 11 GW/cm^2 fits the calculated SPM signal reasonably well, the saturation behavior of the TPA signal vastly differs from the classic saturation model. The calculated lock-in signals also exhibit a saturation behavior distinct from the genuine saturation behavior of the theoretically predicted $\chi^{(3)}$, particularly for the TPA signal. In general, the spectral reshaping measurement tends to exaggerate the saturation signature. For example, both SPM and TPA signals display a sharper drop. The TPA signal starts to flip sign at a lower intensity as compared to $\mathrm{Im}[\chi^{(3)}_{gr}]$ and the valley is also relatively deeper. Again, the sign change in TPA very likely contributes to the unexpected signal in Figure 4.4 (a). The saturation line shape is thus crucial for future investigations on the underlying saturation mechanism.

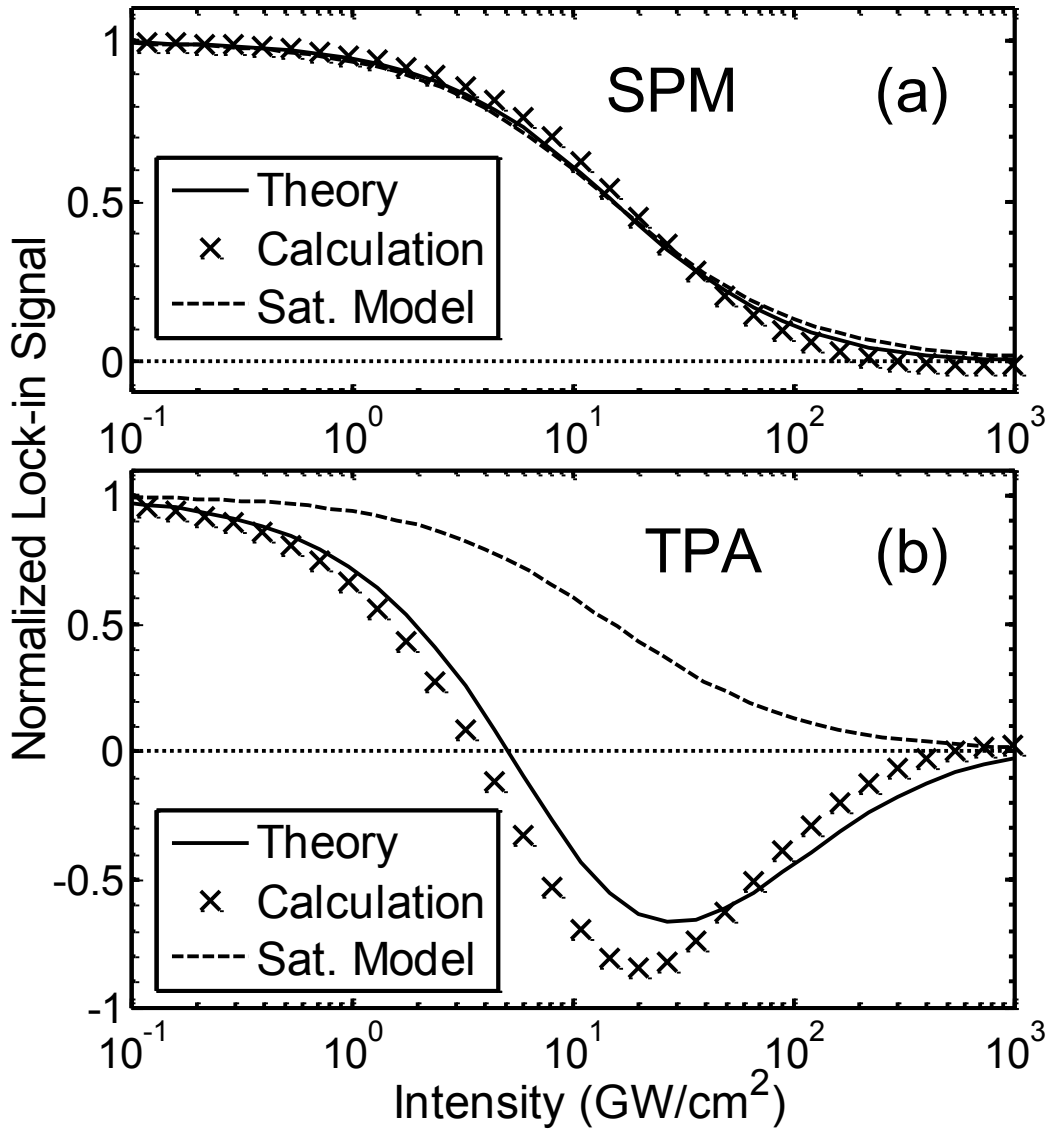

Figure 4.9: Comparison of theoretically generated $\chi^{(3)}$ values (solid lines, identical to τ_1=30 fs curve in Figure 4.7 where both channels are normalized to one) to the lock-in signals from our detection method (crosses). Part (a) shows the real part of $\chi^{(3)}$ (self-phase modulation); part (b) shows the imaginary part (two-photon absorption). The dashed curves are signals fit by the classic saturation model with a threshold of 11 GW/cm^2. Note the very strong deviations in part (b) from classical saturation behavior (including a sign change) which likely contributes to the unexpected experimental behavior in Figure 4.4.

With the calculated lock-in signal as a function of intensity, the expected SPM and TPA signal for a particular laser power can be obtained by integrating the signal over the whole transverse plane at a given z position. In Figure 4.10 we compare the calculated SPM signal at the focus (z=0, τ_1 = 30 fs and τ_2 = 1 fs) with our measurement (obtained from Figure 4.4 (d)). With a $\chi^{(3)}_{gls}$ of 5.8*10^{-22} m^{2}V^2, the calculated SPM signal shows good agreement with our measurement. The uncertainty in $\chi^{(3)}$ of our glass substrate changes the signal strength (for example, in an extreme case a $\chi^{(3)}_{gls}$ of 2.0*10^{-22} m^{2}V^2 may scale the normalized signal up by 3 times), however the saturation behavior is well captured. There are two other major factors that contribute to the uncertainty of our measurement: the error in the pulse duration and the error in laser power. The pulse duration τ_P was measured by FROG [121] and had an error of about 10% (50±5 fs), which leads to about 10% uncertainty in peak intensity calculations. This may slightly shift the calculated curve along the power axis. On the other hand, the error in our laser power measurement (10%) could also slightly move the experimental data points along the power axis. The uncertainty in the Rayleigh range (0.1 μm) and that in the z position measurement (the resolution of the vertical translation stage is 0.1 μm) contribute very little to the uncertainty in the peak value (less than 1%). All these effects are much less significant compared to the uncertainty in parameters of the glass, which can be eliminated by future measurements on the specific glass substrate used.

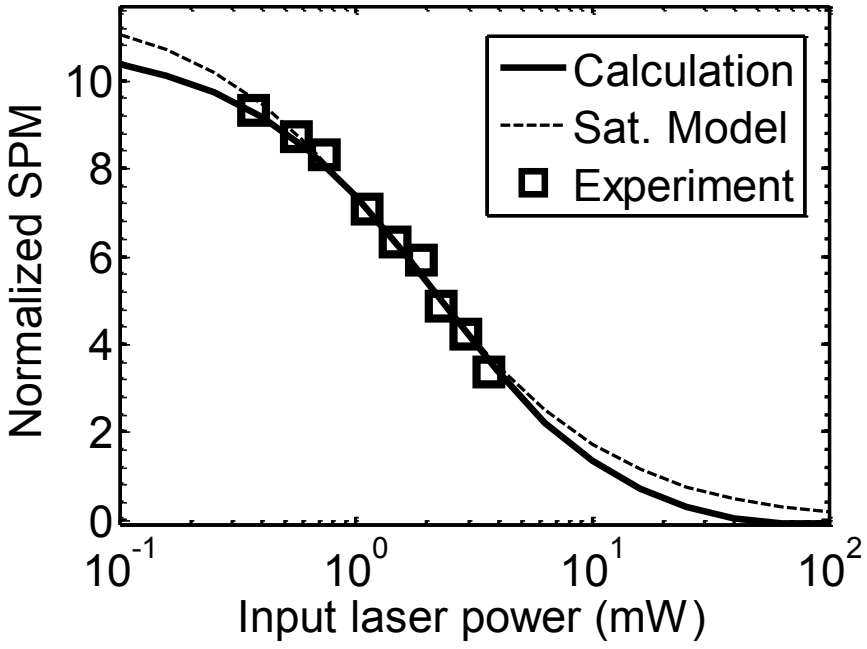

Figure 4.10: Comparison of theoretically-calculated SPM signals with experimental data. The lines are expected signal calculated with a $\chi^{(3)}_{gls}$ =5.8*10^{-22} m^2/V^2. The experimental data is obtained from Figure 4.4 (d). The dashed fit curve is calculated with a classical saturation model with a threshold of 1.7 mW corresponding to a threshold intensity of 11 GW/cm^2. For the theoretical calculation, τ_1 = 30 fs and τ_2 = 1 fs are chosen to match this saturation threshold.

In Figure 4.11, we compare the theoretically calculated z-scan traces with the experimental data. The $\chi^{(3)}_{gr}$ used for this calculation is obtained with τ_1 = 30 fs and τ_2 = 1fs. The fitting parameter coefficient B for the SPM z-scan trace is taken as 11.5 and the corresponding coefficient C = 4.0 for TPA z-scan trace is obtained with β = 1.7 and the ratio of the real part to the imaginary part of the calculated $\chi^{(3)}_{gr}$, see Eq. (4.11) and Eq. (4.12). A relatively good agreement between experimental data and the theoretical predication is demonstrated. Particularly the abnormal dip structure in the TPA z-scan trace is qualitatively reproduced when the input laser power is large.

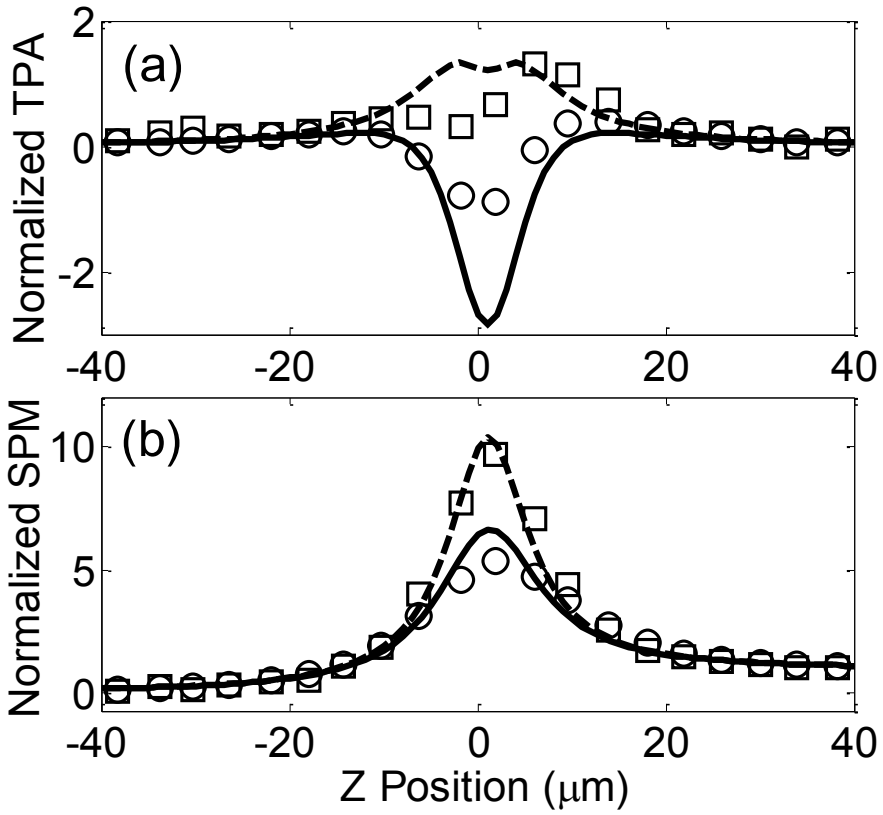

Figure 4.11: Comparison of the theoretically-calculated z-scan traces with the experimental data for TPA (a) and SPM signals (b). The laser power is 2.31 mW (solid line) and 0.37 mW (dashed line). Theoretical calculations use the following parameters: τ_1 = 30 fs, τ_2 = 1 fs, and β = 1.7.

The remaining disagreement implies that several other nonlinear optical processes may also contribute to signals in the TPA channel. One possible contributing factor could be higher-order nonlinearities of graphene (e.g. $\chi^{(5)}$ effects), which could induce saturation in the TPA signal [119]; however, this is unlikely to be the dominant effect, as Figure 4.4b shows that the TPA curves seem to be converging to a shape proportional to intensity squared. Other factors could be second-harmonic generation (SHG) in graphene itself [122, 123] , or surface second-harmonic generation (SSHG) [124,

125] and third-harmonic generation (THG) [38] at the air-graphene-glass interface. Like TPA, these are also loss processes and generate positive signals. Particularly, the asymmetric contribution of THG from glass and air interface (caused by aberrations of the Gaussian beam as it crosses from air into glass [38]) might lead to the asymmetric feature observed in the TPA z-scan traces – in Figure 4.4 (a) the glass side shows a higher signal than the air side. Finally, the broadband luminescence induced by the laser-created electron-hole plasma might produce some negative signal in the TPA channel [112]. This incoherent emission process exhibits a quadratic dependence on light intensity, which could lead to a negative peak given a different saturation behavior [112]. Note that graphene has a substantial linear absorption (a loss of 2.3% photons in the unsaturation regime) and thus a negative two-photon-absorption signal (a gain of $1.4*10^{-3}$ % photons with 3.7 mW input power) does not violate energy conservation. Further, this nonlinear emission is much smaller than the linear absorption.

More experimental and theoretical investigation is needed to fully understand the lineshape of the TPA signal. For example, one can isolate a pure nonlinear luminescence signal by rejecting the entire input laser spectrum with filters on the detection side, or a polarization dependent measurement can be employed to study the symmetry of SHG, SSHG and THG from the sample. We expect that a quantitative fit can be achieved by considering the potential contribution from other possible nonlinear processes discussed above, such as the SHG and the plasma-induced luminescence in graphene, as well as the THG and SSHG at the air-graphene-glass interface. Although the

complexity of the TPA z-scan traces prevents us from getting an accurate estimation of the imaginary part of $\chi^{(3)}_{gr}$ for now, our TPA measurement could potentially reveal a variety of interesting nonlinear optical phenomena of the air-graphene-glass interface. The understanding of these nonlinear processes is crucial for graphene application based on its nonlinear optical properties in electronics or optoelectronics [106, 126-128].

4.4. Layer counting in few-layer graphene flakes

The high contrast SPM/TPA images of graphene enables us to clearly quantify the number of layers in the various graphene flakes. To demonstrate this, we perform SPM and TPA imaging on mechanically exfoliated graphene flakes deposited on a glass coverslip. The results are presented in Figure 4.12, where regions displaying signals at discrete levels correspond to graphene flakes with different numbers of layers. As shown in the middle panel of Figure 4.12, similar patterns can also be seen in the bright-field image but with much lower dynamic range. To get the actual number of layers for each region, a correct scale (or unit) is required. We identified that the region labeled No. 1 in Figure 4.12 (b) produces the minimum nonlinear signal among all regions in the sample. It also serves as a building block for signals from a few other regions. We suspect that this is a single-layer flake and tested this assumption by analyzing region No. 1 with Raman spectroscopy. We plotted the corresponding Raman spectrum in Figure 4.13, where the 2D peak at 2645 cm^{-1} is higher (almost twice as large as) than the G peak at 1580 cm^{-1}, indicating that region No. 1 is indeed a single-layer graphene flake [129, 130].

By calibrating the image to the nonlinear signal of this single-layer region, the number of layers for the entire image can be determined. For graphene with only a few layers (less than 6) a linear dependence of the signal on the number of layers is a reasonable approximation. For more layers, however, a more sophisticated model is required, which will be discussed later.

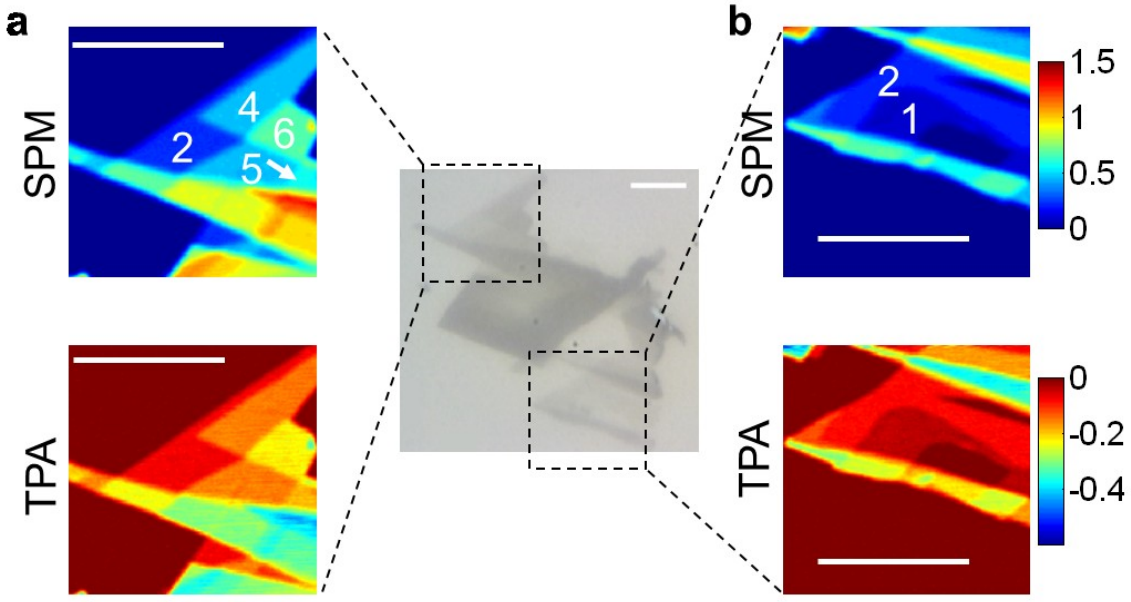

Figure 4.12: Bright field image (grayscale, center) and nonlinear optical imaging of mechanically exfoliated graphene flakes (color, sides). The regions of the nonlinear optical images are indicated by dashed boxes in the bright field images. The input laser power is 0.5 mW. For some regions, the number of layers is labeled with numbers. Acquisition time is 1.6 s per frame, and the images are averaged over 8 frames. Scale bars are 20 μm.

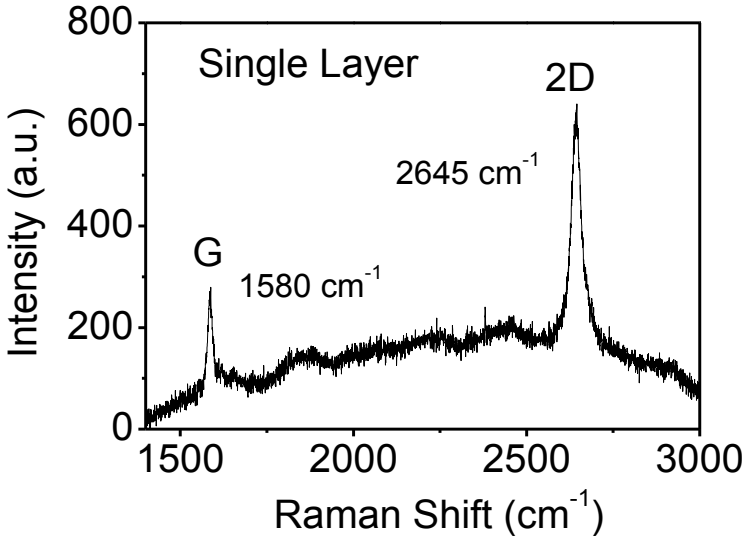

Figure 4.13: Raman spectrum of the graphene sample from region No. 1 in Figure 4.12 (b). The fact that the 2D peak is larger than the G peak confirms that a single-layer graphene is measured.

To provide more insight into the nonlinear signals and their dependence on the number of layers, we compare the nonlinear image with the co-registered transmission image. Our few-layer graphene samples have little scattering, and thus, we are able to obtain clean transmission images by averaging over a large number of frames (and normalizing by the transmission image taken from a blank area). In Figure 4.14 (a), we plotted a high resolution transmission image (1-T) of the few-layered graphene sample. The contrast in the transmission image is noticeably weaker than the contrast in the nonlinear image, as compared to the SPM image of the same sample in Figure 4.14 (b). We observe a strong correlation between linear absorption and nonlinear signal through a 2D histogram in Figure 4.14 (c). This 2D histogram plots co-registered pixels in the transmission and SPM images onto a 2D map, from which we are able to identify each

graphene flake in an intuitive, yet a quantitative manner. Pixels from the same region cluster together and form an island in the 2D map, and the color of these islands denotes the density of their population (or the area of the region). By selectively highlighting those pixels in individual islands (circles in Figure 4.14 (c)) in the original absorption and SPM images, we can easily visualize regions with a particular layer number of graphene flakes (colored areas in Figure 4.14 (a) and (b)). The tails attached to each island partially reveals its local environments: for example yellow colored regions form an island that has two additional outreaching tails (excluding the two major lines), indicating that it is connected to an open area and regions with even more layers. The island can also split to sub islands, due to small variations in the laser intensity when scanning, and because the nonlinear SPM signal is more sensitive to intensity. This phenomenon is more significant for regions with a large number of layers (see also regions No. 13a and 13b in Figure 4.14).

To make a fair comparison between the linear and nonlinear imaging techniques, we convert both signals into the equivalent number of layers based on their characteristic dependence on layer number. The expected transmittance is $T=1/(1+NS)^2$ for graphene flakes with N layers[99, 131]. For the intensity used here ($I = 10\ GW/cm^2$), saturation in absorption is observed [132], and we include a saturation factor η in the definition of $S=\eta\pi\alpha/2$, where α is the fine structure constant. In principle, η can be theoretically calculated using the method described in section 4.3.3. As described in [131], for a third-order process, a polarization field is generated that scales as

$E^{(3)}=NS/(1+NS)^4$. Because we measure the interference between the linearly transmitted phase reference and the generated anti-Stokes component, we expect our signal to scale as $NS/(1+NS)^5$.

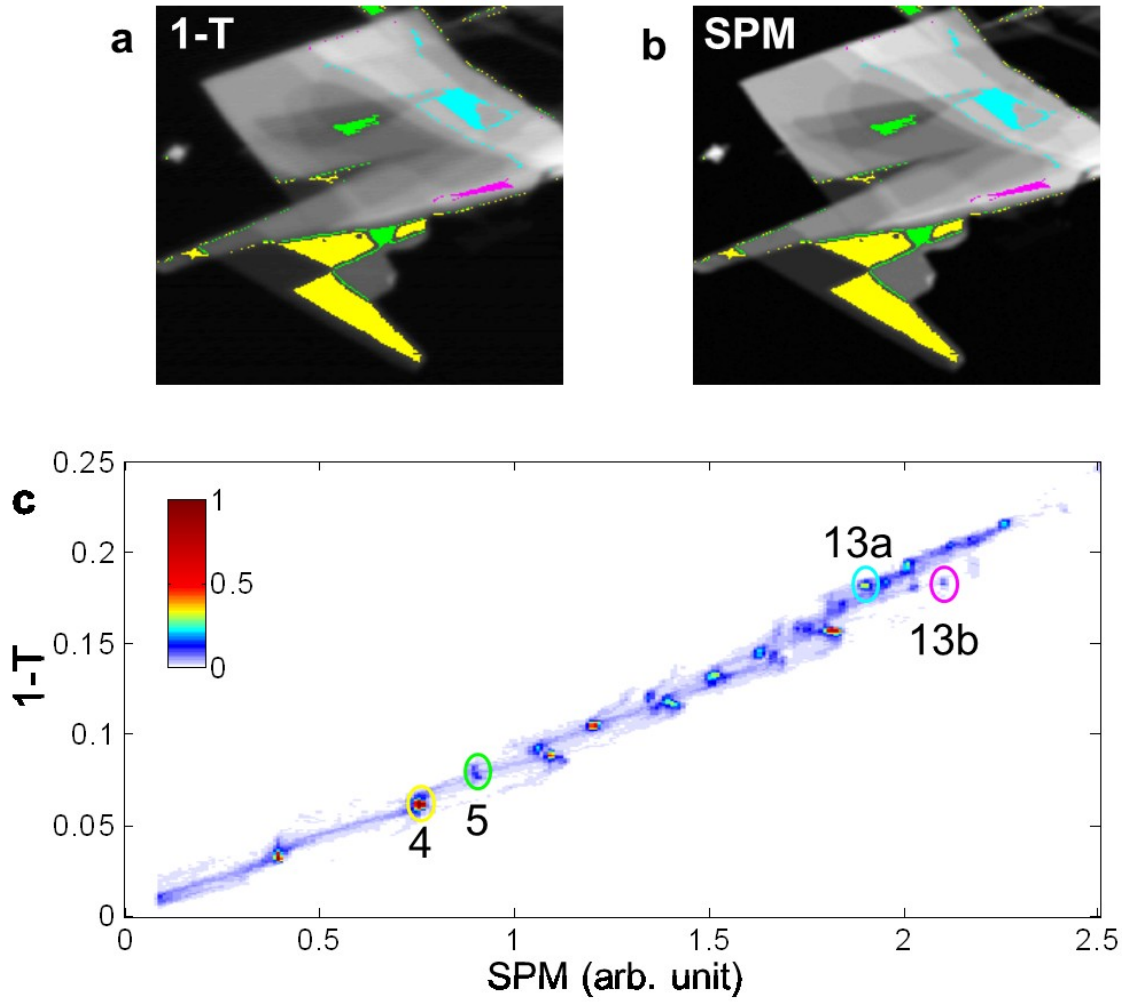

Figure 4.14: Layer counting in few-layer graphene flakes. (a), Transmission contrast; (b), SPM contrast of the same sample; (c), 2D histogram of transmission and SPM contrast, where colored circles label the region with a certain number of layers obtained from transmission. These regions are highlighted in parts (a) and (b) in the corresponding colors. Regions 13a and 13b in (c) are of the same number of layers but at different locations. They produce different SPM signals because they experienced slightly different laser powers.

With these scaling relations, we convert both transmission and SPM signals to the equivalent number of layers for each individual pixel and re-plot the 2D histogram in Figure 4.15 (a). A saturation factor of $\eta = 0.71$ provides good agreement between our experimental results and the theoretical model: the peaks in the transmission histogram align well to the grid (the right panel in Figure 4.15 (a)); though it has been previously noted that the existing models for fitting FWM signals with the number of layers does not fit quantitatively [107, 131] (see Figure 4.15 (b)). One possible reason for this discrepancy is omission of the saturation in nonlinear optical response in the previously published models. However, as we showed in the last section, the nonlinear response in fact is power dependent, at least in single layer graphene. In a few-layer graphene flake, the lowest layers (exposed to the attenuated laser power) would be expected to have a higher effective $\chi^{(3)}$. Not considering this effect would lead to an underestimate of the nonlinear signal from a few-layer graphene flakes, particularly for large layer numbers. Further work will be needed to verify this effect as the source of the deviation between theory and experiment.

The background in the 2D histogram arises from boundary areas that overlap different layers within the image resolution. Note that the resolution is significantly better for the nonlinear approach; for instance, a small 5-layer region (labeled in Figure 4.12 (a)) is clearly shown in the top histogram (of the nonlinear signal), but almost buried in the background in the right histogram panel. The fact that these 'islands' are thinner across the x-axis further confirms the higher resolution of the nonlinear method

compared to transmission. For large numbers of layers, the incremental change in the nonlinear signal gets smaller, and the variations in the laser intensity of the scanning beam likely lead to deviations from the ideal calibration. The real significance, however, is that the SPM contrasts are still observable in a scattering sample, but transmission contrast is seriously distorted and completely useless for layer counting.

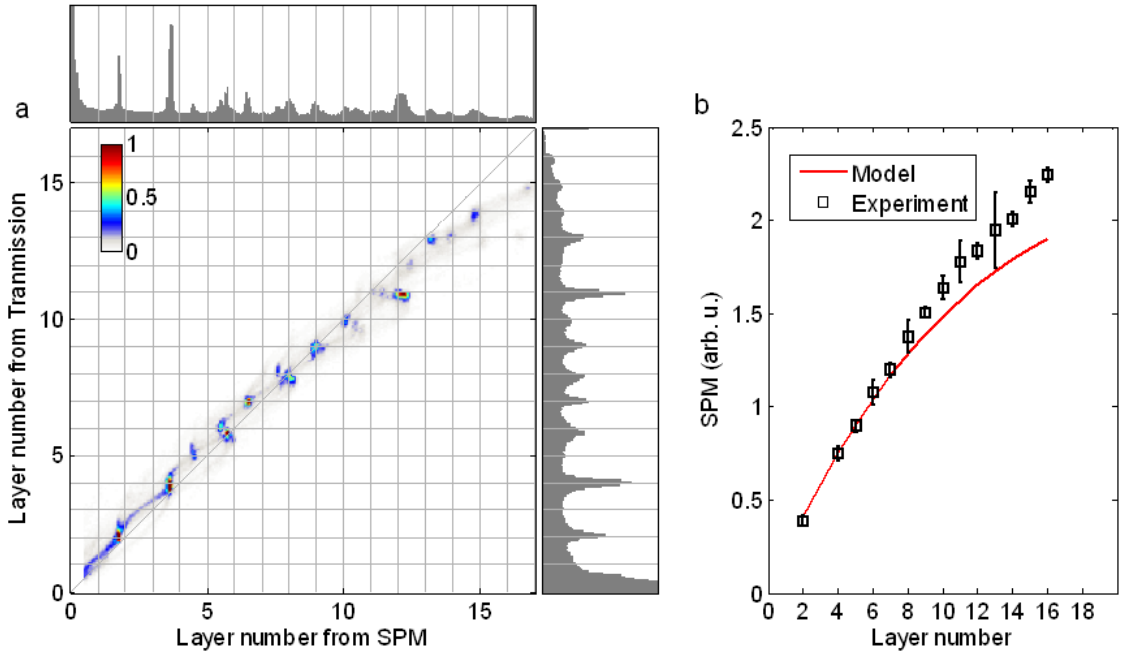

Figure 4.15: Comparison of graphene flake layer counting by transmission and nonlinear contrast. The major panel (a) plots the 2D histogram of the number of layers, where the populations from blank areas are masked. The top and right panels plot the histogram of number of layers converted from SPM and transmission contrast. In (b), The SPM signal was plot as a function of number of graphene layers. The red curve plots the scaling model $NS/(1+NS)^5$ with S obtained by fitting the small-layer transmission data. The misalignment in the top panel is due to this less accurate model for SPM for conversion.

4.5. Imaging different graphene samples

4.5.1. Reduced graphene oxide preparation

Among all available methods to manufacture graphene, the reduction of graphene oxide (GO) is probably the most promising method for large scale production and the most appropriate choice for biomedical applications. In our experiment, reduced graphene oxide (RGO) was produced by reducing the GO made by the modified Hummers method, as described elsewhere [133, 134]. To make the GO, 2 g of natural graphite flakes, 2 g of $NaNO_3$, and 90 ml of concentrated H_2SO_4 were mixed in a flask that was stirred in an ice bath. 12 g of $KMnO_4$ was then added slowly to avoid overheating. The mixture obtained was first stirred in an ice bath for 1.5 hours and then at 35°C for 2 hours. Next, 90 ml nanopure water was added dropwise to dilute the mixture, followed by an addition of 200 ml nanopure water and 10 ml H_2O_2 (30%). The obtained mixture was then subjected to three steps of centrifugation at 16,000 rpm to remove the residual salts and acids. The centrifuged slurry was collected at each step and dispersed in nanopure water prior to the next centrifuge step. Following centrifugation, a mild sonication (20 min) was used to exfoliate the GO. Next, a low-speed centrifuge at 7,000 rpm was used to remove large, thick, multilayer GO until the supernatant was free of visible particles. The graphene oxide suspension thus obtained was used for reduction after dilution with nanopure water to the targeted concentration (0.25 mg/ml).

The reduction of GO followed the method developed by Li *et al* [135]. 18.0 µl of hydrazine solution (35% in water) and 126 µl of ammonia solution (28% in water) were added to 36 ml of graphene oxide dispersion in a flask. After vigorous shaking for a few minutes, the flask was put in an oil bath that was kept at ~90°C for 1 hour. The solution was then cooled to room temperature and subjected to dialysis against ~0.5% ammonia solution for 24 hours to remove the excess hydrazine. Finally, gum arabic (GA) was added (mass ratio of 4:1 with respect to reduced graphene oxide (RGO)) to the RGO suspension to further stabilize the RGO sheets as a surfactant. The final GA-stabilized RGO dispersion is stable for several months without noticeable aggregation or precipitation.

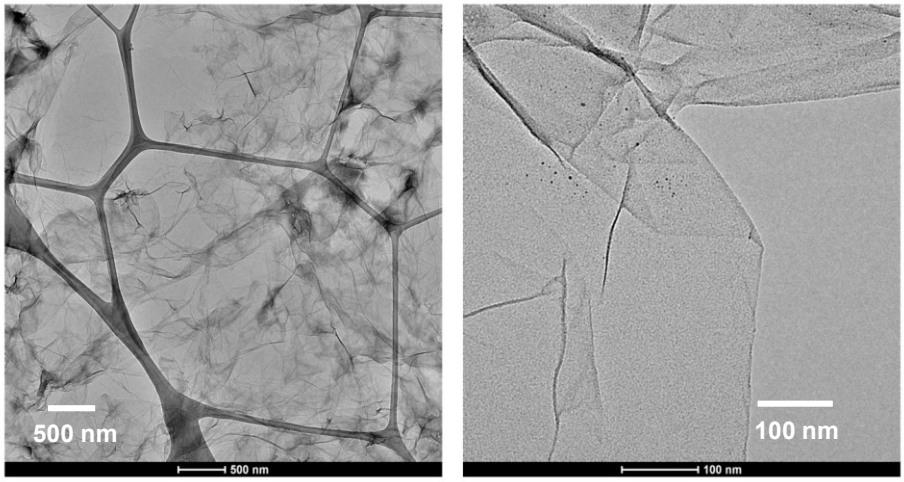

Figure 4.16: TEM images of reduced graphene oxide. The folded edges and wrinkles increase the effective number of layers, thus producing larger nonlinear signals.

The final RGO product is characterized by high resolution TEM, and the images are as shown in Figure 4.16. The sample under examination is composed of small RGO flakes with scrabbled edges, which are attached to each other. Nevertheless, the RGO

flakes are well dispersed and the number of layers is well controlled to fewer than 10. For optical characterization, a GA-stabilized RGO suspension is coated on a glass slide, which is dried overnight at room temperature and then mounted on the sample stage for microscopy imaging. We also use a GA-stabilized RGO suspension for cell incubation.

4.5.2. Nonlinear optical characterization of different carbon products

To make sure that our technique is able to discriminate graphene from other types of carbon products, we perform nonlinear imaging on amorphous carbon (AC), GO and RGO under the same conditions. All samples are made through the same procedure: each suspension of AC, GO and RGO is coated on a glass slide, which is then dried overnight at room temperature. As shown in Figure 4.17 (a), no signal is produced in the nonlinear microscopy image of AC, even though a substantial amount of AC micro particles are obviously shown in the transmission image. This is due to the fact that AC does not possess any significant nanostructures. At the same power level, GO does not produce any appreciable nonlinear signal either (Figure 4.17 (b)), which is expected since GO does not possess the desired linear dispersion relation, despite the single-layer nature of GO. After exposure to high optical power levels, GO can, however, show strong nonlinear signals; we suspect this is due to the permanent light-induced reduction of GO[136]. In Figure 4.17 (b), the left side of the GO sample was scanned for 3 minutes with 4 mW input power and turned into RGO, producing significant SPM signal.

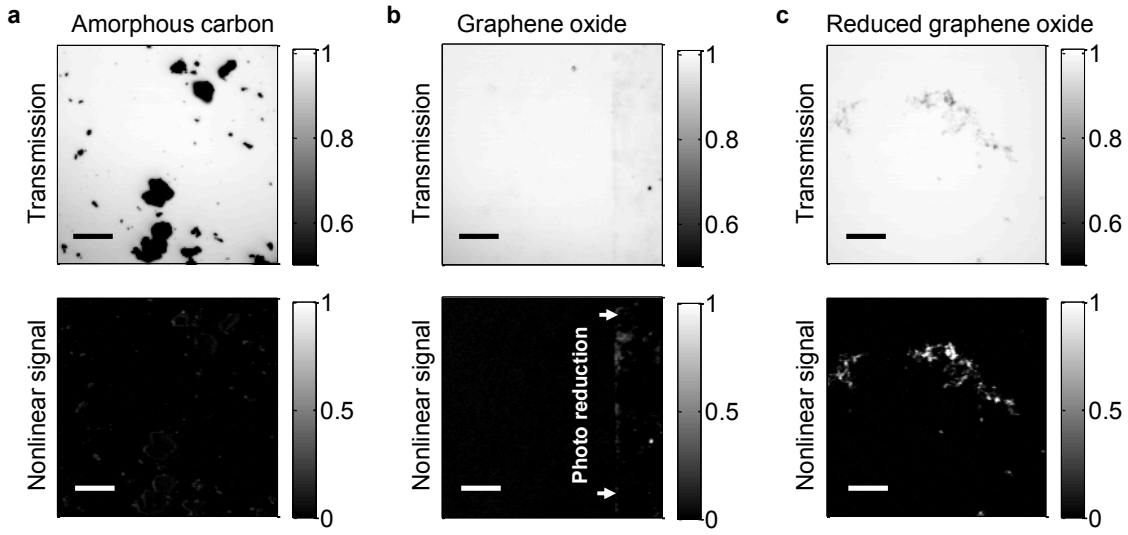

Figure 4.17: Transmission and nonlinear optical images of amorphous carbon (a), graphene oxide (b), and reduced graphene oxide (c). The strip on the left side in (b) is photoreduced and turned into graphene, thus it becomes less transparent and produces a nonlinear signal (see text). Scale bars are 20 μm. The laser power is 0.7 mW, and the objective is 40x, 0.75 NA. Acquisition speed is 6.4 s per frame, and the images are averaged over 4 frames.

4.5.3. Nonlinear imaging of different graphene samples

Figure 4.18 compares graphene samples produced by mechanical exfoliation[137], chemical vapor deposition (CVD) growth and chemical RGO. Monolayer graphene produced by CVD extends over a large scale (up to 1mm), but the morphological inhomogeneity at the micrometer scale is higher than in mechanically exfoliated graphene flakes. Dotted bright lines in Figure 4.18 (b) may be caused by granular boundaries on the copper foil where the graphene monolayer is grown, and the small holes and bright spots are likely due to scratching or contamination during the production and the transformation process. Although the physical appearances of CVD

and mechanically exfoliated films are different, their nonlinear optical properties are quite similar. The nonlinear signal amplitude and phase values of single-layer exfoliated graphene (A=0.16±0.004, θ = -0.24±0.09 rad) are very close to the values for CVD growth monolayer graphene (A = 0.18±0.006, θ = -0.21±0.07 rad). This phase is also almost identical for graphene flakes with different numbers of layers in Figure 4.18 (a), implying that SPM and TPA satisfy very similar layer-number scaling.

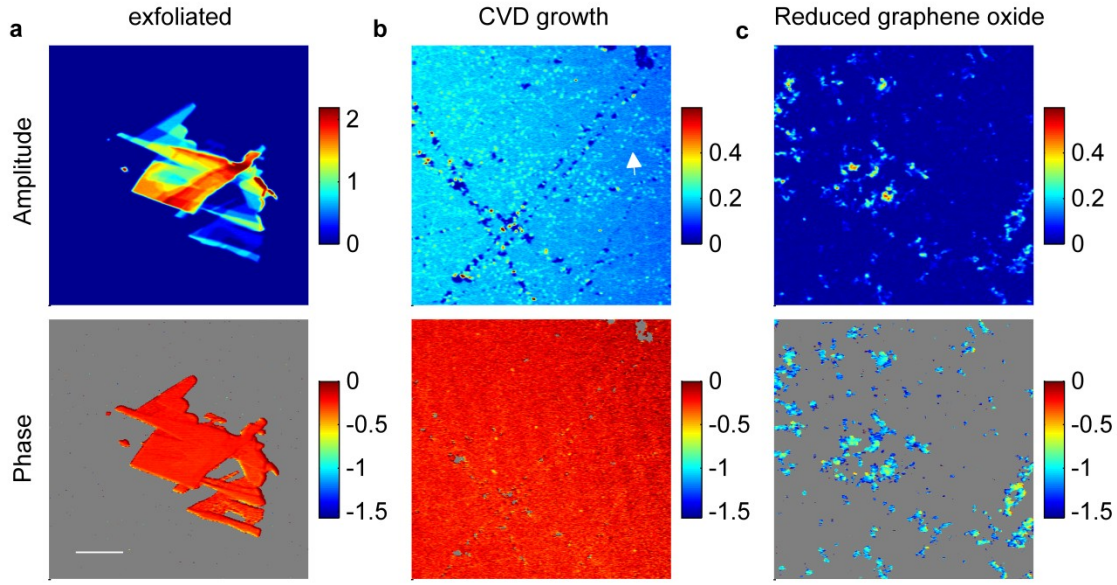

Figure 4.18: Nonlinear amplitude and phase images of different types of graphene. (a) Mechanically-exfoliated few-layer graphene flakes; (b) CVD growth monolayer graphene transferred onto a glass substrate; (c) Gum arabic-stabilized reduced graphene oxide suspension dispersed on a glass coverslip. The arrow in (b) shows bright dotted lines that may be caused by granular boundaries on the copper foil. In the phase images, the low-amplitude areas are masked. All images are acquired with 0.7 mW input power. Acquisition time is 6.4 s per frame, and the images are averaged over 4 frames. The scale bar is 20 μm.

However, RGO exhibits very distinct behavior compared to the few-layer graphene sample. From Figure 4.18 (c) we can see that RGO flakes are well dispersed on

the glass coverslip, since the RGO suspension used to make this sample is stabilized with gum arabic. As revealed by high resolution TEM images in Figure 4.16, the edges and contact regions (equivalently more layers) produce much higher nonlinear signals, indicated by the bright edges in Figure 4.18 (c). The average signal strength is comparable to few-layer graphene flakes from exfoliated graphene samples, however, the phase in the RGO samples (-1.0±0.3 rad) is vastly different from the other two types of graphene, and the inhomogeneity across the sample is larger. The phase shifts towards TPA, indicating that the residual oxidization might result from strong nonlinear absorption. Another possible source for this phase variation is the morphological inhomogeneity of the RGO flakes.

4.6. In vitro imaging of graphene in breast cancer cells

To demonstrate the ability to image graphene in biological environments by spectral reshaping, we acquired *in vitro* images of breast cancer cells incubated with gum arabic-stabilized RGO flakes. The cell culturing and graphene incubation are conducted by our collaborator Dr. Hsiangkuo Yuan from Duke University, department of biomedical engineering. The BT549 cancer cells were a gift from Dr. Victoria Seewaldt. Cells were incubated in RPMI 1640 medium (Invitrogen; Carlsbad, CA) containing 10% of fetal bovine serum (FBS), 25 mM HEPES and 0:023 U ml-1 of insulin, in an incubator with a humidified atmosphere (37 ºC, 5% CO2). Cells in the exponential growth phase were used in experiments. The 100mg/L gum arabic-stabilized RGO suspension (mass ratio:

gum arabic : RGO = 4:1) is diluted to a final concentration of 10 mg/L in the growth medium and incubated with 80% confluent BT549 cells for 24 hours. The cells were fixed with paraformaldehyde (4%, 10 min) and washed with phosphate-buffered saline twice.

A transmission image of a breast cancer cell is displayed in Figure 4.19 (a); where RGO flakes and aggregates are noticeable but present very little contrast. The co-registered nonlinear optical image in Figure 4.19 (b), on the other hand, highlights only the distribution of RGO flakes. Overlaying SPM contrast onto the transmission image clearly shows how the RGO flakes are distributed within the cell and its environment (Figure 4.19 (c)). While the majority of the flakes are attached to the cell membrane, some flakes are trapped in the cytoplasm and others are floating in the culture medium. Although Figure 4.19 just shows images taken at a specific depth, our technique is capable of 3D optical sectioning, and a stack of images at different depths can be taken and presented in a movie file [89].

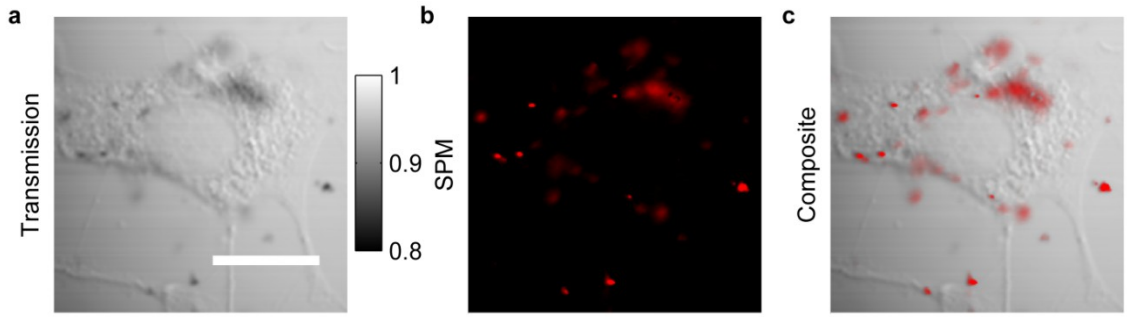

Figure 4.19: *In vitro* graphene imaging in BT549 breast cancer cells. (a) Transmission contrast displaying a cell. (b) SPM contrast highlights the distribution of graphene flakes. (c) Composite image of both transmission and SPM contrasts. Laser power before the objective is 1 mW. Acquisition time is 3.2 s per frame, and the images are averaged over 8 frames. The scale bar is 20 μm.

4.7. Conclusion

Our technique provides several potential advantages over other available nonlinear imaging methods. For example, pump-probe microscopy can also image graphene, but our homodyne technique discerns the nonlinear phase (the SPM/TPA ratio), which is independent of the number of layers in exfoliated and CVD grown graphene. Thus phase can distinguish graphene response from the many other TPA and SPM processes in complex materials such as tissue. In addition, our technique utilizes a one-color laser system which is simpler and less expensive than the two-color laser system used in pump-probe and previous CARS-type FWM microscopy.

In conclusion, we have developed a versatile nonlinear optical imaging technique for quantitative graphene imaging in both solid-state and biological environments. This technique can be easily incorporated into a commercial multi-photon microscope to provide additional valuable nonlinear optical contrasts. The high contrast nonlinear optical images can quantify the layer number of few-layered graphene flakes with high resolution even on a scattering surface, which might be useful in solid-state graphene studies and in optoelectronic applications. With 3D optical sectioning, sub-micrometer resolution, and fast imaging speed, our spectral reshaping nonlinear optical imaging technique also offers a promising way to study nano-bio interactions and the cytotoxicity of graphene products.

5. Phase-cycling coherent anti-Stokes Raman scattering

This chapter will explore a pulse shaping technique to suppress the nonresonant background in coherent anti-Stokes Raman scattering (CARS) and to reveal the phase information of the nonlinear Raman signal. After introducing the basic concepts of CARS, we will discuss in detail the theory of this new phase-cycling CARS technique (PC-CARS). We will describe the experimental set up for PC-CARS and demonstrate its capability and high sensitivity by measuring the CARS signal of solutions of benzene in carbon disulfide with various concentrations.

5.1. Introduction to CARS

The vibrational level structure of biomolecules could provide highly specific structural, metabolic and functional contrast in tissue. Infrared spectroscopy is able to obtain this information but its application to tissue imaging is hindered by strong water absorption. Raman scattering using visible or near infrared (NIR) light can penetrate much deeper in tissue; unfortunately, the Raman cross sections of intrinsic markers are generally small, and sensitive measurement techniques are required for biologically relevant concentrations [18]. Spontaneous Raman and CARS effects imprint the vibrational spectrum onto light scattered from the sample, and thus both techniques can be used to obtain spectroscopic information from tissue [138]. However, CARS offers several advantages [2, 40]. First, as a nonlinear optical technique, CARS can provide all the benefits mentioned in Chapter 1, including 3-D optical sectioning and better

performance in a scattering medium. Second, the anti-Stokes signal, which is emitted at a shorter wavelength with respect to the incident light, is not contaminated by autofluorescence. CARS has a broad range of biomedical applications, including metabolic imaging, imaging lipid structure and studying drug delivery.

5.1.1. Signal generation in CARS

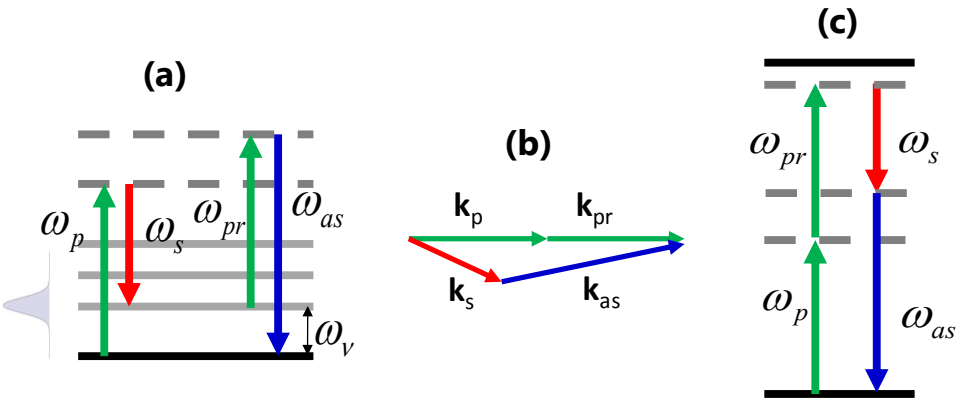

Figure 5.1: (a) Energy level schemes of coherent anti-Stokes Raman scattering; (b) Phase matching diagram of CARS; (c) Energy level schemes of nonresonant four-wave mixing. Solid (dashed) lines indicate real (virtual) states.

CARS is associated with the third-order nonlinear susceptibility $\chi^{(3)}$ and can be treated as a vibrationally-resonant four wave mixing (FWM) process [2]. As illustrated in Figure 5.1 (a), the combined optical field of pump E_p, Stokes E_s and probe E_{pr} light (the pump and probe fields are usually degenerate $\omega_p = \omega_{pr}$, and the frequency of the Stokes field is ω_s) interacts with the nonlinear medium to generate anti-Stokes light at a new frequency $\omega_{as} = 2\omega_p - \omega_s$. Assuming that both pump and Stokes fields are plane waves, the intensity of the anti-Stokes signal can be described as [40, 70],

$$I_{as} \propto \left|\chi^{(3)}\right|^2 I_p^2 I_s \left(\frac{\sin(\Delta kl/2)}{\Delta kl/2}\right)^2, \tag{5.1}$$

where I_p and I_s are intensities of the input pump and Stokes light, l is the thickness of the sample, and Δk is the wave vector mismatch. Because the medium is generally dispersive, the wave vector ($2\mathbf{k}_p$-$\mathbf{k}_s$) of the nonlinear polarization might not match the wave vector of the anti-Stokes field $\mathbf{k}_{as}$, as shown in Figure 5.1 (b). It is the wave vector mismatch Δk, defined as $|\mathbf{k}_{as} - (2\mathbf{k}_p - \mathbf{k}_s)|$, that makes CARS phase-sensitive. A proper phase relation between the interacting fields must be maintained along the propagating direction in order to eliminate or minimize this mismatch. Otherwise, signals from different locations will destructively interfere.

To relax the phase matching condition, CARS microscopy usually employs a collinear geometry in which both the pump and Stokes beams are tightly focused into the sample. The nonlinear interaction is confined to the focal volume, leading to a very short interaction length l. As long as l is smaller than the coherence length $l_c = 1/\Delta k$, destructive interference can be prevented. Additionally, within the focal volume, the wave vectors of the excitation photons possess a large range of directions; therefore there are always enough photons to fulfill the phase matching condition.

There are two contributions in the anti-Stokes signal: resonant signal and nonresonant background [2]. As indicated in Figure 5.1 (a), the anti-Stokes signal can be resonantly enhanced when the frequency difference $\Delta = \omega_p - \omega_s$ is tuned to the Raman

active vibrational transition ω_v. We can attribute this contribution to a resonant third-order nonlinear susceptibility

$$\chi_{res}^{(3)} = \frac{A}{\Delta - \omega_v - i\Gamma}, \tag{5.2}$$

where Γ is the bandwidth of the Raman line. The nonresonant background comes from any other third-order processes that only involve virtual states. For example, as shown in Figure 5.1 (c), spontaneous absorption of two photons with frequency ω_p and emission of a photon with frequency ω_s can generate a new photon at ω_{as} without exciting a vibrational state. This nonresonant FWM process could be aggravated when $2\omega_p$ approaches an electronic transition (this enhanced FWM process was used to image nanoparticles and graphene in Chapter 3 and Chapter 4). We attribute this nonresonant contribution to a nonresonant third-order nonlinear susceptibility $\chi_{nr}^{(3)}$. Considering contributions from both parts, the intensity of the CARS signal can be written as

$$I_{CARS}(\Delta) \propto \left|\chi^{(3)}\right|^2 = \left|\chi_{nr}^{(3)}\right|^2 + \left|\chi_{res}^{(3)}\right|^2 + 2\chi_{nr}^{(3)}\,\mathrm{Re}[\chi_{res}^{(3)}(\Delta)], \tag{5.3}$$

where $\mathrm{Re}[\chi_{res}^{(3)}]$ denotes the real part. The first term is independent of frequency difference and hence constitutes a purely nonresonant background. The second term is purely from the resonant contribution. It dominates if we are probing concentrated Raman scatterers, showing a prominent peak at the Raman transition. The third term mixes both nonresonant and resonant contributions, usually giving a dispersive line

shape. This mixed term distorts the line shape (i.e. shifts the position of the Raman peak or mixes two adjacent Raman peaks) which makes the identification of a Raman signature very difficult.

5.1.2. Background suppression techniques in CARS

To minimize the effects of the nonresonant background, conventional CARS techniques usually employ synchronized picosecond laser pulses for excitation. Since the lifetime of the vibrationally excited states is on the picosecond time scale, excitation with picosecond lasers can significantly improve the signal-to-background ratio. The reason for using picosecond laser pulse is even more straightforward in the frequency domain. Picosecond (pump, probe and Stokes) laser pulses have a bandwidth close to the Raman transition width. As a result, the CARS signal is optimally enhanced when the frequency difference between pump and stokes match the Raman shift.

Additional background suppression is still needed to resolve weak Raman transitions or to perform CARS measurements where the concentration of molecules of interest is low. In both scenarios, the nonresonant background can be much greater than the Raman signature. Because the nonresonant background does not depend on frequency, background suppression is more critical for broadband CARS.

Several CARS techniques have been invented to suppress the nonresonant background. The time-resolved CARS technique takes advantage of the finite lifetime of excited vibrational states and introduces a probe pulse at a later time (~ 1ps) to

eliminate the instantaneous FWM background. In this case, the signal-to-background ratio increases at the expense of the decrease in the resonant CARS signal, which decays exponentially due to the population depletion of excited states. The three-color configuration also makes the instrument too complicated for imaging application.

The signal-to-background ratio can also be improved by polarization-sensitive detection [139-141]. Both $\chi_{res}^{(3)}$ and $\chi_{nr}^{(3)}$ are 4th rank tensors, but they have different symmetries, leading to their distinct dependence on the polarization of the incident lasers. Therefore, by choosing a proper configuration for the linearly polarized pump and Stokes fields, resonant and nonresonant CARS signals can be distinguished based on their detected polarization direction. In this case, introducing an appropriately oriented analyzer can eliminate the nonresonant background with a trade off in the resonant signal. The polarization-sensitive detection works only if the polarization of excitation and emission light is preserved. However, this assumption usually does not hold in highly scattering media such as tissue.

Background-free CARS is possible by performing interferometric measurement, which distinguishes the resonant from nonresonant polarization by taking advantage of the difference in their phase properties: $\chi_{nr}^{(3)}$ is real, while $\chi_{res}^{(3)}$ is a complex number. A reference anti-Stokes field with a pre-determined phase (i.e., local oscillator (LO)) can extract the imaginary part of the resonant contribution by homodyning the signal, and

the local phase at the focus can be measured at the modulation frequency of the LO to compensate for variations caused by scattering [142, 143].

Pulse-shaping approaches of varying complexity have also been implemented to suppress the nonresonant background in broadband CARS [81, 144-149]; for example, one approach uses the real, nonresonant polarization generated at the focus within the sample as a LO to interfere with the resonant component that is appropriately phase-shifted by a pulse shaper [81], and then uses a high resolution spectrometer to extract the background-free Raman contribution. The drawbacks of the existing techniques are that they either rely on a LO that is supplied externally to the sample and can thus not be perfectly controlled [142, 144-146], or uses a monochromator to spectrally analyze the Raman contributions [81, 147, 148]. Because of the wavelength difference between the CARS-generating beams and the LO, an externally supplied LO experiences a different effective propagation path (and fluctuations thereof), leading to an unstable interference with the generated CARS radiation. The use of a monochromator is troublesome because its performance is inevitably degraded by scattering.

5.2. Theory of Phase-cycling CARS

Here we report a phase cycling technique to suppress the nonresonant background. In contrast to previous methods, our approach uses a femtosecond pulse shaping technique with rapid update rates at a few kHz [59, 83] to generate both a static nonresonant LO and a phase-rotating resonant contribution at the focus within the

sample. These two contributions result in an inherently stable interference that can be recorded with a detector and a lock-in amplifier without the need for a high-resolution spectrometer.

5.2.1. The principle of phase-cycling CARS

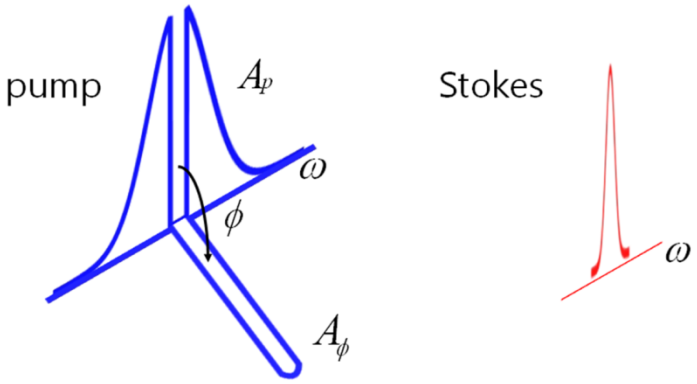

Figure 5.2: Pulse shapes for phase-cycling CARS. A broadband pump/probe pulse is created with a narrowband portion that is incremented in phase from one pulse to the next, and is applied with a narrowband Stokes pulse. Both beams are linearly polarized along x axis. The detection is not polarization-sensitive.

The principle of the phase-cycling CARS is illustrated in Figure 5.2. The broadband pulse, serving as the degenerate pump/probe pulse, is shaped such that the phase ϕ of a narrow portion in the center of the spectrum is incremented from one pulse to the next (the rotating portion). The spectral width of the rotating portion and the bandwidth of the Stokes pulse are much narrower than the pump bandwidth and are approximately the Raman linewidth. These two pulses interact with the third-order optical nonlinear susceptibility $\chi_{nr}^{(3)} + \chi_{res}^{(3)}(\Delta)$, where the nonresonant susceptibility $\chi_{nr}^{(3)}$ is real and assumed to be frequency independent, and the Raman susceptibility $\chi_{res}^{(3)}(\Delta)$

is complex and depends on the difference $\Delta = \omega_p - \omega_s$ between the pump and the Stokes frequencies. Although here we place the rotating portion in the center of the pump spectrum ($\omega_\phi = \omega_p$), its exact position is not critical.

The interaction within the sample leads to static and phase-rotating polarizations. The static polarization is dominated by the nonresonant component (FWM), which scales as $P_0 \propto 2\chi_{nr}^{(3)} A_p^2 A_s$, where A_p and A_s are the square root of the intensity of the pump/probe and Stokes pulses, respectively. This nonresonant component gives rise to a broadband four-wave mixing signal centered at the anti-Stokes frequency ($2\omega_p - \omega_s$), which constitutes the static LO. The phase-rotating polarization has components originating from both $\chi_{nr}^{(3)}$ and $\chi_{res}^{(3)}$. $\chi_{nr}^{(3)}$ generates two identical components (one for which the phase-rotating portion serves as the pump and the static portion as the probe, and another with the reverse order), which scale as $P_{\phi,nr} \propto 2\chi_{nr}^{(3)} A_p A_s A_\phi$, where A_ϕ is the square root of the intensity of the phase-rotating spectral component. The dominant resonant component $P_{\phi,res} \propto 2\chi_{res}^{(3)}(\Delta) A_p A_s A_\phi$ originates from the molecular coherence created by the phase-rotating portion and the Stokes pulse, which is then probed by the broad static portion. This resonant component gives rise to a broadband anti-Stokes Raman signal centered at $\omega_p + \omega_\phi - \omega_s$, where $\omega_\phi = \omega_p$ is the frequency of the narrow rotating portion. We measure both quadratures of the phase-rotating component

$$S_{\phi f} \propto \chi_{nr}^{(3)} A_p^2 A_\phi A_s^2 \left\{ \left[\chi_{nr}^{(3)} + \mathrm{Re}[\chi_{res}^{(3)}(\omega_\phi - \omega_s)] \right] \cos\phi + \mathrm{Im}[\chi_{res}^{(3)}(\omega_\phi - \omega_s)] \sin\phi \right\}, \quad (5.4)$$

of the anti-Stokes intensity $\left|P_0 + P_\phi \exp(i\phi)\right|^2$ with a lock-in detector. The out-of-phase component (imaginary channel) measures only the imaginary part of the Raman susceptibility and is background free; the in-phase component (real channel) contains the dispersive part of the Raman term plus a nonresonant FWM offset. Here all our input laser beams are linearly polarized along x direction. In a centrosymmetric material, such as tissue, the only tensor component we measured is $\chi^{(3)}_{xxxx}$. In this chapter we treat $\chi^{(3)}$ as a scalar to represent this particular component.

This phase-cycling CARS method is not a broadband multiplex technique, in the sense that it does not resolve multiple Raman transitions in a single shot; here, selectivity is achieved by tuning the frequency difference between the narrowband Stokes and the narrowband rotating portion in the broad pump spectrum (ω_ϕ-ω_s). When this frequency difference coincides with a Raman transition, we obtain an absorptive peak in the imaginary channel and a dispersive feature in the real channel.

The femtosecond pulse shaper effectively creates a combination of a picosecond pulse (the rotating narrow portion) and a femtosecond pulse (the static pump), and, in this sense, the CARS application is similar to the *ps-fs* scheme reported in [148], where if the two pulses are out of phase (both containing a fixed inter-pulse phase) and their relative spectral amplitudes are carefully matched, the nonresonant background generated from the two pulses cancel. Note that the picosecond pulse generates a much larger resonant signal than the femtosecond pulse, due to its much narrower spectral

distribution. As a result, the total resonant signal is not balanced and does not cancel, and background free measurement can be achieved. In our case, however, our ability to dynamically rotate the phase of a narrow portion of a broadband pump lets us retrieve both dispersive (real channel) and absorptive (imaginary channel) Raman features. In addition, precise amplitude matching between the picosecond and the femtosecond pulse is not necessary. Finally, while the *ps-fs* scheme is a broadband CARS technique that relies on a spectrometer to obtain spectral resolution, the spectral resolution of our phase-cycling CARS is determined by the frequency difference between narrowband Stokes and the narrowband rotating component of the pump without the need for spectral analysis of the anti-Stokes radiation.

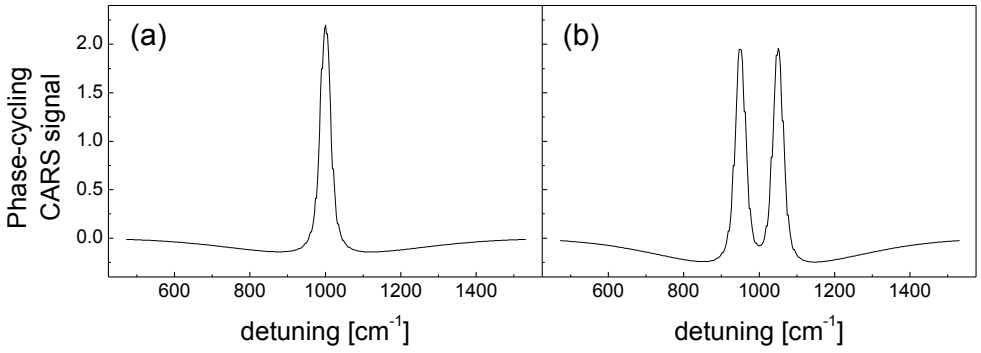

Figure 5.3: Simulation of the phase-cycling CARS signal with a single (a) and multiple (b) Raman lines within the broad bandwidth of the pump/probe pulse.

The local oscillator that is used in our technique for homodyning is spectrally much wider than the Raman lines to be investigated. This ensures that even in congested regions of the Raman spectrum the local oscillator does not vary substantially when probing different Raman frequencies. The presence of several Raman lines within

the broad bandwidth of the pump pulse does not produce interference cross terms, but merely superimposes the individual lines, as demonstrated in Figure 5.3.

5.2.2. Comparison of phase cycling-CARS with narrowband CARS

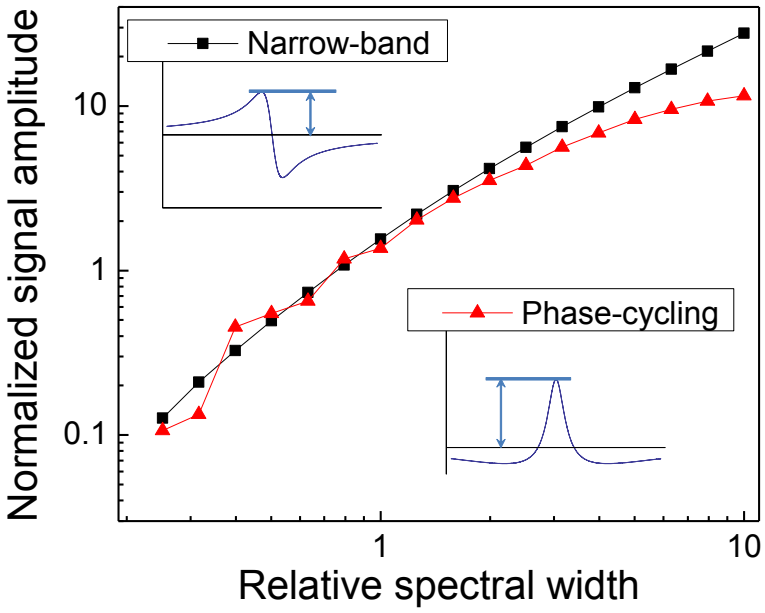

Figure 5.4: Simulation of narrowband and phase cycling CARS signal amplitudes. The spectral width (Stokes and pump in the narrowband case, Stokes and phase rotating portion in the phase-cycling case) are relative to the width of the Raman line. The signal amplitudes are normalized by the factor $E_p^2 E_s$. The variations for low spectral widths for phase-cycling CARS are caused by the discrete values for the width of the local oscillator slice.

It is instructive to compare the relative signal strengths of our phase-cycled CARS with those obtained by conventional narrowband CARS. For a large nonresonant susceptibility (as is present in low-concentration samples) narrowband CARS, as a function of detuning, yields a dispersive line shape with a large nonresonant offset. We therefore regard the difference between the maximum and the offset as the usable signal amplitude. For spectrally narrow input pulses, the amplitude of this signals scales

as $S_{NB,diff} \propto \delta^2 E_p^2 E_s \chi_{nr}^{(3)} \mathrm{Re}[\chi_{res}^{(3)}]_{\max}$. Here, δ is the spectral width of the pump and Stokes pulses and E_p and E_s are the pulse energies of the pump and Stokes pulses, respectively. For phase-cycling CARS, the measurement is background-free and the peak amplitude is used for comparison. In this case, the absolute signal scales as $S_{PC-CARS} \propto \delta^2 E_p^2 E_s \chi_{nr}^{(3)} \mathrm{Im}[\chi_{res}^{(3)}]_{\max}$. Here, δ denotes the spectral width of the Stokes pulse and the width of the phase-rotating spectral portion. The width of the pump pulse was assumed to be much larger than δ. Figure 5.4compares the two signal amplitudes as a function of δ on the same scale. In this figure, both amplitudes were normalized by the pulse energies $E_p^2 E_s$. We can see that for spectral widths on the order of the Raman line width, both techniques yield similar signal strengths for equal pulse energies. While spectrally narrow excitation pulses more efficiently excite Raman transitions, the broad pulses amplify weaker Raman signatures with a strong local oscillator.

5.3. Experimental setup and results

5.3.1. Instrumental design

The experimental setup for our phase-cycling CARS technique is shown in Figure 5.5. A regenerative amplifier (Coherent, RegA) operating at 20 kHz was used as the laser source (~ 60 fs pulses at 800 nm), where 80% of its output pumped an optical parametrical amplifier (Coherent, OPA 9450) to generate a broadband pump/probe beam (~80 fs pulses at 740 nm). This beam was then spectrally shaped with a 4-*f* pulse shaper based on an acousto-optical modulator arrangement [83]. The phase of the

central portion of this spectrum (~0.6 nm wide) was rotated at a rate of 5 kHz. The remaining portion of the RegA output was converted to the narrowband Stokes beam (0.6 nm spectral width, ~900 fs pulse length) by another 4-*f* pulse shaper acting as a spectral filter. Both beams were combined with a dichroic mirror and focused into the sample cuvette with a microscope objective (NA 0.25) resulting in a focal size of about 1.1 μm. The anti-Stokes light was separated from the transmitted beam with a 700 nm short-pass filter, detected with a biased photodiode, time-gated with a boxcar integrator (Stanford Research Systems, SR250), and measured with a lock-in amplifier (Stanford Research Systems, SR830) with a time constant of 1 s. To acquire a CARS spectrum, the frequency of the narrowband Stokes pulse was tuned by sweeping the spectral filter through the broad spectrum of the 800 nm input laser.

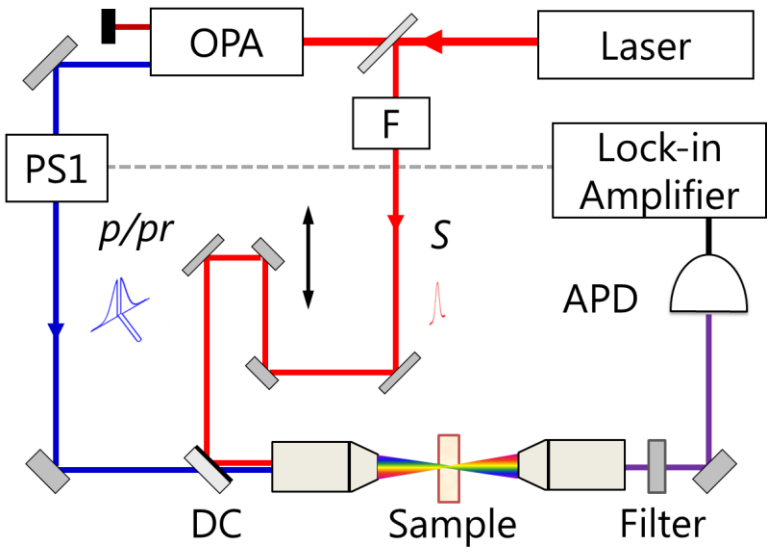

Figure 5.5: Experimental setup for phase-cycling CARS. PS, pulse shaper; F, tunable spectral filter; OPA, optical parametric amplifier; DC, dichroic mirror; APD, avalanche photo diode.

5.3.2. Experimental results

To demonstrate the concept of phase-cycling CARS, we measured the CARS spectrum of various solutions of benzene in carbon disulfide (CS_2). Benzene has a pronounced Raman transition at 992 cm^{-1} (ring-stretch mode), while CS_2 has no strong modes in the region from 750 cm^{-1} to 1300 cm^{-1} (CS_2 and benzene have weak Raman transition at 800 cm^{-1} and 1200 cm^{-1}, respectively). For comparison, we also acquired standard CARS spectra with narrowband (about 0.6 nm) pump/probe and Stokes pulses. In order to account for the variation in power when tuning the Stokes wavelength, we normalized the acquired traces by the signal from pure CS_2.

Figure 5.6 (a) shows the narrowband CARS spectrum for benzene (100% volume concentration) with a peak at around 1000 cm^{-1}, which is distorted by the interference between real and imaginary susceptibilities. Decreasing the concentration leads to decreased signal-to-background ratios and more severe line-shape distortions. For volume concentrations less than 10%, the resonant signal is almost indistinguishable from the large nonresonant background. In comparison, Figure 5.6 (b) and (c) show the real and imaginary channel, respectively, obtained with phase-cycling CARS. As indicated by Eq. (5.4), the real channel signal is a combination of both resonant and nonresonant contributions, resulting in an offset dispersive line shape of the Raman transition. In contrast, the imaginary signal is exclusively due to the resonant contribution, and thus shows an absorptive peak-like feature similar to a spontaneous Raman spectrum.

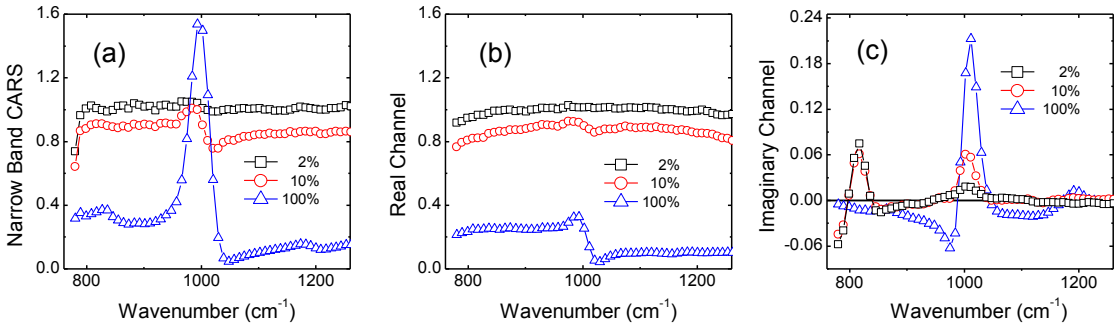

Figure 5.6: (a) Narrowband CARS spectrum obtained for 3 different benzene concentrations (15 μW pump power and 48 μW Stokes power). The signal was normalized by the signal of pure CS_2. The real (b) and the imaginary (c) channel signals from phase-cycling CARS (50 μW pump power and 15 μW Stokes power). The signals were normalized by the real channel signal of pure CS_2. The two absorptive peaks at 800 cm^{-1} and 1200 cm^{-1} are due to weak Raman transitions of CS_2 and benzene, respectively. In all cases the width of the peaks are determined by the spectral width of the pulses, not by the width of the Raman line (~1.5 cm^{-1}).

According to Eq. (4), the signal of our measurement should scale linearly with the Stokes power and quadratically with the pump power. These scaling behaviors are confirmed with measurements based on the 10% volume concentration solution as shown in Figure 5.7 (a). Eq. (4) also predicts that for low benzene concentrations, the phase-cycling CARS signal scales linearly with concentration, which we confirmed with measurements shown in Figure 5.7 (b). Here, the uncertainty (error bars in Figure 5.7 (b), given by the fluctuation of the lock-in amplifier) is almost constant for different volume concentrations. It limits the sensitivity of the current experimental setup to 0.5% volume concentration (when the signal is equal to the uncertainty), corresponding to about 108 benzene molecules in the focal volume. This uncertainty is largely dominated by our detection electronics (primarily by the boxcar amplifier), which prevents shot-noise limited detection. We expect a substantial improvement by adapting this phase-cycling

CARS approach to a rapid pulse shaping technique for mode-locked lasers recently developed in our group [60].

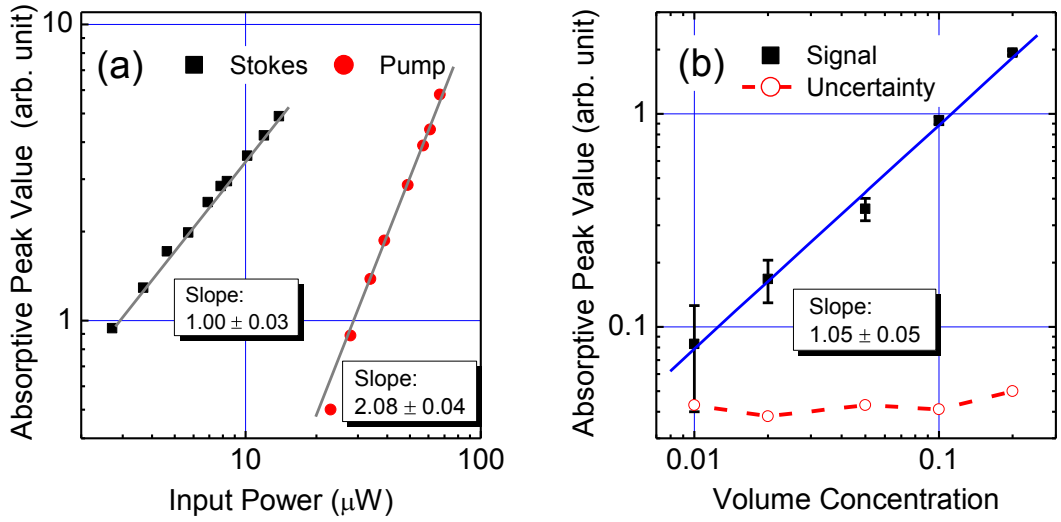

Figure 5.7: (a) Dependence of the strength of the imaginary signal component at 1000 cm^{-1} (absorptive peak value) of phase-cycling CARS on the input Stokes and pump power. (b) Absorptive peak value of phase-cycling CARS as a function of benzene concentration in CS2. Linear fitting on a log-log scale results in a slope value of 1.05 ± 0.05.

To further explore the properties of the phase-cycling CARS technique, we compared our experimental result with numerical calculations, as shown in Figure 5.8 (a) and (b). In these figures we notice weak, broad, negative wings in proximity to the narrow Raman line. These wings originate from the combination of two interference terms: one is between nonresonant static polarization and resonant phase-cycling polarization, the other is between resonant static polarization (it is neglected in the previous theory section, because it is much smaller than the nonresonant static polarization) and nonresonant phase-cycling polarization. These two terms have opposite phase and should cancel; however, due to the factor of 2 in the first term, we

have one contribution left. In order to reduce this effect, we can refine the phase profile of the rotating portion of the pump/probe pulse by inserting a π phase step in the center of the rotating portion [150, 151]. While this phase step does not affect the generated static LO, it suppresses the nonresonant rotating FWM contributions ($P_{\phi nr}$) that are responsible for the broad wings and the large offset of the real channel. Because the introduced phase step can enhance or counteract the inherent change in the phase profile of a Raman resonance depending on its relative phase, lock-in detection can selectively extract the narrow resonant Raman contribution ($P_{\phi res}$). In contrast to [149], however, it is not necessary to closely match the details of the Raman phase profile (we approximate it with a π phase step), easing the demands on the pulse shaper. Figure 5.8 (c) and (d) show calculations and experimental data for such a phase shape. Here the width of the phase-rotating component is about 20 cm^{-1} with the π phase step at its center. The reduction of the width of the negative wings in the imaginary channel and the suppression of the large nonresonant offset in the real channel are apparent. The small offset in the real channel of the experimental data in Figure 5.8 (d) is likely due to a slightly asymmetric shape of our pump/probe spectrum.

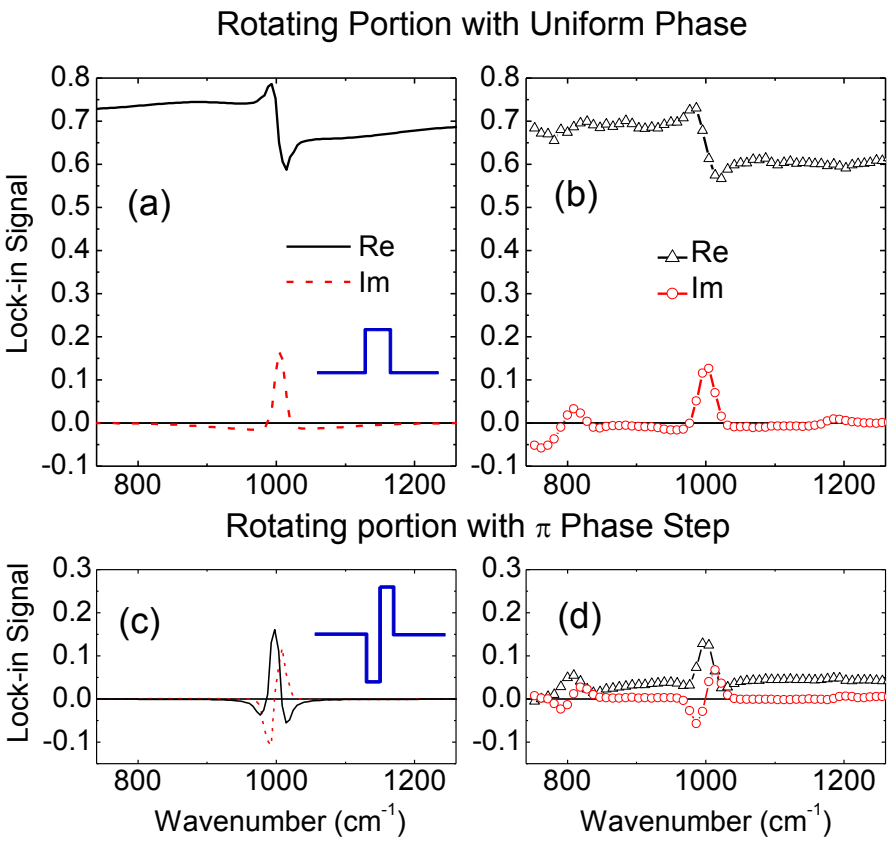

Figure 5.8: Simulation (a) and experimental (b) data for a uniform rotating phase component. Simulation (c) and experimental (d) data for a rotating phase component that contains a π phase step. Insets in (a) and (c) show the phase profile of the rotating component. The sample was 20 vol-% benzene in CS2. For the simulation, only one Raman transition was considered.

5.4. Conclusion and outlook

Our technique could offer several potential advantages for tissue imaging. The local oscillator used for amplification does not have to be supplied, but is generated from ubiquitous, nonresonant four-wave mixing processes at the focus (co-localized with the Raman signal), which provides a stable phase reference even in a highly scattering environment. For weak Raman scatters, the out-of-phase component provides

absorptive Raman signatures, while the in-phase component provides essentially the strength of the LO. In the case of non-uniform four-wave mixing generation (i.e. if FWM itself generates contrast), the in-phase component could be used for normalization of the Raman contrast. Although we cannot record multiple Raman transitions in a single shot, selecting different frequencies out of a broadband Stokes spectrum produces a different vibrational contrast, and a very rapid update is possible. One disadvantage to our technique as compared to the narrowband case is that at the same power, a broader spectrum leads to a shorter pulse and a larger peak intensity, which might limit the maximum laser power in biological imaging.

Our current experimental setup uses an amplified laser system with a pulse-shape repetition rate of 20 kHz, with which high-speed imaging of biological tissue is not feasible. Also, the threshold of photodamage of tissue samples is easily reached due to the high peak intensity of the laser. However, we can extend the pulse shaping technique to 80 MHz mode-locked lasers with lower peak intensity, with a minimum modification of the rapid pulse shaper. We have to replace the edge filter with a notch filter or a band-pass filter and phase-shift the local oscillator. When combined with a suitable dual color source, this proposed rapid pulse shaper should make PC-CARS suitable for high-speed imaging applications.

In addition to CARS, there is another coherent Raman imaging technique, stimulated Raman scattering (SRS), which has advanced very rapidly in the past few years. SRS takes the advantage of the high sensitivity pump-probe detection technique

developed in Warren's group [45, 52-54]. By modulating the pulse intensity of the pump (or Stokes) beam at a MHz rate and measuring the induced Raman gain in the Stokes beam (or Raman loss in the pump beam), one can achieve extremely high sensitivity with the standard dual-color laser sources that are typically used in CARS. For a detailed comparison between CARS and SRS please refer to papers from Xie's group [56, 57]. It is very challenging for PC-CARS to achieve sensitivity higher than that of SRS; however, PC-CARS can produce phase information on the third nonlinear optical susceptibility, which is very unique among all existing nonlinear optical imaging technique. The full potential of PC-CARS is yet to be explored.

In conclusion, we described a homodyne coherent anti-Stokes Raman scattering technique based on femtosecond laser pulse shaping (phase-cycling) and demonstrated it with an amplified laser and AOM-based pulse shapers. This technique utilizes a self-generated nonresonant background as a local oscillator to retrieve phase information on the Raman signal. This technique benefits from being insensitive to scattering and could therefore be applicable for imaging vibrational modes in highly scattering samples such as tissue

References

1. Zipfel, W.R., R.M. Williams, and W.W. Webb, *Nonlinear magic: multiphoton microscopy in the biosciences,* Nat Biotechnol, 2003, 21(11): p. 1369-77.

2. Evans, C.L. and X.S. Xie, *Coherent Anti-Stokes Raman Scattering Microscopy: Chemical Imaging for Biology and Medicine,* Annual Review of Analytical Chemistry, 2008, 1: p. 883-909.

3. Helmchen, F. and W. Denk, *Deep tissue two-photon microscopy,* Nature Methods, 2005, 2(12): p. 932-940.

4. Richards-Kortum, R. and E. SevickMuraca, *Quantitative optical spectroscopy for tissue diagnosis,* Annual Review of Physical Chemistry, 1996, 47: p. 555-606.

5. Best, S.P., R.J.H. Clark, M.A.M. Daniels, C.A. Porter, and R. Withnall, *Identification by Raman Microscopy and Visible Reflectance Spectroscopy of Pigments on an Icelandic Manuscript,* Studies in Conservation, 1995, 40(1): p. 31-40.

6. Cheon, S., K.D. Kihm, J.S. Park, J.S. Lee, B.J. Lee, H. Kim, and B.H. Hong, *How to optically count graphene layers,* Opt. Lett., 2012, 37(18): p. 3765-3767.

7. Fabbri, M., M. Picollo, S. Porcinai, and M. Bacci, *Mid-Infrared Fiber-Optics Reflectance Spectroscopy: A Noninvasive Technique for Remote Analysis of Painted Layers. Part II: Statistical Analysis of Spectra,* Appl. Spectrosc., 2001, 55(4): p. 428-433.

8. Gauderon, R., P.B. Lukins, and C.J. Sheppard, *Three-dimensional second-harmonic generation imaging with femtosecond laser pulses,* Opt Lett, 1998, 23(15): p. 1209-11.

9. Zuzak, K.J., M.D. Schaeberle, E.N. Lewis, and I.W. Levin, *Visible reflectance hyperspectral imaging: characterization of a noninvasive, in vivo system for determining tissue perfusion,* Anal Chem, 2002, 74(9): p. 2021-8.

10. Lakowicz, J.R., *Principles of Fluorescence Spectroscopy*. 2nd ed 1999, New York: Kluwer Academic/Plenum.

11. Lichtman, J.W. and J.A. Conchello, *Fluorescence microscopy,* Nature Methods, 2005, 2(12): p. 910-919.

12. Luker, G.D. and K.E. Luker, *Optical imaging: current applications and future directions,* J Nucl Med, 2008, 49(1): p. 1-4.

13. Bastiaens, P.I.H. and A. Squire, *Fluorescence lifetime imaging microscopy: spatial resolution of biochemical processes in the cell,* Trends in Cell Biology, 1999, 9(2): p. 48-52.

14. OLeary, M.A., D.A. Boas, X.D. Li, B. Chance, and A.G. Yodh, *Fluorescence lifetime imaging in turbid media,* Optics Letters, 1996, 21(2): p. 158-160.

15. Soloviev, V.Y., K.B. Tahir, J. McGinty, D.S. Elson, M. Neil, A. Sardini, J. Hajnal, S.R. Arridge, and P.M.W. French, *Fluorescence lifetime imaging through turbid media reconstructed in the Fourier domain using time-gated imaging data,* Diffuse Optical Imaging of Tissue, 2007, 6629: p. V6291-V6291.

16. Stringari, C., A. Cinquin, O. Cinquin, M.A. Digman, P.J. Donovan, and E. Gratton, *Phasor approach to fluorescence lifetime microscopy distinguishes different metabolic states of germ cells in a live tissue,* Proceedings of the National Academy of Sciences, 2011, 108(33): p. 13582-13587.

17. van Munster, E.B. and T.W.J. Gadella, *Fluorescence Lifetime Imaging Microscopy (FLIM)*, in *Microscopy Techniques*, J. Rietdorf, Editor 2005, Springer Berlin / Heidelberg. p. 1301-1303.

18. Hanlon, E.B., R. Manoharan, T.W. Koo, K.E. Shafer, J.T. Motz, M. Fitzmaurice, J.R. Kramer, I. Itzkan, R.R. Dasari, and M.S. Feld, *Prospects for in vivo Raman spectroscopy,* Physics in Medicine and Biology, 2000, 45(2): p. R1-R59.

19. Zavaleta, C., A. de la Zerda, Z. Liu, S. Keren, Z. Cheng, M. Schipper, X. Chen, H. Dai, and S.S. Gambhir, *Noninvasive Raman spectroscopy in living mice for evaluation of tumor targeting with carbon nanotubes,* Nano Letters, 2008, 8(9): p. 2800-2805.

20. Havener, R.W., S.Y. Ju, L. Brown, Z.H. Wang, M. Wojcik, C.S. Ruiz-Vargas, and J. Park, *High-Throughput Graphene Imaging on Arbitrary Substrates with Widefield Raman Spectroscopy,* Acs Nano, 2012, 6(1): p. 373-380.

21. Robert, H.W., *Confocal optical microscopy,* Reports on Progress in Physics, 1996, 59(3): p. 427.

22. Wilhelm, S., B. Gröbler, M. Gluch, and H. Heinz *Confocal laser scanning microscopy principles*. 2000. http://zeiss-campus.magnet.fsu.edu/referencelibrary/laserconfocal.html.

23. Paddock, S., *Principles and practices of laser scanning confocal microscopy,* Molecular Biotechnology, 2000, 16(2): p. 127-149.

24. Lorenzetti, G., J. Striova, A. Zoppi, and E.M. Castellucci, *Confocal Raman microscopy for in depth analysis in the field of cultural heritage,* Journal of Molecular Structure, 2011, 993(1-3): p. 97-103.

25. Xu, C., W. Zipfel, J.B. Shear, R.M. Williams, and W.W. Webb, *Multiphoton fluorescence excitation: New spectral windows for biological nonlinear microscopy,* Proceedings of the National Academy of Sciences of the United States of America, 1996, 93(20): p. 10763-10768.

26. Denk, W. and K. Svoboda, *Photon upmanship: why multiphoton imaging is more than a gimmick,* Neuron, 1997, 18(3): p. 351-7.

27. Fu, D., *Developing novel nonlinear optical contrast for biomedical imaging*, 2009, Princeton University: United States -- New Jersey.

28. Kobat, D., M.E. Durst, N. Nishimura, A.W. Wong, C.B. Schaffer, and C. Xu, *Deep tissue multiphoton microscopy using longer wavelength excitation,* Opt. Express, 2009, 17(16): p. 13354-13364.

29. Horton, N.G., K. Wang, D. Kobat, F.W. Wise, and C. Xu. *In Vivo Three-Photon Microscopy of Subcortical Structures within an Intact Mouse Brain*. 2012. Optical Society of America 2012: p. CThC5.4.

30. Denk, W., J.H. Strickler, and W.W. Webb, *Two-photon laser scanning fluorescence microscopy,* Science, 1990, 248(4951): p. 73-6.

31. Larson, D.R., W.R. Zipfel, R.M. Williams, S.W. Clark, M.P. Bruchez, F.W. Wise, and W.W. Webb, *Water-soluble quantum dots for multiphoton fluorescence imaging in vivo,* Science, 2003, 300(5624): p. 1434-1436.

32. Rubart, M., *Two-Photon Microscopy of Cells and Tissue,* Circulation Research, 2004, 95(12): p. 1154-1166.

33. So, P.T.C., C.Y. Dong, B.R. Masters, and K.M. Berland, *Two-photon excitation fluorescence microscopy,* Annual Review of Biomedical Engineering, 2000, 2: p. 399-429.

34. Jung, J.C. and M.J. Schnitzer, *Multiphoton endoscopy,* Opt. Lett., 2003, 28(11): p. 902-904.

35. Brown, R.M., A.C. Millard, and P.J. Campagnola, *Macromolecular structure of cellulose studied by second-harmonic generation imaging microscopy,* Optics Letters, 2003, 28(22): p. 2207-2209.

36. Campagnola, P.J. and L.M. Loew, *Second-harmonic imaging microscopy for visualizing biomolecular arrays in cells, tissues and organisms,* Nat Biotechnol, 2003, 21(11): p. 1356-60.

37. Tsai, M.-R., S.-Y. Chen, D.-B. Shieh, P.-J. Lou, and C.-K. Sun, *In vivo optical virtual biopsy of human oral mucosa with harmonic generation microscopy,* Biomed. Opt. Express, 2011, 2(8): p. 2317-2328.

38. Barad, Y., H. Eisenberg, M. Horowitz, and Y. Silberberg, *Nonlinear scanning laser microscopy by third harmonic generation,* Applied Physics Letters, 1997, 70(8): p. 922-924.

39. Filippidis, G., K. Melessanaki, and C. Fotakis, *Second and third harmonic generation measurements of glues used for lining textile supports of painted artworks,* Analytical and Bioanalytical Chemistry, 2009, 395(7): p. 2161-2166.

40. Cheng, J.X. and X.S. Xie, *Coherent anti-Stokes Raman scattering microscopy: Instrumentation, theory, and applications,* Journal of Physical Chemistry B, 2004, 108(3): p. 827-840.

41. Li, B., W.S. Warren, and M.C. Fischer, *Phase-cycling coherent anti-Stokes Raman scattering using shaped femtosecond laser pulses,* Optics Express, 2010, 18(25): p. 25825-25832.

42. Warren, W.S., W. Wagner, and T. Ye, *The prospects for high resolution optical brain imaging: the magnetic resonance perspective,* Magnetic Resonance Imaging, 2003, 21(10): p. 1225-1233.

43. Fischer, M.C., I. Piletic, D. Fu, T.E. Matthews, H. Liu, P. Samineni, B. Li, and W.S. Warren, *Enhancing two-color absorption, self-phase modulation, and Raman*

microscopy signatures in tissue with femtosecond laser pulse shaping, Proc. SPIE, 2009, 7183: p. 71830V-11.

44. Fischer, M.C., T. Ye, G. Yurtsever, A. Miller, M. Ciocca, W. Wagner, and W.S. Warren, *Two-photon absorption and self-phase modulation measurements with shaped femtosecond laser pulses,* Optics Letters, 2005, 30(12): p. 1551-1553.

45. Fu, D., T. Ye, T.E. Matthews, G. Yurtsever, and W.S. Warren, *Two-color, two-photon, and excited-state absorption microscopy,* Journal of Biomedical Optics, 2007, 12(5).

46. Li, B., K.E. Claytor, H. Yuan, T. Vo-Dinh, W.S. Warren, and M.C. Fischer, *Multicontrast nonlinear optical microscopy with a compact and rapid pulse shaper,* Opt. Lett., 2012, 37(13): p. 2763-2765.

47. Samineni, P., B.L. Li, J.W. Wilson, W.S. Warren, and M.C. Fischer, *Cross-phase modulation imaging,* Optics Letters, 2012, 37(5): p. 800-802.

48. Tian, P.F. and W.S. Warren, *Ultrafast measurement of two-photon absorption by loss modulation,* Optics Letters, 2002, 27(18): p. 1634-1636.

49. Warren, W.S., M.C. Fischer, and T. Ye, *Cellular imaging - Novel nonlinear contrast improves deep-tissue microscopy,* Laser Focus World, 2007, 43(6): p. 99-103.

50. Wilson, J.W., P. Samineni, W.S. Warren, and M.C. Fischer, *Cross-phase modulation spectral shifting: nonlinear phase contrast in a pump-probe microscope,* Biomedical Optics Express, 2012, 3(5): p. 854-862.

51. Ye, T., D. Fu, and W.S. Warren, *Nonlinear Absorption Microscopy,* Photochemistry and Photobiology, 2009, 85(3): p. 631-645.

52. Fu, D., T. Ye, T.E. Matthews, B.J. Chen, G. Yurtserver, and W.S. Warren, *High-resolution in vivo imaging of blood vessels without labeling,* Optics Letters, 2007, 32(18): p. 2641-2643.

53. Fu, D., T. Ye, T.E. Matthews, J. Grichnik, L. Hong, J.D. Simon, and W.S. Warren, *Probing skin pigmentation changes with transient absorption imaging of eumelanin and pheomelanin,* Journal of Biomedical Optics, 2008, 13(5): p. 054036.

54. Matthews, T.E., I.R. Piletic, M.A. Selim, M.J. Simpson, and W.S. Warren, *Pump-probe imaging differentiates melanoma from melanocytic nevi,* Sci Transl Med, 2011, 3(71): p. 71ra15.

55. Samineni, P., A. deCruz, T.E. Villafana, W.S. Warren, and M.C. Fischer, *Pump-probe imaging of historical pigments used in paintings,* Optics Letters, 2012, 37(8): p. 1310-1312.

56. Freudiger, C.W., W. Min, B.G. Saar, S. Lu, G.R. Holtom, C.W. He, J.C. Tsai, J.X. Kang, and X.S. Xie, *Label-Free Biomedical Imaging with High Sensitivity by Stimulated Raman Scattering Microscopy,* Science, 2008, 322(5909): p. 1857-1861.

57. Min, W., C.W. Freudiger, S.J. Lu, and X.S. Xie, *Coherent Nonlinear Optical Imaging: Beyond Fluorescence Microscopy,* Annual Review of Physical Chemistry, Vol 62, 2011, 62: p. 507-530.

58. Min, W., S.J. Lu, S.S. Chong, R. Roy, G.R. Holtom, and X.S. Xie, *Imaging chromophores with undetectable fluorescence by stimulated emission microscopy,* Nature, 2009, 461(7267): p. 1105-1109.

59. Fischer, M.C., H.C. Liu, I.R. Piletic, and W.S. Warren, *Simultaneous self-phase modulation and two-photon absorption measurement by a spectral homodyne Z-scan method,* Optics Express, 2008, 16(6): p. 4192-4205.

60. Piletic, I.R., M.C. Fischer, P. Samineni, G. Yurtsever, and W.S. Warren, *Rapid pulse shaping with homodyne detection for measuring nonlinear optical signals,* Optics Letters, 2008, 33(13): p. 1482-1484.

61. Iijima, S. and T. Ichihashi, *Single-Shell Carbon Nanotubes of 1-Nm Diameter,* Nature, 1993, 363(6430): p. 603-605.

62. Ajayan, P.M. and O.Z. Zhou, *Applications of carbon nanotubes,* Carbon Nanotubes, 2001, 80: p. 391-425.

63. Xia, Y.N., *Nanomaterials at work in biomedical research,* Nature Materials, 2008, 7(10): p. 758-760.

64. Feng, L.Z. and Z.A. Liu, *Graphene in biomedicine: opportunities and challenges,* Nanomedicine, 2011, 6(2): p. 317-324.

65. Medintz, I.L., A.R. Clapp, H. Mattoussi, E.R. Goldman, B. Fisher, and J.M. Mauro, *Self-assembled nanoscale biosensors based on quantum dot FRET donors,* Nature Materials, 2003, 2(9): p. 630-638.

66. Zavaleta, C.L., B.R. Smith, I. Walton, W. Doering, G. Davis, B. Shojaei, M.J. Natan, and S.S. Gambhir, *Multiplexed imaging of surface enhanced Raman scattering nanotags in living mice using noninvasive Raman spectroscopy,* Proceedings of the National Academy of Sciences of the United States of America, 2009, 106(32): p. 13511-13516.

67. Wang, Y., C.-Y. Lin, A. Nikolaenko, V. Raghunathan, and E.O. Potma, *Four-wave mixing microscopy of nanostructures,* Adv. Opt. Photon., 2011, 3(1): p. 1-52.

68. Yue, S.H., M.N. Slipchenko, and J.X. Cheng, *Multimodal nonlinear optical microscopy,* Laser & Photonics Reviews, 2011, 5(4): p. 496-512.

69. Fischer, M.C., T. Ye, G. Yurtsever, A. Miller, M. Ciocca, W. Wagner, and W.S. Warren, *Two-photon absorption and self-phase modulation measurements with shaped femtosecond laser pulses,* Opt. Lett., 2005, 30(12): p. 1551-3.

70. Boyd, R.W., *Nonlinear Optics* second ed 2003, New york: Academic Press.

71. Agrawal, G.P., *Nonlinear fiber optics*. 4th ed 2007, Boston: Elsevier / Academic Press. xvi, 529 p.

72. Hendow, S.T. and S.A. Shakir, *Recursive Numerical-Solution for Nonlinear-Wave Propagation in Fibers and Cylindrically Symmetrical-Systems,* Applied Optics, 1986, 25(11): p. 1759-1764.

73. Warren, W.S. and M.S. Silver, *The art of pulse crafting: applications to magnetic resonance and laser spectroscopy,* Advances in magnetic resonance, 1988, 12: p. 247-384.

74. Weiner, A.M., *Femtosecond pulse shaping using spatial light modulators,* Review of Scientific Instruments, 2000, 71(5): p. 1929-1960.

75. Weiner, A.M., J.P. Heritage, R.J. Hawkins, R.N. Thurston, E.M. Kirschner, D.E. Leaird, and W.J. Tomlinson, *Experimental-Observation of the Fundamental Dark Soliton in Optical Fibers,* Physical Review Letters, 1988, 61(21): p. 2445-2448.

76. Weiner, A.M., Y. Silberberg, H. Fouckhardt, D.E. Leaird, M.A. Saifi, M.J. Andrejco, and P.W. Smith, *Use of Femtosecond Square Pulses to Avoid Pulse Breakup in All-Optical Switching,* Ieee Journal of Quantum Electronics, 1989, 25(12): p. 2648-2655.

77. Umstadter, D., E. Esarey, and J. Kim, *Nonlinear Plasma-Waves Resonantly Driven by Optimized Laser-Pulse Trains,* Physical Review Letters, 1994, 72(8): p. 1224-1227.

78. Umstadter, D., J. Kim, E. Esarey, E. Dodd, and T. Neubert, *Electron acceleration by nonlinear plasma waves resonantly driven with optimized high-intensity laser pulse trains,* Future of Accelerator Physics, 1996(356): p. 270-300.

79. Hartemann, F.V., *High-intensity scattering processes of relativistic electrons in vacuum,* Physics of Plasmas, 1998, 5(5): p. 2037-2047.

80. Warren, W.S., *Effects of Pulse Shaping in Laser Spectroscopy and Nuclear Magnetic-Resonance,* Science, 1988, 242(4880): p. 878-884.

81. Oron, D., N. Dudovich, and Y. Silberberg, *Single-pulse phase-contrast nonlinear Raman spectroscopy,* Physical Review Letters, 2002, 89(27).

82. Silberberg, Y., *Quantum Coherent Control for Nonlinear Spectroscopy and Microscopy,* Annual Review of Physical Chemistry, 2009, 60: p. 277-292.

83. Hillegas, C.W., J.X. Tull, D. Goswami, D. Strickland, and W.S. Warren, *Femtosecond Laser-Pulse Shaping by Use of Microsecond Radiofrequency Pulses,* Optics Letters, 1994, 19(10): p. 737-739.

84. Cundiff, S.T. and A.M. Weiner, *Optical arbitrary waveform generation,* Nature Photonics, 2010, 4(11): p. 760-766.

85. Yuan, H.K., C.G. Khoury, H. Hwang, C.M. Wilson, G.A. Grant, and T. Vo-Dinh, *Gold nanostars: surfactant-free synthesis, 3D modelling, and two-photon photoluminescence imaging,* Nanotechnology, 2012, 23(7).

86. Wang, H.F., T.B. Huff, D.A. Zweifel, W. He, P.S. Low, A. Wei, and J.X. Cheng, *In vitro and in vivo two-photon luminescence imaging of single gold nanorods,* Proceedings of the National Academy of Sciences of the United States of America, 2005, 102(44): p. 15752-15756.

87. Ando, J., K. Fujita, N.I. Smith, and S. Kawata, *Dynamic SERS Imaging of Cellular Transport Pathways with Endocytosed Gold Nanoparticles,* Nano Letters, 2011, 11(12): p. 5344-5348.

88. Jares-Erijman, E.A. and T.M. Jovin, *FRET imaging,* Nature Biotechnology, 2003, 21(11): p. 1387-1395.

89. Li, B., Y. Cheng, J. Liu, C. Yi, A.S. Brown, H. Yuan, T. Vo-Dinh, M.C. Fischer, and W.S. Warren, *Direct Optical Imaging of Graphene In Vitro by Nonlinear Femtosecond Laser Spectral Reshaping,* Nano Letters, 2012.

90. Yang, K., S.A. Zhang, G.X. Zhang, X.M. Sun, S.T. Lee, and Z.A. Liu, *Graphene in Mice: Ultrahigh In Vivo Tumor Uptake and Efficient Photothermal Therapy,* Nano Letters, 2010, 10(9): p. 3318-3323.

91. Liu, Z., J.T. Robinson, X.M. Sun, and H.J. Dai, *PEGylated nanographene oxide for delivery of water-insoluble cancer drugs,* Journal of the American Chemical Society, 2008, 130(33): p. 10876-10877.

92. Sun, X.M., Z. Liu, K. Welsher, J.T. Robinson, A. Goodwin, S. Zaric, and H.J. Dai, *Nano-Graphene Oxide for Cellular Imaging and Drug Delivery,* Nano Research, 2008, 1(3): p. 203-212.

93. Lu, C.H., H.H. Yang, C.L. Zhu, X. Chen, and G.N. Chen, *A Graphene Platform for Sensing Biomolecules,* Angewandte Chemie-International Edition, 2009, 48(26): p. 4785-4787.

94. Loh, K.P., Q.L. Bao, G. Eda, and M. Chhowalla, *Graphene oxide as a chemically tunable platform for optical applications,* Nature Chemistry, 2010, 2(12): p. 1015-1024.

95. Park, S., N. Mohanty, J.W. Suk, A. Nagaraja, J.H. An, R.D. Piner, W.W. Cai, D.R. Dreyer, V. Berry, and R.S. Ruoff, *Biocompatible, Robust Free-Standing Paper Composed of a TWEEN/Graphene Composite,* Advanced Materials, 2010, 22(15): p. 1736-1740.

96. Schinwald, A., F.A. Murphy, A. Jones, W. MacNee, and K. Donaldson, *Graphene-Based Nanoplatelets: A New Risk to the Respiratory System as a Consequence of Their Unusual Aerodynamic Properties,* Acs Nano, 2012, 6(1): p. 736-746.

97. Duch, M.C., G.R.S. Budinger, Y.T. Liang, S. Soberanes, D. Urich, S.E. Chiarella, L.A. Campochiaro, A. Gonzalez, N.S. Chandel, M.C. Hersam, and G.M. Mutlu, *Minimizing Oxidation and Stable Nanoscale Dispersion Improves the Biocompatibility of Graphene in the Lung,* Nano Letters, 2011, 11(12): p. 5201-5207.

98. Ishigami, M., J.H. Chen, W.G. Cullen, M.S. Fuhrer, and E.D. Williams, *Atomic structure of graphene on SiO2,* Nano Letters, 2007, 7(6): p. 1643-1648.

99. Nair, R.R., P. Blake, A.N. Grigorenko, K.S. Novoselov, T.J. Booth, T. Stauber, N.M.R. Peres, and A.K. Geim, *Fine structure constant defines visual transparency of graphene,* Science, 2008, 320(5881): p. 1308-1308.

100. Roddaro, S., P. Pingue, V. Piazza, V. Pellegrini, and F. Beltram, *The optical visibility of graphene: Interference colors of ultrathin graphite on SiO2,* Nano Letters, 2007, 7(9): p. 2707-2710.

101. Casiraghi, C., A. Hartschuh, E. Lidorikis, H. Qian, H. Harutyunyan, T. Gokus, K.S. Novoselov, and A.C. Ferrari, *Rayleigh imaging of graphene and graphene layers,* Nano Letters, 2007, 7(9): p. 2711-2717.

102. Senyuk, B., N. Behabtu, B.G. Pacheco, T. Lee, G. Ceriotti, J.M. Tour, M. Pasquali, and I.I. Smalyukh, *Nonlinear Photoluminescence Imaging of Isotropic and Liquid Crystalline Dispersions of Graphene Oxide,* Acs Nano, 2012, 6(9): p. 8060-8066.

103. Galande, C., A.D. Mohite, A.V. Naumov, W. Gao, L. Ci, A. Ajayan, H. Gao, A. Srivastava, R.B. Weisman, and P.M. Ajayan, *Quasi-Molecular Fluorescence from Graphene Oxide,* Sci. Rep., 2011, 1(85): p. 5.

104. Lui, C.H., K.F. Mak, J. Shan, and T.F. Heinz, *Ultrafast Photoluminescence from Graphene,* Physical Review Letters, 2010, 105(12): p. 127404.

105. Kim, J., L.J. Cote, F. Kim, and J.X. Huang, *Visualizing Graphene Based Sheets by Fluorescence Quenching Microscopy,* Journal of the American Chemical Society, 2010, 132(1): p. 260-267.

106. Bonaccorso, F., Z. Sun, T. Hasan, and A.C. Ferrari, *Graphene photonics and optoelectronics,* Nature Photonics, 2010, 4(9): p. 611-622.

107. Hendry, E., P.J. Hale, J. Moger, A.K. Savchenko, and S.A. Mikhailov, *Coherent Nonlinear Optical Response of Graphene,* Physical Review Letters, 2010, 105(9): p. 097401.

108. Spanu, L., S. Sorella, and G. Galli, *Nature and Strength of Interlayer Binding in Graphite,* Physical Review Letters, 2009, 103(19).

109. Kim, H., T. Sheps, P.G. Collins, and E.O. Potma, *Nonlinear Optical Imaging of Individual Carbon Nanotubes with Four-Wave-Mixing Microscopy,* Nano Letters, 2009, 9(8): p. 2991-2995.

110. Druet, S.A.J., B. Attal, T.K. Gustafson, and J.P. Taran, *Electronic Resonance Enhancement of Coherent Anti-Stokes Raman-Scattering,* Physical Review A, 1978, 18(4): p. 1529-1557.

111. Min, W., S.J. Lu, M. Rueckel, G.R. Holtom, and X.S. Xie, *Near-Degenerate Four-Wave-Mixing Microscopy,* Nano Letters, 2009, 9(6): p. 2423-2426.

112. Stohr, R.J., R. Kolesov, J. Pflaum, and J. Wrachtrup, *Fluorescence of laser-created electron-hole plasma in graphene,* Physical Review B, 2010, 82(12): p. 121408(R).

113. Kim, K.S., Y. Zhao, H. Jang, S.Y. Lee, J.M. Kim, K.S. Kim, J.H. Ahn, P. Kim, J.Y. Choi, and B.H. Hong, *Large-scale pattern growth of graphene films for stretchable transparent electrodes,* Nature, 2009, 457(7230): p. 706-710.

114. Reina, A., X.T. Jia, J. Ho, D. Nezich, H.B. Son, V. Bulovic, M.S. Dresselhaus, and J. Kong, *Large Area, Few-Layer Graphene Films on Arbitrary Substrates by Chemical Vapor Deposition,* Nano Letters, 2009, 9(1): p. 30-35.

115. Dan, Y.P., Y. Lu, N.J. Kybert, Z.T. Luo, and A.T.C. Johnson, *Intrinsic Response of Graphene Vapor Sensors,* Nano Letters, 2009, 9(4): p. 1472-1475.

116. Lee, Y., S. Bae, H. Jang, S. Jang, S.E. Zhu, S.H. Sim, Y.I. Song, B.H. Hong, and J.H. Ahn, *Wafer-Scale Synthesis and Transfer of Graphene Films,* Nano Letters, 2010, 10(2): p. 490-493.

117. Chase, L.L., Van Stryland, E. W., *CRC Handbook of Laser Science and Techonology* 1995: CRC Press, Boca Raton, FL. Section 8.1.

118. Guillet de Chatellus, H. and E. Freysz, *Measurement of the third-order susceptibility of glasses by EFISH of femtosecond pulses,* Opt. Express, 2001, 9(11): p. 586-591.

119. Zhang, Z.S. and P.L. Voss, *Full-band quantum-dynamical theory of saturation and four-wave mixing in graphene,* Optics Letters, 2011, 36(23): p. 4569-4571.

120. Li, T., L. Luo, M. Hupalo, J. Zhang, M.C. Tringides, J. Schmalian, and J. Wang, *Femtosecond Population Inversion and Stimulated Emission of Dense Dirac Fermions in Graphene,* Physical Review Letters, 2012, 108(16).

121. Trebino, R., *Frequency-Resolved Optical Gating: The Measurement of Ultrashort Laser Pulses* 2000, Norwell, MA USA: Kluwer Academic Publishers.

122. Dean, J.J. and H.M. van Driel, *Graphene and few-layer graphite probed by second-harmonic generation: Theory and experiment,* Physical Review B, 2010, 82(12).

123. Mikhailov, S.A., *Theory of the giant plasmon-enhanced second-harmonic generation in graphene and semiconductor two-dimensional electron systems,* Physical Review B, 2011, 84(4).

124. Bain, C.D., *Studies of adsorption at interfaces by optical techniques: ellipsometry, second harmonic generation and sum-frequency generation,* Current Opinion in Colloid & Interface Science, 1998, 3(3): p. 287-292.

125. Shen, Y.R., *Optical Second Harmonic Generation at Interfaces,* Annual Review of Physical Chemistry, 1989, 40(1): p. 327-350.

126. Bao, Q.L., H. Zhang, Y. Wang, Z.H. Ni, Y.L. Yan, Z.X. Shen, K.P. Loh, and D.Y. Tang, *Atomic-Layer Graphene as a Saturable Absorber for Ultrafast Pulsed Lasers,* Advanced Functional Materials, 2009, 19(19): p. 3077-3083.

127. Sun, Z.P., T. Hasan, F. Torrisi, D. Popa, G. Privitera, F.Q. Wang, F. Bonaccorso, D.M. Basko, and A.C. Ferrari, *Graphene Mode-Locked Ultrafast Laser,* Acs Nano, 2010, 4(2): p. 803-810.

128. Gu, T., N. Petrone, J.F. McMillan, A. van der Zande, M. Yu, G.Q. Lo, D.L. Kwong, J. Hone, and C.W. Wong, *Regenerative oscillation and four-wave mixing in graphene optoelectronics,* Nature Photonics, 2012, 6(8): p. 554-559.

129. Ferrari, A.C., J.C. Meyer, V. Scardaci, C. Casiraghi, M. Lazzeri, F. Mauri, S. Piscanec, D. Jiang, K.S. Novoselov, S. Roth, and A.K. Geim, *Raman spectrum of graphene and graphene layers,* Physical Review Letters, 2006, 97(18).

130. Yoon, D., H. Moon, H. Cheong, J.S. Choi, J.A. Choi, and B.H. Park, *Variations in the Raman Spectrum as a Function of the Number of Graphene Layers,* Journal of the Korean Physical Society, 2009, 55(3): p. 1299-1303.

131. Mikhailov, S.A., *Theory of the nonlinear optical frequency mixing effect in graphene,* Physica E: Low-dimensional Systems and Nanostructures, 2012, 44(6): p. 924-927.

132. Xing, G., H. Guo, X. Zhang, T.C. Sum, and C.H.A. Huan, *The Physics of ultrafast saturable absorption in graphene,* Opt. Express, 2010, 18(5): p. 4564-4573.

133. Hummers, W.S. and R.E. Offeman, *Preparation of Graphitic Oxide,* Journal of the American Chemical Society, 1958, 80(6): p. 1339-1339.

134. Zhao, J.P., S.F. Pei, W.C. Ren, L.B. Gao, and H.M. Cheng, *Efficient Preparation of Large-Area Graphene Oxide Sheets for Transparent Conductive Films,* Acs Nano, 2010, 4(9): p. 5245-5252.

135. Li, D., M.B. Muller, S. Gilje, R.B. Kaner, and G.G. Wallace, *Processable aqueous dispersions of graphene nanosheets,* Nature Nanotechnology, 2008, 3(2): p. 101-105.

136. El-Kady, M.F., V. Strong, S. Dubin, and R.B. Kaner, *Laser Scribing of High-Performance and Flexible Graphene-Based Electrochemical Capacitors,* Science, 2012, 335(6074): p. 1326-1330.

137. Novoselov, K.S., A.K. Geim, S.V. Morozov, D. Jiang, Y. Zhang, S.V. Dubonos, I.V. Grigorieva, and A.A. Firsov, *Electric field effect in atomically thin carbon films,* Science, 2004, 306(5696): p. 666-669.

138. Cui, M., B.R. Bachler, and J.P. Ogilvie, *Comparing coherent and spontaneous Raman scattering under biological imaging conditions,* Optics Letters, 2009, 34(6): p. 773-775.

139. Cheng, J.X., L.D. Book, and X.S. Xie, *Polarization coherent anti-Stokes Raman scattering microscopy,* Optics Letters, 2001, 26(17): p. 1341-1343.

140. Lu, F., W. Zheng, and Z.W. Huang, *Heterodyne polarization coherent anti-Stokes Raman scattering microscopy,* Applied Physics Letters, 2008, 92(12).

141. Lu, F., W. Zheng, C.L. Sheppard, and Z.W. Huang, *Interferometric polarization coherent anti-Stokes Raman scattering (IP-CARS) microscopy,* Optics Letters, 2008, 33(6): p. 602-604.

142. Evans, C.L., E.O. Potma, and X.S.N. Xie, *Coherent anti-Stokes Raman scattering spectral interferometry: determination of the real and imaginary components of nonlinear susceptibility chi((3)) for vibrational microscopy,* Optics Letters, 2004, 29(24): p. 2923-2925.

143. Jurna, M., J.P. Korterik, C. Otto, J.L. Herek, and H.L. Offerhaus, *Vibrational Phase Contrast Microscopy by Use of Coherent Anti-Stokes Raman Scattering,* Physical Review Letters, 2009, 103(4).

144. Xu, X.J.G., S.O. Konorov, J.W. Hepburn, and V. Milner, *Background-free coherent Raman spectroscopy by detecting the spectral phase of molecular vibrations,* Optics Letters, 2008, 33(11): p. 1177-1179.

145. von Vacano, B., T. Buckup, and M. Motzkus, *Highly sensitive single-beam heterodyne coherent anti-Stokes Raman scattering,* Optics Letters, 2006, 31(16): p. 2495-2497.

146. Marks, D.L. and S.A. Boppart, *Nonlinear interferometric vibrational imaging,* Physical Review Letters, 2004, 92(12).

147. Lim, S.H., A.G. Caster, and S.R. Leone, *Fourier transform spectral interferometric coherent anti-Stokes Raman scattering (FTSI-CARS) spectroscopy,* Optics Letters, 2007, 32(10): p. 1332-1334.

148. Lee, Y.J. and M.T. Cicerone, *Single-shot interferometric approach to background free broadband coherent anti-Stokes Raman scattering spectroscopy,* Optics Express, 2009, 17(1): p. 123-135.

149. Postma, S., A.C.W. van Rhijn, J.P. Korterik, P. Gross, J.L. Herek, and H.L. Offerhaus, *Application of spectral phase shaping to high resolution CARS spectroscopy,* Optics Express, 2008, 16(11): p. 7985-7996.

150. Oron, D., N. Dudovich, D. Yelin, and Y. Silberberg, *Narrow-band coherent anti-stokes Raman signals from broad-band pulses,* Physical Review Letters, 2002, 88(6).

151. Chen, B.C. and S.H. Lim, *Optimal laser pulse shaping for interferometric multiplex coherent anti-stokes Raman scattering microscopy,* Journal of Physical Chemistry B, 2008, 112(12): p. 3653-3661.

Biography

Baolei Li was born in Suqian, Jiangsu province, China on 28th October, 1985. He received a bachelor of science in physics in June 2005 from Nanjing University located in Nanjing, Jiangsu province, China. In September 2005, He entered Tsinghua University in Beijing China for graduate study and received a master of science in physics two years later. He continued his graduate study in physics at Duke University from August 2007. During graduate work at Duke University in Durham, NC he published the following papers: B. Li, W. S. Warren, M. C. Fischer, 'Phase cycling coherent anti-Stokes Raman scattering with shaped femtosecond laser pulses', *Optics Express, 18, 25825-25832, 2010*. P. Samineni, B. Li, J. W. Wilson, W. S. Warren, M. C. Fischer, 'Cross-phase modulation imaging', *Optics Letters 37, 800-802, 2012* (this work was featured in OSA Spotlight on Optics in April 2012 and was selected for additional publication in *Virtual Journal for Biomedical Optics 7(5)*), B. Li, K. E. Claytor, H. Yuan, T. Vo-Dinh, W. S. Warren, M. C. Fischer, 'Multicontrast nonlinear optical microscopy with a compact and rapid pulse shaper', *Optics Letters 37, 2763-2765, 2012* (selected for additional publication in *Virtual Journal for Biomedical Optics*). B. Li, Y. Cheng, J. Liu, C. Yi, A. S. Brown, H. Yuan, T. Vo-Dinh, M. C. Fischer and W. S. Warren, Direct optical imaging of graphene in vitro by nonlinear femtosecond laser spectral reshaping, *Nano Letters, 12, 5936-5940*, *2012*.